DESIGN AND ANALYSIS OF RAPID APPROXIMATION TECHNIQUES FOR ENERGY-EFFICIENT BUILDING APPLICATION.

Thesis Submitted for the Award of the Degree of

DOCTOR OF PHILOSOPHY

in

Electronics and Communication Engineering

By

Sanam Kouser

Registration Number: 11919162

Supervised By

Dr. G. Raam Dheep (25227)

Assistant Professor

School of Electronics and Electrical Engineering

Lovely Professional University, Punjab

Co-Supervised By

Prof. Ramesh Bansal

Professor

Department of Electrical, University of Sharjah, UAE

LOVELY PROFESSIONAL UNIVERSITY, PUNJAB

2023

DECLARATION

I, hereby declare that the presented work in the thesis entitled "Design and Analysis of Rapid Approximation Techniques for Energy-efficient Building Application" in fulfilment of the degree of **Doctor of Philosophy (Ph. D.)** is the outcome of research work carried out by me under the supervision of Dr. G. Raam Dheep working as Assistant professor in the Electrical and Electronic of Lovely Professional University, Punjab, India. In keeping with the general practice of reporting scientific observations, due acknowledgements have been made whenever the work described here has been based on the findings of another investigator. This work has not been submitted in part or full to any other University or Institute for the award of any degree.

(Signature of Scholar)

Name of the scholar: Sanam Kouser

Registration No.: 11919162

Department/School: Electrical and Electronic Engineering

Lovely Professional University,

Punjab, India

CERTIFICATE

This is to certify that the work reported in the Ph. D. thesis entitled Design and Analysis of Rapid Approximation Techniques for Energy-efficient Building Application" submitted in fulfilment of the requirement for the reward of degree of **Doctor of Philosophy (PhD)** in the Electronic and Communication is a research work carried out by Sanam Kouser Registration No.11919162 is a bonafide record of her original work carried out under my supervision and that no part of thesis has been submitted for any other degree, diploma or equivalent course.

(Signature of Supervisor)

Name of supervisor: Dr.G. Raamdheep

Designation: Assistant Professor

Department/School: School of Electronics and Electrical Engineering
University: Lovely Professional University

(Signature of Co-Supervisor)
Name of Co-Supervisor: Prof. Ramesh Bansal
Designation: Professor
Department/school: Electrical Engineering Department
University: University of Sharjah, UAE

ABSTRACT

As the world's population and economy continue to expand at an unprecedented rate, so does the world's need for electricity. Since CO2 emissions have risen significantly, global warming has occurred. Fortunately, pollution-free, eco-friendly, and limitless forms of renewable energy such as photovoltaic (PV) electricity may help alleviate some of these issues. The installation of PV systems across the world has thus increased in recent decades.

The PV energy conversion system must be run at full power in order to maximize the efficiency of the solar system. With a variety of factors, including sun irradiation, temperature, and array voltage, it is very difficult to accurately measure an array's maximum power point (MPP). So, an MPPT controller is required in the PV system if it is to run at its maximum power point (MPP). Achieved through conventional methods like perturb and observation (P & O) and incremental conductance (INC), as well as through intelligent-based methods like artificial neural networks (ANN), and fuzzy logic controllers. To ensure that the DC connection voltage does not fluctuate, the MPPT has a built-in DC-DC boost converter. this study compares the performance of the fixed voltage MPPT, P&O, INC, FLC and ANN algorithms. The simulation study is carried out for a 100 kW PV standalone system under varying climatic circumstances

Grid-connected PV systems with horse herd optimization MPPT and hybrid Fuzzy Neural Network variable step size P&O MPPT are simulated. The grid-connected PV system was tested with uniform irradiance and partial shading conditions. Design and modelling grid-connected PV system with AEO optimized PI controller is carried out and the artificial ecosystem optimized PI voltage and current controlled grid-connected PV energy conversion system for different operating conditions are analyzed

Grid-connected PV systems are typically more efficient than standalone systems because they can take advantage of net metering, which allows excess electricity generated by the system to be sent back to the grid for credit, reducing the overall cost of electricity.

The design and modelling of grid-connected PV systems with an optimized PI controller are analyzed. Detailed simulation of the artificial ecosystem optimized PI voltage and currently controlled grid-connected PV energy conversion system is examined for different operating conditions and compared with the ZN PI controller and AFL controller. The above methods are compared in terms of THD, rise time and settling time.

Optimization algorithms play a crucial role in tracking the maximum power point (MPP) of a solar panel. The MPP is the point at which the panel generates the maximum amount of power, and tracking it is important for achieving optimal energy output.

Solar panels are subject to various factors that can affect their performance, including temperature, shading, and changes in weather conditions. An optimization algorithm is designed to constantly adjust the system to maximize power output and ensure that the panel operates at its MPP despite these factors. The optimization algorithm uses feedback control to continuously adjust the power output of the solar panel to match the MPP. This is achieved by constantly monitoring the voltage and current output of the panel and adjusting the load resistance accordingly.

Without optimization algorithms, solar panels would not be able to generate as much power as they are capable of. This can result in lower energy output and reduced efficiency, which can be particularly problematic in situations where solar power is the primary source of energy. Optimization algorithms also enable solar panels to be integrated more effectively into the grid. By ensuring that the panel operates at its MPP, the energy generated can be fed back into the grid more efficiently, reducing the need for backup power and increasing the overall efficiency of the system.

Hence in this paper, various optimization techniques are used to extract maximum power from the solar panel. All the algorithms are checked with varying temperatures and changing weather conditions. All the algorithms are compared in terms of various parameters.

A DC microgrid is a type of electrical power produced by solar panels and some battery storage systems. DC microgrids are less common and less

established than AC microgrids, but they are becoming increasingly popular as the use of renewable energy sources such as solar panels and wind turbines becomes more widespread.

DC microgrids are generally more efficient than AC microgrids because they eliminate the need for multiple conversions between AC and DC power. They are also simpler to design and operate, which can make them more cost-effective.

One potential drawback of DC microgrids is that they require specialized equipment, such as DC-DC converters, to convert the voltage of the power to the appropriate level for use by various devices. This can add complexity and cost to the system. Ongoing advancements in solar technology, such as improvements in solar cell efficiency and energy storage systems, can help to make solar PV systems more cost-effective and efficient. This can make them more attractive to homeowners and businesses looking to reduce their carbon footprint and energy costs. The use of optimization techniques ensures that the solar panel is operating at its maximum power point, which maximizes energy output and reduces energy waste. This can lead to significant improvements in energy efficiency and cost savings over time. Optimization techniques can help to mitigate the effects of external factors, such as shading and changes in weather conditions, on the performance of the solar panel. This can help to increase the reliability of the system and reduce the risk of system downtime.

In this paper, the simulation and analysis of various optimization techniques connected with the grid, here many bios-inspired techniques are also used to analyse the effects in solar panels during uniform & non-uniform conditions. By comparing the features of MPPT optimization techniques we can able to choose the best among all, which can able to track maximum power during all conditions. Hence it avoids the drawbacks of the grid-connected system. The prototype model of the best optimization can be developed and it can be used for real-time implementation in Grid-connected as well as standalone PV systems.

ACKNOWLEDGEMENT

Embarking on the journey of researching approximation techniques for energy-efficient building applications, this work is motivated by the dual commitment to advancing building design methodologies and contributing to the utilization of solar energy in sustainable architecture.

This research is driven by the pressing need to address energy efficiency and environmental sustainability challenges in urban structures. Buildings, major contributors to energy consumption and environmental impact, demand innovative solutions. The integration of solar energy solutions, including Maximum Power Point Tracking (MPPT) techniques, is a crucial aspect of this study, recognizing the pivotal role solar power can play in achieving sustainability.

Completing this doctoral research was made possible by the invaluable support of numerous individuals and organizations. Sincere appreciation goes to my primary advisor, Dr. G. Raamdheep for his invaluable guidance, mentorship, and unwavering support throughout the entire research process. His expertise and commitment to excellence have been instrumental in shaping this thesis.

I am equally thankful to my co-supervisor, Prof Ramesh Bansal whose insights, constructive feedback, and collaborative spirit have greatly enriched the quality of this research. His contributions have been integral to the successful completion of this work.

I would also like to express my appreciation to the members of my SAS, ETPs and pre-submission committees, for their thoughtful suggestions and valuable input. Special thanks to my family and friends for their continuous support, understanding, and encouragement during this challenging academic journey.

I acknowledge the financial support provided by my husband that facilitated the execution of this research.

This thesis is a testament to the collective efforts and contributions of many. I am truly grateful for the collaborative spirit fostered by my guide, co-supervisor, colleagues, family and everyone involved in this academic endeavour.

03 May 2024

TABLE OF CONTENTS

CONTENTS

List of Figures		
Fig. No.	**Name of the Figure**	**Page No.**
2.1	Fixed(constant) Voltage peak(max) Solar PV power point technique	10
2.2	Vol-current, vol-power characteristics of a typical 250W PV panel	12
2.3	Zoomed view of voltage vs power characteristics of the typical 250 W PV panel	13
2.4	P&O Peak power locus methodology for Solar PV system	14
2.5	Power-Voltage characteristics of a typical 250 W PV-Panel	15
2.6	Flow Chart for PO MPPT	16
2.7	InC Peak power method for solar PV system	17
2.8	Power-Voltage characteristics of a typical 250 W PV-Panel	18
2.9	Flow Chart for Incremental Conductance MPPT	20
2.10	Fuzzy Logic Based Peak power point technique for Solar PV system	22
2.11	Membership function for Error	23
2.12	Membership function for the rate of change of error	23
2.13	Membership Function for Fuzzy Duty-Cycle	24
2.14	Neural Network Based Peak power point technique for Solar PV system	25
2.15	Generalized Blocks of ANN-based MPPT Controller	26
2.16	Generalized structure of ANN layer	27
2.17	Flowchart for hybrid neural network (NN)/fuzzy logic MPPT with variable step-size	31
2.18	FLC-based variable step size control	32
2.19	The FLC's input membership function (b) The FLC's output membership function	33
2.20	Hybrid fuzzy logic / neural network variable step size MPPT	34
2.21	High step-up ratio DC-DC converter and an active switching LC network	35
2.22	Simulation of Solar PV system with Fixed Voltage MPPT Method	37
2.23	MATLAB Simulation of Solar PV system with P&O MPPT Method	38
2.24	Simulation of Solar PV system with Incremental Conductance MPPT Method	38

List Of Symbols and Abbreviations	
Symbols and Abbreviations	**Description**
AC	Alternating Current
C	Capacitor
V_{dc}	DC voltage
DC	Direct Current
η	Efficiency
EMC	Electromagnetic Compatibility
EMI	Electromagnetic Interference
L	Inductor
P_{IN}	Input power
IEEE	Institute of Electrical and Electronics Engineers
IGBT	Insulated Gate Bipolar Transistor
IC	Integrated Chips
KV	Kilo Volt
$V_{O, MAX}$	Maximum output voltage
MPPT	Maximum PowerPoint Tracking
MW	Mega Watt
MOSFET	Metal Oxide Semiconductor Field Effect Transistor
MLI	Multilevel Inverter
NPC	Neutral Point Clamped
P_{OUT}	Output power
V_{peak}	Peak voltage
PV	Photo Voltaic
P_{LOSS}	Power loss
PWM	Pulse Width Modulation
R_L	Resistor
I_{rms}	RMS current
V_{rms}	RMS voltage
RMS	Root Mean Square
THD	Total Harmonic Distortion
VSI	Voltage Source Inverter

Chapter 1
Introduction

1.1 Introduction

In this chapter, the global energy environment is accurately portrayed. Currently, coal dominates the energy mix; however, there is a shift towards cleaner technologies. Along with detailing the nation's general energy condition, the share of renewable energy in each of India's regions is highlighted. It is projected that by 2050, each region should have 250 MW of renewable capacity. The reasons for and objectives of this research effort are discussed, considering all the novel features of this research at this stage.

Human civilization rests on a foundation of energy. The well-being and progress of people are directly tied to the availability and efficient use of energy, which has a significant impact on a community's or a country's social and economic growth. Because of its central role in global politics, diplomacy, and the economy, energy commands the undivided attention of all parties involved [1]-[5].

The growth of clean energy is relentless, as evidenced by annual statistics from the International Energy Agency (IEA): IEA forecasts project that the renewable energy share in global electricity supply will rise from 28.7% in 2021 to 43% in 2030. Additionally, renewables are expected to contribute two-thirds of the increase in electricity demand during this period, primarily driven by wind and photovoltaic technologies. The International Energy Agency (IEA) projects that global electricity demand will rise by 70% by 2040, with its share of final energy use increasing from 18% to 24% over the same period. This growth is primarily driven by the emerging economies of India, China, Africa, the Middle East, and South-East Asia.

Transitioning to an energy system based on renewable technologies will yield highly positive economic outcomes for the global economy and development. Both the International Renewable Energy Agency (IRENA) and the International Energy Agency (IEA) suggest that tripling the share of renewable energy in electricity generation from the 2022 levels to 90% worldwide by 2030 is essential for meeting the targets set in the Paris Agreement. Achieving this goal will require increasing annual investments in renewable energy from the current USD 1.3 trillion to USD 5 trillion, which will in turn boost job creation and drive growth in the green economy.

Raw strength (man and animal power) was the primary source of pre-industrial energy consumption (about 1700 kWh). Water, wind, the smelting of metals, and firewood were also used as foundations of energy. The discovery and subsequent improvement in coal-use technologies propelled the Industrial Revolution around 1800. A wide range of steam engines powered by coal and automated manufacturing and transportation were widely adopted in line with current developments. Around 1900, the amount of oil and natural gas being discovered and used grew at an exponential rate. Global awareness of inefficient and indiscriminate oil usage was raised during and after World War II due to the struggle for oil possession and access among countries. Alternative sources of energy were sought, and natural gas and uranium-based atomic energy were instrumental in spurring economic expansion. New technologies and resources, particularly renewables, have recently come into emphasis as a way to keep up with the rapid rate of growth while also reducing the dangers associated with fossil fuel consumption. This change has occurred recently. Power supply and energy use patterns have an enormous impact on human civilization's progress. Additionally, the current energy situation may be utilized to help plan the future [6]-[9].

1.2 Review of related works

A thorough analysis of the nation's potential for renewable energy resources, hybrid energy systems, and integrated resource utilization in rural electrification initiatives was deemed necessary to obtain viable data. More research is being done on how to utilize green energy sources, including the creation of stand-alone hybrid systems and efforts to harness renewable energy resource potentials. All simulations for the following authors were performed using the MATLAB simulation environment, even though they took place over a wide range of dates, places, and nations.

As reported in [10], a model of an independent energy generation system was simulated for remote communities. According to the findings of the study, the majority of the energy consumed in remote communities is for lighting, radio, and television entertainment purposes, totalling approximately 0.2 to 1 kWh/day, depending on the time of day. The feasibility of simulating and modeling four distinct system setups/configurations, including a diesel-battery-powered micro hydro generator (solar-diesel-battery), LPG-Solar battery-generator, and hydro-LPG generator-battery, was explored. The most cost-effective micro hydro-hybrid system consisted of a 15-kiloWatt LPG generator, a 14-kiloWatt micro-hydro generator, and a 36-kiloWatt-hour battery storage alternative based on the simulation's results, with a cost per kWh of 6.5 Rupees. The second simulation for the PV hybrid system included a 15-kiloWatt LPG generator, 18kW PV source generator, and 72kWh storage battery; the estimated energy price was computed at 5.8 Rs/kWh, given a remote petrol price of Rs101/liter and Rs60/Kg price of LPG, resulting in a cost of energy at Rs.50/kWh. To reduce costs, a PV hybrid system was shown to be more cost-effective in the northern portions of Cameroon than a micro-hydro system with a minimum flow rate of 200 liters/second. For example, [11]'s research revealed how to create an all-in-one wind turbine along with a solar PV hybrid energy production system that could power a model village of 100 dwellings as well as health clinics and elementary

schools. To get the project started, a study of the potential for the two (wind and PV power) in a region of interest was conducted. Here the best simulation outcome showed that the system was made up of a turbine/diesel wind/PV battery/generator and converter combination. When it comes to this arrangement, the NPC is $109,114, the COE is 0.302-$/kWh, and the total diesel fuel used is 1,955 liters per year, with an operating duration of 633 hours per year for an 84% renewable proportion.

For rural populations in India, [12] conducted a feasibility analysis on a standalone hybrid power system from solar and wind sources that could be used to generate electricity. The study presented results from a simulation of a 200-household village, incorporating PV, wind, diesel, and battery systems. The most cost-effective setup identified was a battery/converter/diesel generator combination (hybrid) with no contribution from renewable energy sources, as stated in the paper's conclusions. The load-following dispatch technique was utilized in this scenario, along with different cost-effective combinations of diesel generators, PV systems, and converters [112]-[113]. According to the author's conclusion, these power configurations can be effectively deployed in areas where these resources are readily available.

Orissa's Sundargarh district has a hybrid power system comprised of PV, wind, micro-hydro, and a diesel generator, which was designed as a computer model by [13]. Two simulations were conducted in this research: one using a mix of a diesel generator and two primary green energy sources (solar PV-wind), and the other using wind/solar PV, small hydro, and a diesel-run generator. According to the conclusions of the scientists, the scheme is only limited by changes in wind power and home demand. Elhassan et al [14] describe in full the design and construction of a high-efficiency renewable energy-powered electricity system in Sudan's capital of Khartoum. Individual homes and groups of between 10 and 25 households participated in the simulation activity. Single-user PV/battery systems cost more than wind and PV systems for a large group of homes to

produce electricity. Listed here are a few instances of the costs: If there are ten households, the COE is roughly 25.8 SP/Wh, and if there are twenty-five, the COE is approximately 20.1 SP/Wh. Wind turbine hybridization with an off-grid nonrenewable diesel power plant in Saudi Arabia's rural area in the north was shown to be feasible, according to S.Rehman et al. [15]. By merging wind turbines with diesel generators, the project aimed to minimize environmental pollutants and lower operational costs. Wind speed was also included in a sensitivity assessment since it can have a vital influence on the power system over time. The results of the simulation indicated that it would not be feasible to retrofit an existing diesel generator with a wind turbine if the average wind speed was lower than 6 meters per second and the price of diesel fuel was lower than 0.01 cents per litre [34]-[38].

The journal Renewable Energy published research by [16] that examined the possibilities for off-grid electricity in Bhutan's rural areas. The study was conducted at four different locations across the United States. When determining the demanding load, only illumination and communication were taken into account. The principal objective of the article was to increase the efficiency of hybrid power production systems. In Gasa and Lunana, the most cost-effective technology was the PV/battery power generating system, whereas in Getena, the most cost-effective technology was the diesel/battery/PV combination system. Using a wind and battery system was shown to be more efficient at the Yangtse location. As a case study, [17] looked at the economic and technological elements of rural Algerian community's hybrid (wind and diesel generator) projects. The research investigated whether it would be possible to reduce the amount of fuel used by diesel power plants by installing wind turbines alongside those plants' existing systems. When compared to the hybrid system, the diesel-powered plant's cost per litre of between 0.05 and 0.179 dollars is lower, making it the more cost-effective option, according to the author, at wind speeds below 5 m/s. As long as the wind speed is 5.48 metres per second, capacity shortages

are zero percent, renewable fractions are zero percent, and the fuel price is $0.162, a hybrid system is a feasible alternative. In the Democratic Republic of the Congo, hybrid renewable/green energy systems can supply the principal electricity for mobile phone towers, according to Kasukana and colleagues [18]. They were able to prove their viability. Researchers conducted their investigation into the lack of electricity in Kamina, Mbuji-Mayi, and Kabinda, as well as other places. The authors looked into a range of different topologies, including diesel generators, PV-wind systems, 100% PV, and 100% wind schemes. Every possible configuration was examined for its impact on the environment and the economy. For Kabinda's ideal hybrid system, two wind turbines, an 11kW photovoltaic system, eighty-two batteries, and a 7.5kW converter are all that is needed to get the job done. There is an NPC of $196,975 per kWh and a COE of $0.372.

Aside from MATLAB's usage as an optimization tool, the hybrid system configurations were explored with diverse load demands, and the applications, research sites, and meteorological data they used were all unique. To conduct some of the experiments, a diesel-powered generator was used to supply electricity where none previously existed. Other tests were conducted in regions with working electricity. Building a hybrid power system for a particular location requires careful consideration of weather data and the number of houses, service centers, and consumer load profiles. Additionally, the hybrid off-grid power system described in this paper was designed and optimized using the same software. This system will provide electricity to a large number of households for various purposes, including lighting, baking, communication, water and irrigation, and small businesses. Only limited studies at the master's level have been conducted for a small number of families (no more than 200) and in a small number of locations around the country to determine whether or not to implement hybrid power systems in the country. The application, load demand, climate data, location, and sheer quantity of households included in this paper

are some of the ways it differs from other studies that have been conducted [57]-[66].

1.3 Research Motivations

To integrate renewable energy into the present energy mix, there are several reasons for doing so. The urgency to develop and install renewable energy systems worldwide, particularly in India, is primarily motivated by.

1. Increasing need for energy;
2. Depletion of fossil fuel sources;
3. Changes in climate;
4. Belief in inclusive development;
5. Efforts to offer power to those who are currently without it

Solar PV renewable energy systems have recently seen an upsurge in their development and implementation around the globe. The rapid decline in the cost of clean energy technology and the emergence of new renewable markets boost the adoption of renewable-based energy systems. However, ensuring renewables' long-term performance and social advantages is crucial. A key issue is the deterioration of renewable components over time. As the cost of PV modules decreases, the business opportunities for the microgrid concept will improve, as will the range of jobs available in related industries. Human development studies are becoming mandatory due to these initiatives. Reducing emissions using energy systems based on renewable resources also merits consideration. Preliminary simulation studies on design and performance are necessary, as are precise technical and financial concepts for the system under consideration. As a result, the realization and effective usage of non-conventional energy on a broad scale, as well as the ongoing search for other energy sources, pose a major challenge to humanity.

1.4 Objective of research

The following are the goals of the current study, which are based on previous research:

1. Design and simulation of solar PV integrated on standalone model with fixed voltage method, incremental conductance, perturb & observe, Fuzzy, neural network and hybrid Network (NN) & fuzzy based peak power-point tracking control and tested with rapid and continuous varying irradiance conditions and analyzed with the parameters such as rise time and settling time for the converter.
2. Design and simulation of grid-linked PV system with horse herd optimization and hybrid Network & fuzzy-based peak power-point tracking control and tested using rapid and continuous irradiance conditions and also tested with connecting load resistance in a point of common-coupling.
3. Design and MATLAB simulation of Conventional PI, augmented full state feedback controller and Artificial Eco System Optimized Proportional Integral controller for a grid-connected operation of the PV/solar system under non-uniform and uniform irradiance conditions.

1.5 Structure of Thesis

Chapter 1 explains the thesis overview that is appropriate for the reader. A wide range of energy sources has been examined, and their results are reported in this chapter. The thesis's scope, motivation, and structure are all addressed in this section.

Chapter 2 deals with Dissemination of core principles and philosophy of PV systems with different MPPT and energy conversion, and investigation of the Fixed Voltage method, Incremental conductance MPPT, Perturb & Observe MPPT, neural network, fuzzy logic, and hybrid-neural-network & fuzzy-based peak power-point tracking controls to increase solar PV electrical energy production.

Chapter 3 deals with the grid-connected operation of the PV system with horse herd optimization MPPT and hybrid neural network and fuzzy-based MPPT. It also explains the results under uniform irradiance conditions and partial shading conditions.

Chapter 4 investigates the operation of the grid-connected PV system with an Artificial ecosystem-optimized Proportional-Integral controller. The suggested controller is being evaluated in comparison to the conventional proportional-integral controller and AFL controller under uniform irradiance conditions.

In Chapter 5, we will provide final observations and remarks on the grid-connected PV system under non-uniform and uniform irradiance conditions and propose ideas for the scope of future work.

Chapter 2

Maximum/peak power-point Algorithms for Solar- PV system

This chapter elaborates on various algorithms used to determine the peak/max power point of a photovoltaic array system. Many peak power-point approaches have been thoroughly addressed, such as the Fixed voltage MPPT, Perturb and Observe (P&O), Incremental Conductance (InC) approach, fuzzy control-based MPPT method, and Neural Network-based MPPT method.

2.1 Fixed voltage Peak/max power-point algorithm

The peak/max power-point of PV characteristics determines a steady voltage reference across the solar PV (photovoltaic) panel. Figure 2.1 illustrates the principle of fixed PV voltage MPPT.

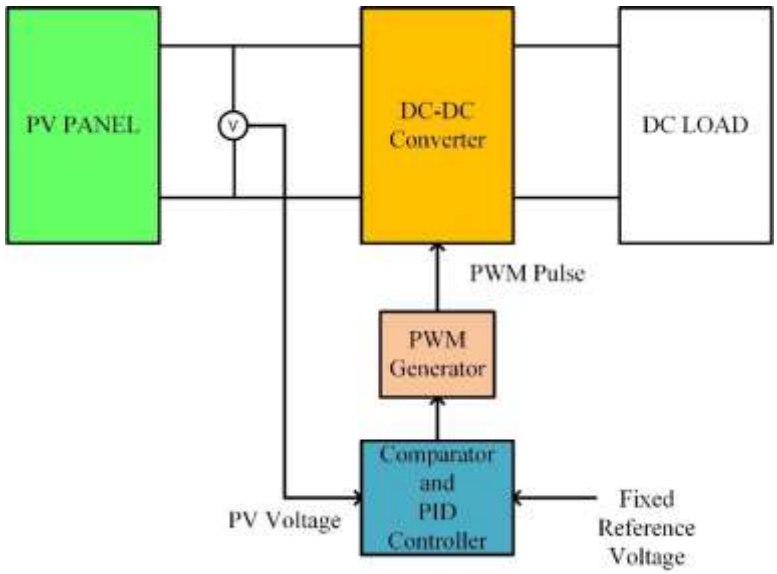

Figure 2.1. Fixed(constant) Voltage Peak(max) Solar PV power point technique

Measurement is done using an onboard voltage sensor, and comparisons are made against the PV panel's peak power point (i.e., volts per square meter).

Using a PID (Proportional Integral Derivative) regulator, the incorrect voltage is corrected. The Proportional Integral Derivative (PID) controller uses the error voltage, sometimes referred to as the duty cycle, to generate the control signal. The PWM generator is applied to handle the duty cycle. Within the PWM generator, the duty cycle is compared to the triangle wave, and the PWM pulse is generated. The power semiconductor switches of the DC-DC converter are activated and deactivated by this PWM pulse. The peak power point can be tracked from the PV panel with this switching pulse and duty cycle.

As a starting point, let's consider that V_{pv} stands for PV voltage, while V_f represents the fixed reference voltage.

$$e(t) = V_f - V_{pv} \tag{2.1}$$

Following the processing of the voltage error by a Proportional Integral Derivative (PID) controller, the following equation serves as the PID controller's output or final result:

$$u(t) = K_p \times e(t) + K_i \int e(t)dt + K_d \frac{de(t)}{dt} \tag{2.2}$$

In this case, the PID controller's Kp, Ki, and Kd represent proportional, integral, and derivative gains, respectively. These controller gains can be adjusted using the Ziegler-Nichols Method or an optimization technique.

Using the PWM generator, the PID controller's output is compared to a triangle waveform, or duty cycle, to determine whether the PID controller is operating properly. The operation of the PWM generator can be represented in terms of the triangle waveform's instantaneous amplitude,

$$\text{T(t).} \quad \begin{array}{c} if\ u(t) > T(t) \\ Pulse = 1 \\ else \\ Pulse = 0 \end{array} \tag{2.3}$$

It is possible to determine the fixed voltage that should be used for a given PV panel's irradiance circumstances by first analyzing its voltage and current characteristics, as shown in Figure 2.2 below.

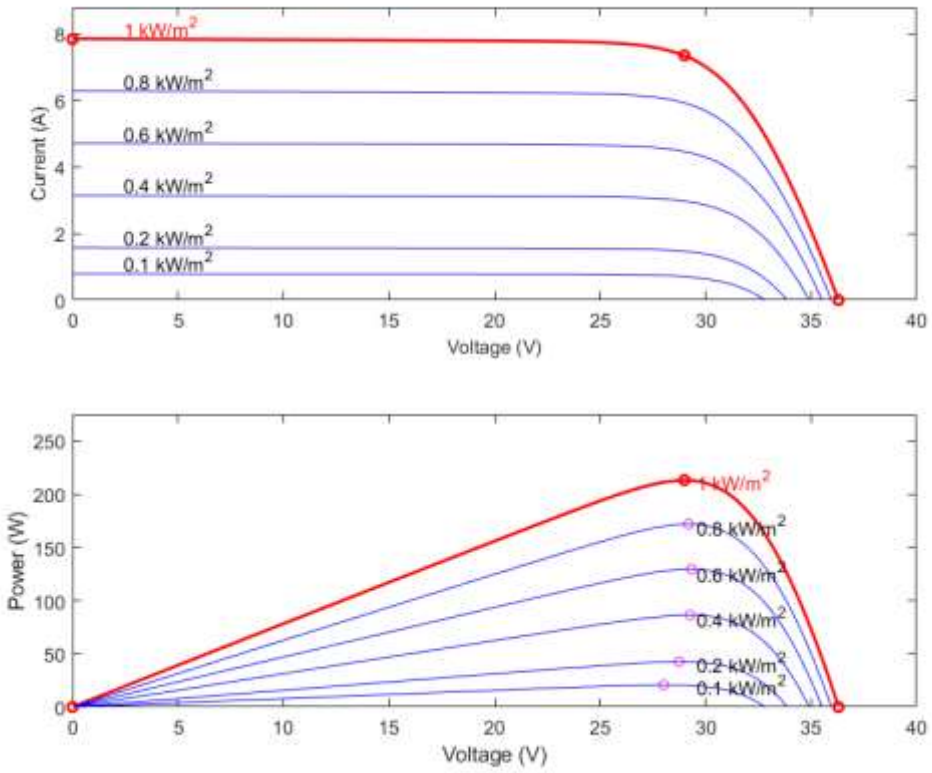

Figure 2.2. Voltage - Current, Voltage – Power characteristics of the typical 250 W PV panel

For different irradiances, after obtaining the voltage (V)-power (P) and voltage (V)-current (I) characteristics, the next step is to measure the PV voltage (V) at the peak power point for various irradiances. An example of typical PV panel power-voltage characteristics is shown in Figure 2.3.

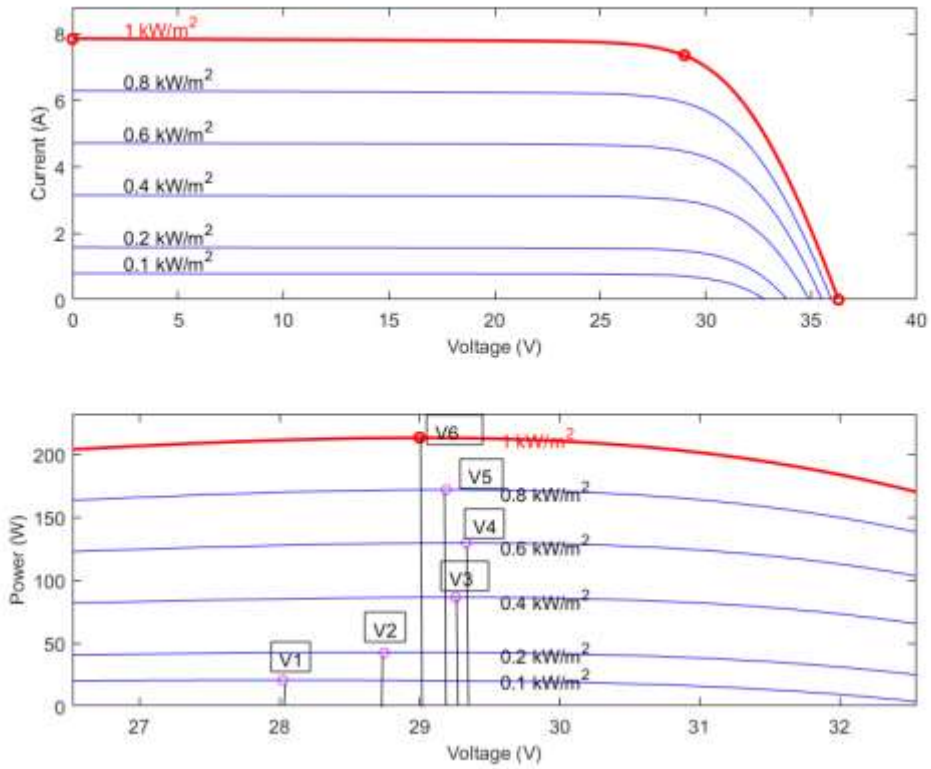

Figure 2.3. Zoomed view of voltage vs power parameters of the typical 250 W PV panel

It is imperative to record the voltage values of V1, V2, V3, V4, and V5, followed by computing their average. This averaged voltage will serve as the constant reference voltage for the Fixed-voltage technique MPPT and can be mathematically expressed as follows.

$$:V_f = \frac{V_1 + V_2 + V_3 + V_4 \ldots + V_n}{n} \tag{2.4}$$

The variable "n" here represents the number of voltage points from the PV array's voltage-power graphs that are used in this calculation.

However, when the cell temperature fluctuates significantly, this approach cannot accurately determine the solar PV panel's peak power output.

2.2 P&O Peak(max) power-locus approach

The Perturb and Observe Peak Power Point (P&O) technique involves maintaining the voltage at the peak power point of every solar photovoltaic panel [24]. This concept of the Perturb and Observe Peak PowerPoint Method is illustrated in Figure 2.4.

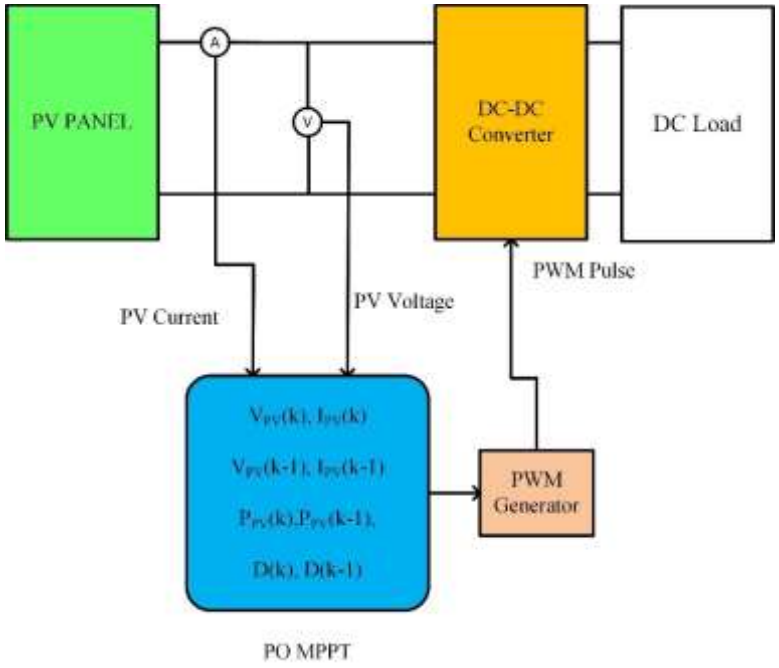

Figure 2.4. P&O Peak power locus technique for Solar PV system

PV voltage and current are measured using voltage and current sensors and detectors. It is then delayed by a sample to retrieve the PV current and voltage values from the preceding sample. PV current and voltage are used to determine the change in power, which is then compared to the previous instant voltage and current [89]. The duty cycle of the P&O MPPT is calculated based on the variation in voltage and power conditions. The PV array's voltage-power characteristics are used to demonstrate how the P&O MPPT works.

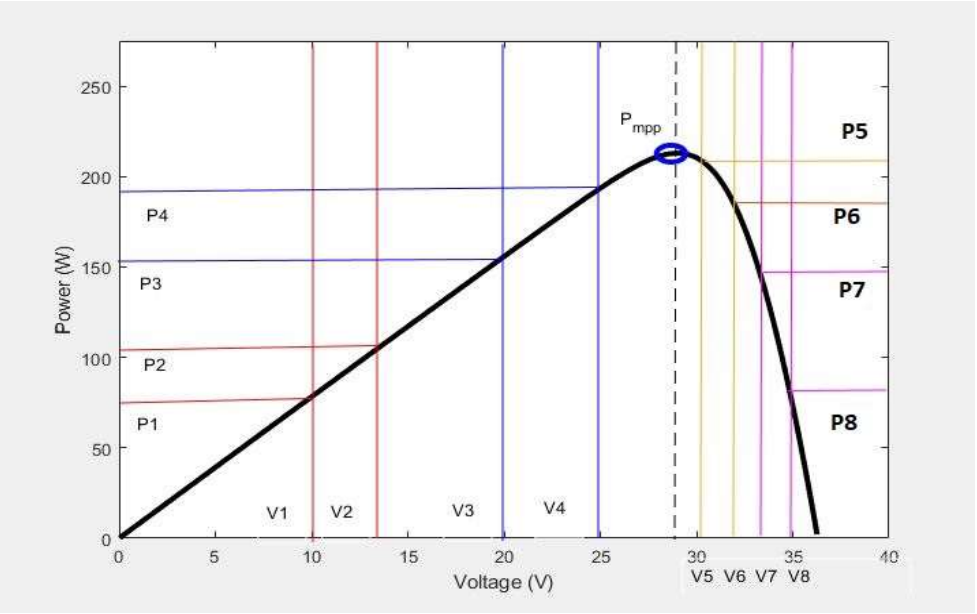

Figure 2.5. Power-Voltage characteristics of a typical 250 W PV Panel

Figure 2.5 shows the typical PV array's voltage-power characteristics. To better understand the P&O MPPT algorithm, four different operating conditions are considered. These conditions are depicted in different colors: the first operating condition is shown in red, the second operating condition in blue, the third operating condition in brown, and the fourth operating condition in pink in Figure 2.5. At the initial operating point, PV voltage changes from V1 to V2, and panel power changes from P1 to P2. To move the power point closer to the maximum power point, the PV voltage should be changed from V2 to another value as long as both P2-P1 and V2-V1 are positive.

$$if\ (P2 - P1 > 0)\ \&\ (V2 - V1 > 0) \quad \{V_{PV} = V2 + \Delta V\} \tag{2.5}$$

The PV voltage is reduced from V4 to V3, and the power changes from P4 to P3 at the second operating point. These conditions require an increase in voltage in the PV panel to shift the maximum/peak power point of the solar PV panel closer to the PV panel's power point (from V3 to V4). This involves a change in power (P3-P4) and a change in voltage (V3-V4)

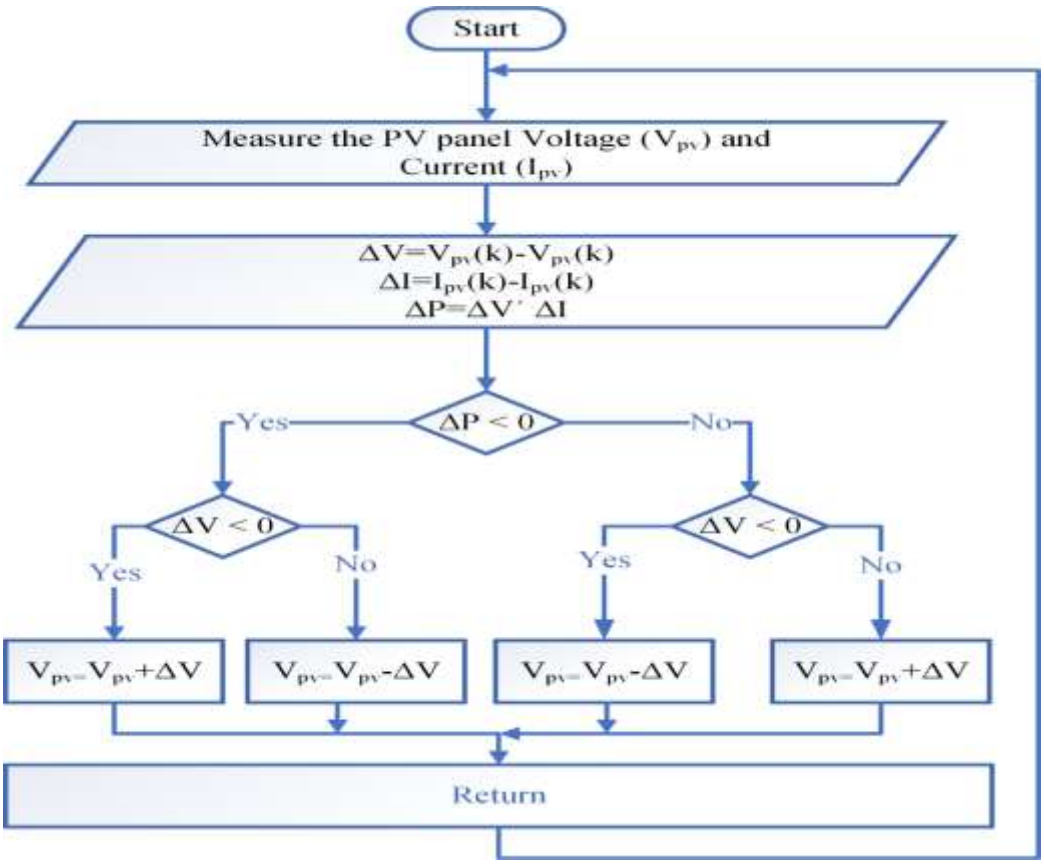

Figure 2.6. Flow Chart for PO MPPT

$$if\ (P3 - P4 < 0)\ \&\&\ (V3 - V4\ < 0)$$
$$\{V_{PV} = V3 + \Delta V\} \tag{2.6}$$

At this third operating point, the PV voltage changes from V5 to V6, and the PV power changes from P5 to P6. The voltage of the PV array should be decreased from V6 to a lower value, as both the change in power (P6-P5) and the voltage variation (V6-V5) are negative under these circumstances.

$$if\ (P6 - P5 < 0)\ \&\&\ (V6 - V5\ > 0)$$
$$\{V_{PV} = V6 - \Delta V\} \tag{2.7}$$

A shift in PV voltage from V8 to V7 and a corresponding decrease in PV power represent the fourth operational point. Changes in power (P7-P8) are positive, whereas changes in voltage (V7-V8) are negative. To move the power

point closer to the maximum or peak power point of the solar panel, the PV voltage should thus drop from V7 to a different value.

$$if\ (P7 - P8\ > 0)\ \&\&\ (V7 - V8\ < 0)$$
$$\{V_{PV} = V7 - \Delta V\} \qquad (2.8)$$

The P&O MPPT algorithm flow chart in Figure 2.6 is based on these four operating circumstances [108]. Since this method oscillates around the PV panel's maximum power point, it takes some time to reach it.

2.3 Incremental conductance Peak power point algorithm

By using this technique, the voltage of the solar PV array is maintained at its maximum power point, depending on PV current and PV voltage, using incremental conductance [24]. The incremental conductance peak power point technique is depicted in Figure 2.7.

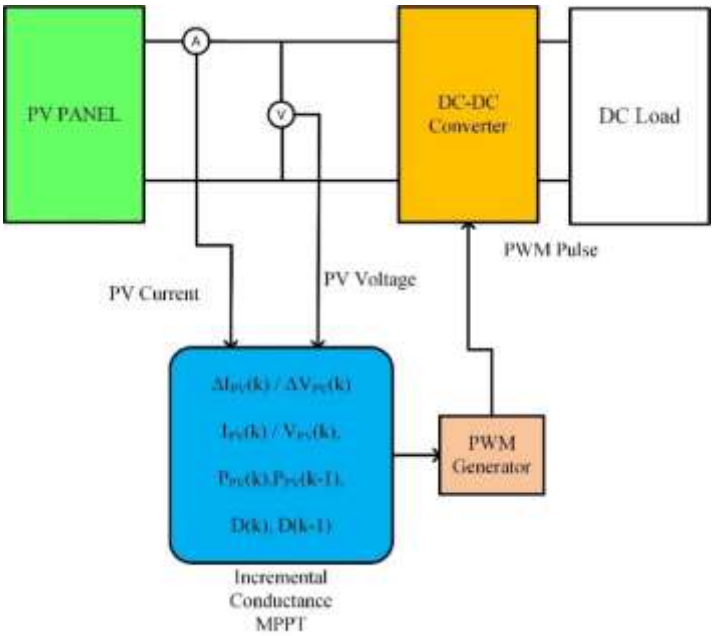

Figure 2.7. (InC) Incremental-Conductance Peak-power-point method for Solar PV system

Current (I) and voltage (V) detectors/sensors are used to measure PV current and voltage in this approach.

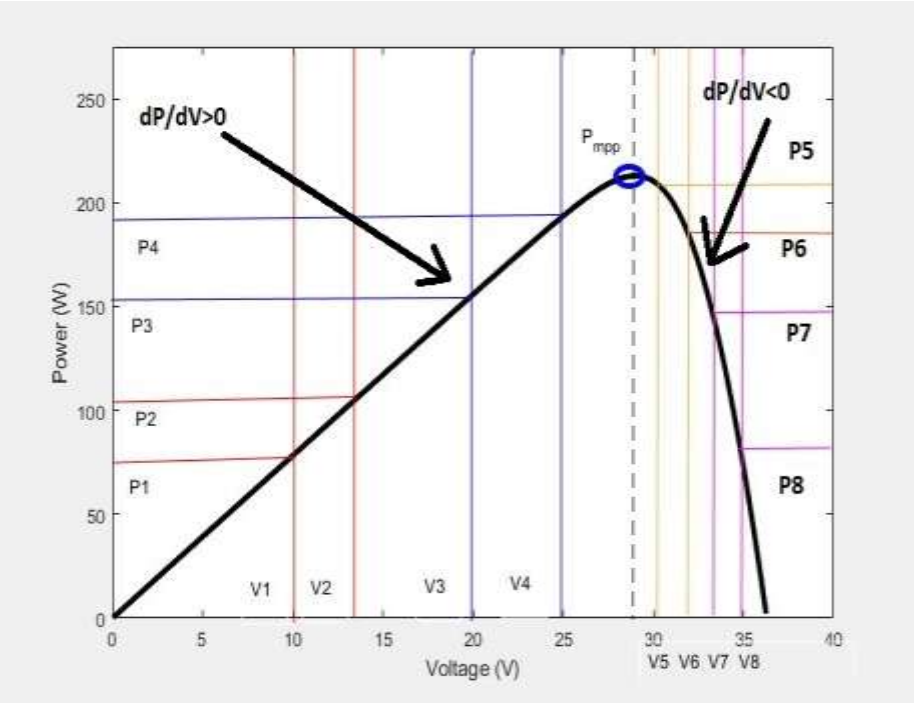

Figure 2.8. Power-Voltage characteristics of a typical 250 W PV-Panel

It is then delayed by a sample to retrieve the PV current and voltage values from the preceding sample. The instant PV current and the preceding instant PV current are used to compute change currents. Based on the previous instant voltage of PV and the current instant voltage of PV, the voltage change is determined. MPPT measures the incremental and direct conductance of the PV panel to determine the duty cycle. The voltage-power characteristics of the PV array are used to illustrate the operation of the InC (incremental-conductance) MPPT [90].

The typical power-voltage characteristics of a PV panel are depicted in Figure 2.8. The incremental conductance MPPT procedure is explained using four different operating conditions, as shown in Figure 2.8. The illustration displays distinct operating points [92], each represented by a unique color. Specifically, the colors red, blue, brown, and pink represent the first, second, third, and fourth operational points, respectively. At the initial operational point, there is a transition in PV voltage from V1 to V2, accompanied by a

corresponding shift in panel power from P1 to P2. Under such conditions, it can be observed that the change in power (P2-P1) and the change in voltage (V2-V1) both exhibit a positive sign. Additionally, the gradient of the power-voltage characteristics is also positive. Under these circumstances, it is recommended to increase the PV voltage from V2 to a value that brings the power point closer to the highest power point of the PV array.

$$\begin{gathered} if\ (\frac{\Delta P}{\Delta V} > 0) \\ \{V_{PV} = V2 + \Delta V\} \end{gathered} \tag{2.9}$$

At the second operating point, the PV voltage decreases from V4 to V3, and the PV power decreases from P4 to P3. This situation involves a negative change in power (P3-P4) and a negative change in voltage (V3-V4), while the slope of the voltage-power characteristics is positively sloped. To reach its maximum output, the PV panel's voltage needs to be increased from V3 to another value.

$$\begin{gathered} if\ (\frac{\Delta P}{\Delta V} > 0) \\ \{V_{PV} = V3 + \Delta V\} \end{gathered} \tag{2.10}$$

At this third operating point, the PV voltage changes from V5 to V6, and the PV power changes from P5 to P6. In these circumstances, the change in power (P6-P5) is negative, and the voltage-power characteristics exhibit a negative gradient. To move closer to the PV array's maximum power point, the PV voltage must be decreased from V6 to another value.

$$\begin{gathered} if\ (\frac{\Delta P}{\Delta V} > 0) \\ \{V_{PV} = V6 - \Delta V\} \end{gathered} \tag{2.11}$$

A shift in PV voltage from V8 to V7 and a corresponding decrease in PV power are observed at the fourth operational point. In these circumstances, the power-voltage characteristics exhibit a negative slope, with a positive sign for power changes (P7-P8) and a negative sign for voltage changes (V7-V8).

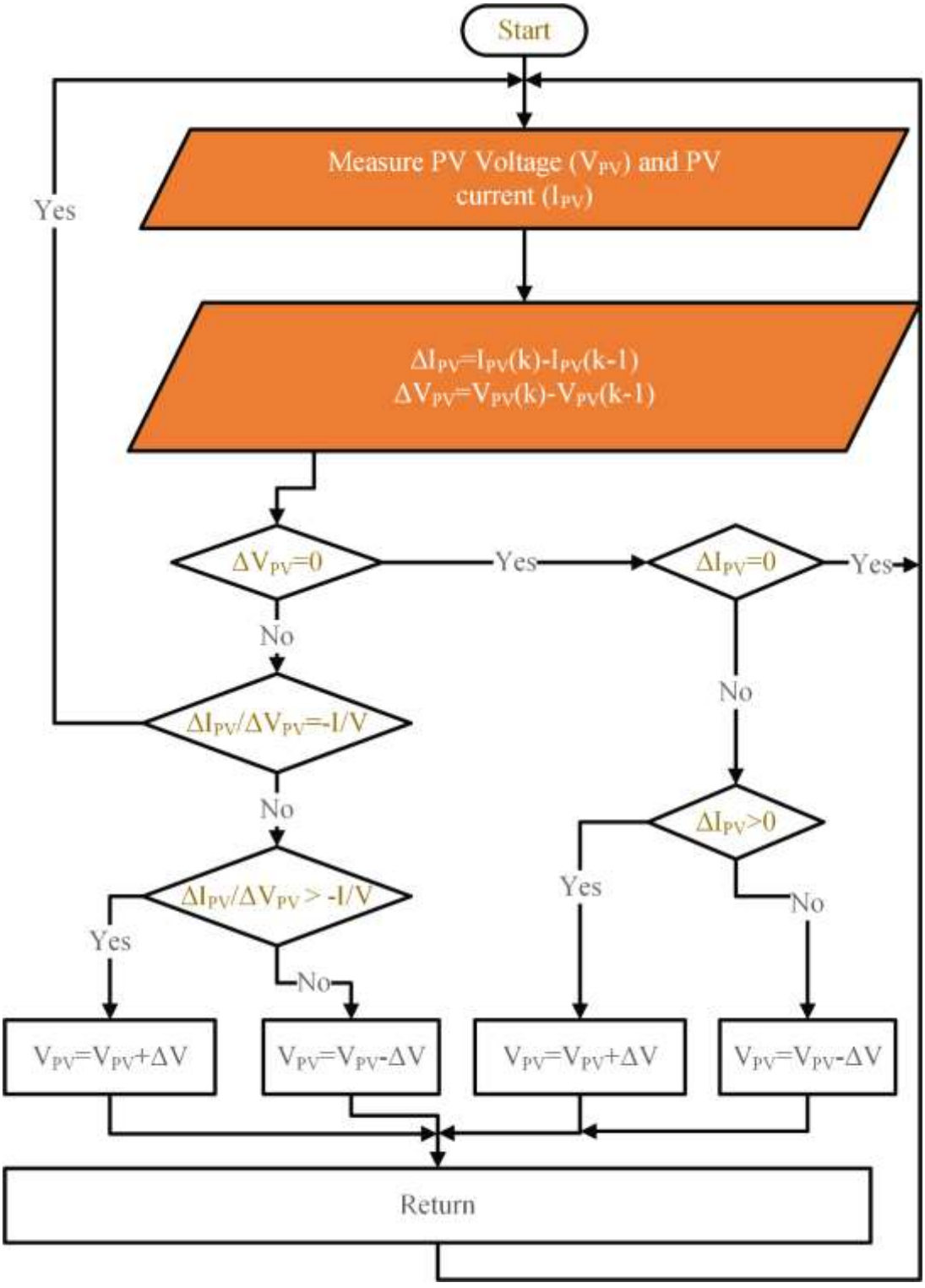

Figure 2.9. Flow Chart for Incremental Conductance MPPT

The voltage needs to be reduced from V7 to another value for the photovoltaic system to reach its maximum energy production

$$if\ (\frac{\Delta P}{\Delta V} > 0)$$
$$\{V_{PV} = V7 - \Delta V\} \quad (2.12)$$

The voltage-power characteristics of the photovoltaic panel can be expressed as a slope., denoted as $\frac{\Delta P}{\Delta V}$.

$$\frac{\Delta P}{\Delta V} = I + V\frac{\Delta I}{\Delta V} \quad (2.13)$$

At its peak, the PV panel's power-voltage characteristics have a slope of zero.

$$0 = I + V\frac{\Delta I}{\Delta V} \quad (2.14)$$

$$\frac{\Delta I}{\Delta V} = -\frac{I}{V} \quad (2.15)$$

Where, $\frac{\Delta I}{\Delta V}$ is the incremental conductance of the PV-panel, $\frac{I}{V}$(current/voltage) is the instantaneous conductance of the PV-panel. Both will equal opposite during peak power point conditions. The power points are on the left side of Toracteristics when$\frac{\Delta I}{\Delta V} > -\frac{I}{V}$. In order to advance the powerpoint towards the maximum (peak) point position, PV voltage must grow to a certain amount.

The power point is located on the right side of the voltage-power characteristics when $\frac{\Delta I}{\Delta V} < -\frac{I}{V}$,. To shift the power point towards the peak location, the PV voltage must decrease to a specific level. The flowchart for the incremental conductance MPPT technique, based on these operating conditions, is shown in Figure 2.9. Since this strategy oscillates around the PV panel's maximum power point, it takes some time to reach it.

2.4 Fuzzy Logic-based MPPT Control Algorithm

To optimize the performance of the photovoltaic array, the MPPT procedure utilizes a fuzzy-based maximum power point tracking approach [26]-[28]. The input to the fuzzy MPPT algorithm includes power slope error (E) and the rate of change of power slope error (E). This algorithm is described by the equation mentioned below.

$$E_N(k) = \frac{\Delta P_N(k)}{\Delta V_N(k)} \tag{2.16}$$

$$\Delta V_N(k) = V_{pvN}(k) - V_{pvN}(k-1) \tag{2.17}$$

$$\Delta P_N(k) = P_{pvN}(k) - P_{pvN}(k-1) \tag{2.18}$$

$$\Delta E_N(k) = E_N(k) - E_N(k-1) \tag{2.19}$$

Where, $E_N(k)$ is the power-error error, power-slope $power - slope$error, $V_{pvN}(k)$ is the current instant voltage(v) of the PV array, $V_{pvN}(k-1)$ is the previous instant voltage of the PV array, $P_{pvN}(k)$ is the current instant PV array

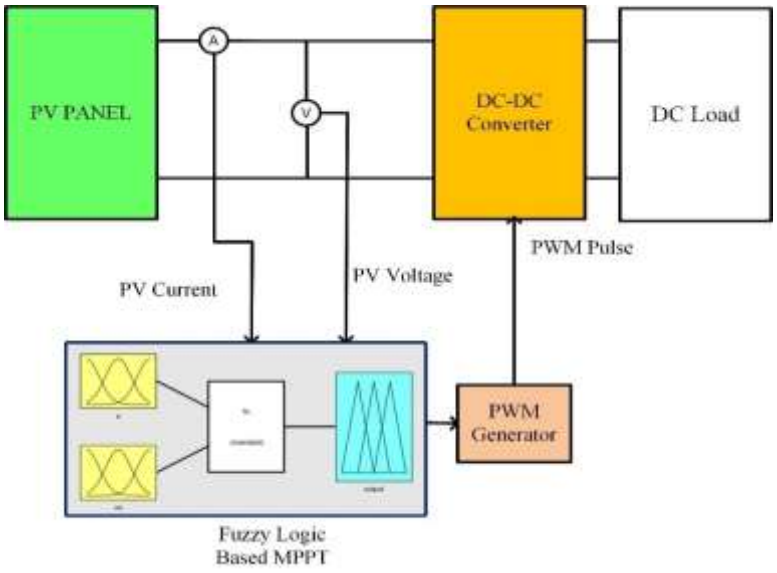

Figure 2.10. Fuzzy-Logic-Based (FLC) Peak-power-point technique for Solar-PV system

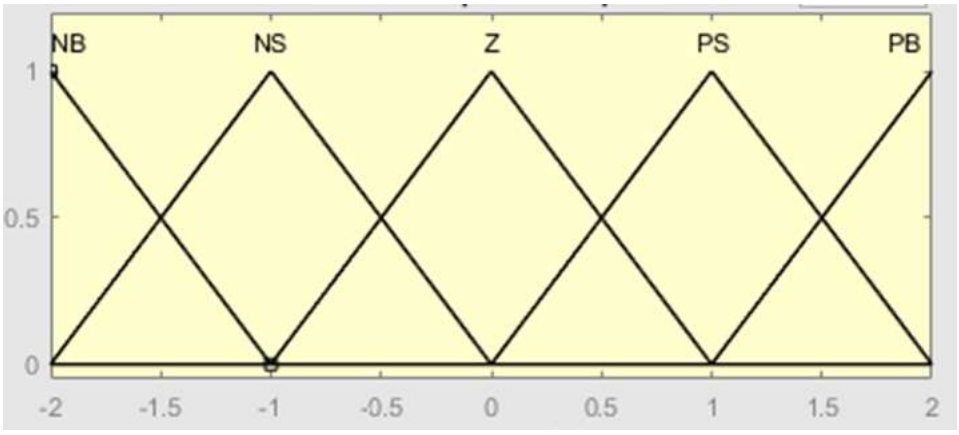

Figure 2.11 Membership function for Error

power, $P_{pvN}(k-1)$ is the earlier instant PV array power, $E_N(k)$ is the current instant power slope error and $E_N(k-1)$ is the earlier instant power slope error.

The Fuzzy MPPT algorithm calculates the duty cycle for the next step based on the power slope error (E) and the rate of change in power (P) slope error. The membership functions for power slope error and the rate of change in power slope error are shown in Figures 2.11 and 2.12. The output of this function can be seen in Figure 2.13.

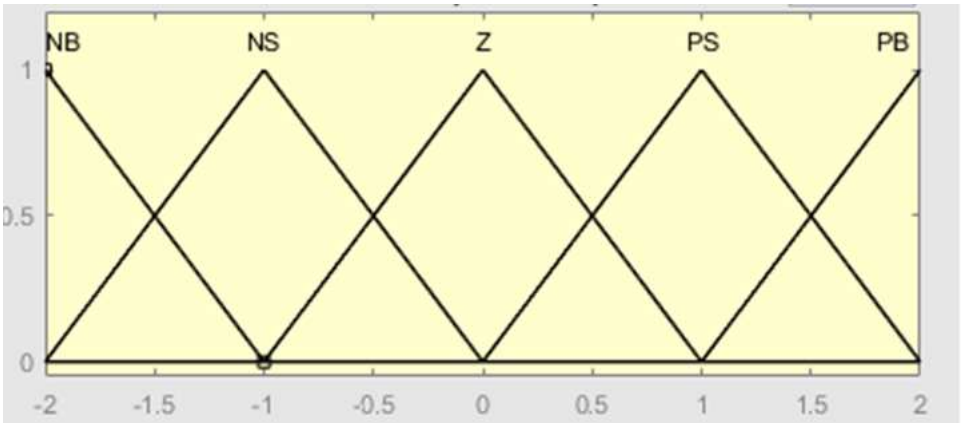

Figure 2.12 Membership function for the rate of change of Error.

The fuzzy implication system MAMDANI is utilized to represent the fuzzy inference-based MPPT. Five membership functions, namely Zero, Positive

Small (Z), Positive Big (PB), and Negative Big (NB), are used to allocate error, rate of error change, and duty cycle (NB).

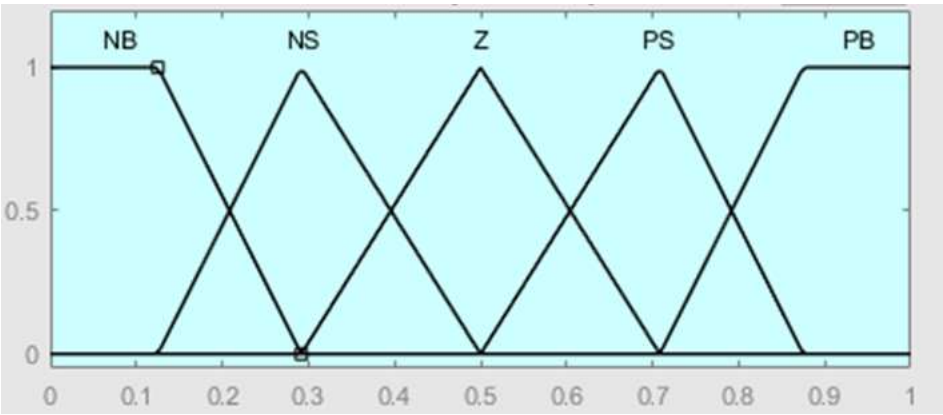

Figure 2.13 Membership function for Duty-Cycle Fuzzy

Table 2.1. Rule base for Fuzzy-Logic MPPT algorithm

$E_N(k)$ / $\Delta E_N(k)$	**NB**	**NM**	**Z**	**PM**	**PB**
NB	NB	NB	PS	PS	Z
NM	NB	NSB	NS	Z	PS
Z	NB	NB	Z	PS	PB
PM	NS	Z	PS	PB	PB
PB	Z	PS	PS	PB	PB

Table 2. I display the rule structure for the twenty-five rules generated in the fuzzy inference system to implement the MPPT algorithm. The Centroid defuzzification method is employed in the fuzzy inference system.

2.5 Neural Network-based MPPTControl Algorithm

Complex or imprecise plant models may benefit from neural networks in nonlinear systems [88]. Solving these puzzles is challenging, whether by hand or through more complicated computer techniques. Weight-initialized ANNs can be regarded as "information experts." The photovoltaic system with neural network MPPT control is shown in Figure 2.14.

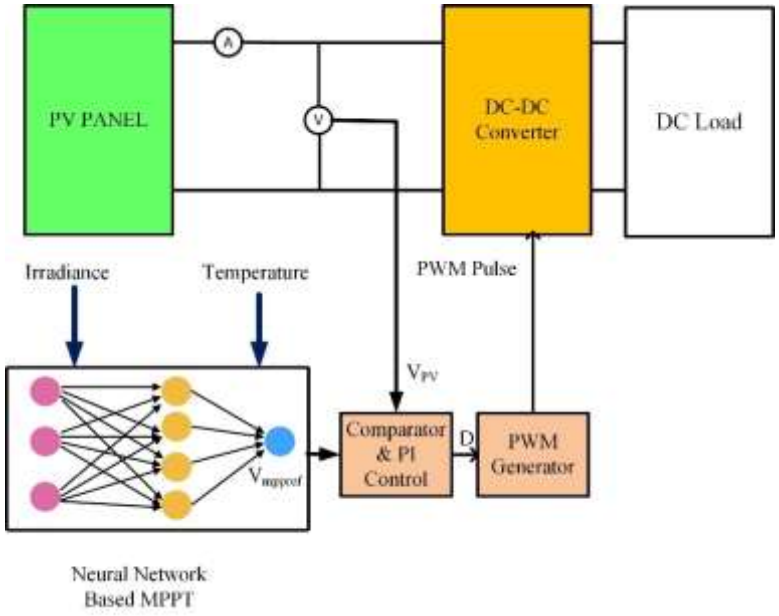

Figure 2.14. Neural-Network(N_N) Based Peak power-point-technique for Solar PV-system

Adopting the concept of adaptive data sets, it is feasible to use an input and output set to learn and accomplish an assignment. During the learning process, neural networks can arrange themselves according to the information they receive. Figure 2.15 exhibits a neural network in the block diagram. The peak PV-array output voltage (Vmppref) is used to train the Neural Network controller, which receives inputs of temperature (T) and irradiance (I). PI(Proportional Integral) Controller is utilized to compare the neural network(NN) output voltage to the PV voltage and create the duty cycle[86]. The duty cycle is determined based on the connection (2.15),

$$D = K_p \times \left(V_{PV} - V_{mppref}\right) + K_i \times \int \left(V_{PV} - V_{mppref}\right) dt \quad (2.20)$$

Using the power slope error (E) and the rate of change in power slope error (P), fuzzy MPPT determines the duty cycle for the next step. Figures 2.11 and 2.12 provide the membership values for power slope error and power slope error rate

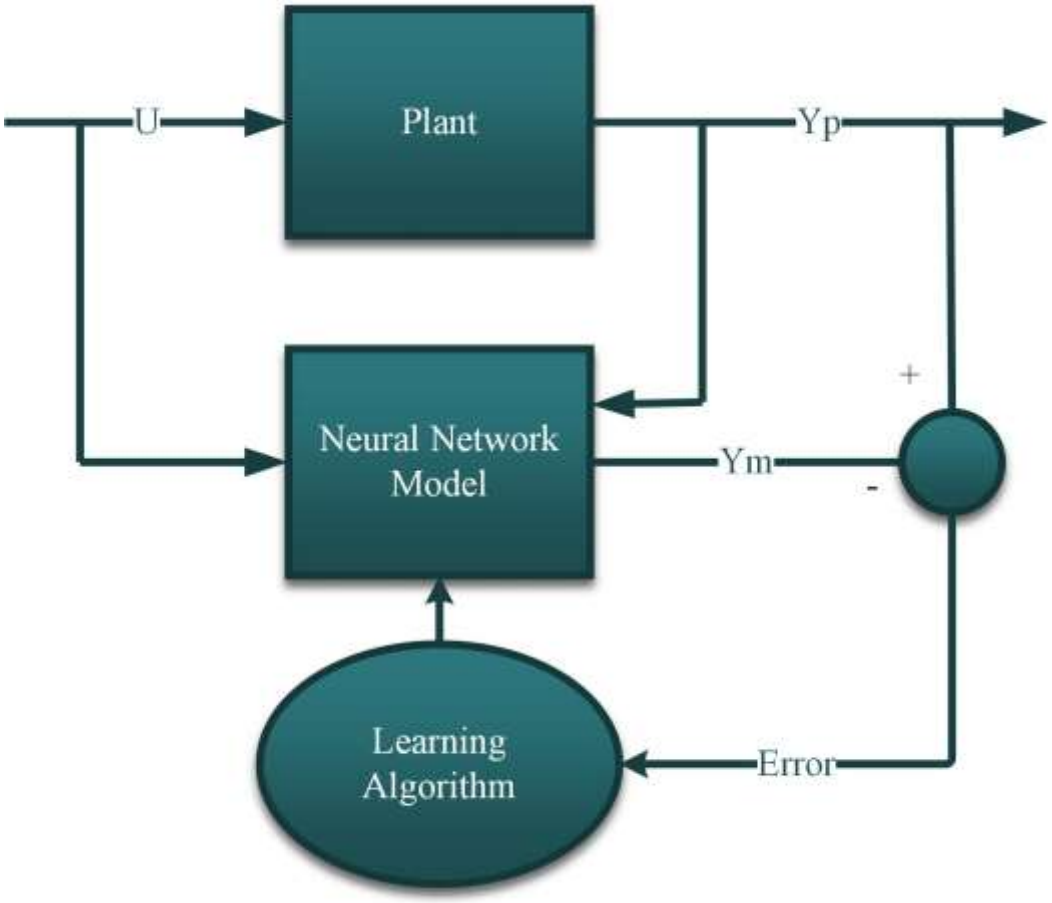

Figure 2.15 Generalized Blocks of ANN-based MPPT Controller

of variation. All the input and output variables required to construct the neural network framework are provided by the data. Before constructing a neural network tailored for a specific task, feed-forward networks are explored. The general architecture of the Feed-forward Network is shown in Figure 2.16. Three methods can be used to build an ANN model:

1. Discover the neurological connections in the wiring of your brain that connect the various patterns.

2. Choose the technique for determining each neuron's initial weight based on the training and learning function.

3. Define an activation function to find the output of a neuron. This stage is described by the term "network architecture" [72].

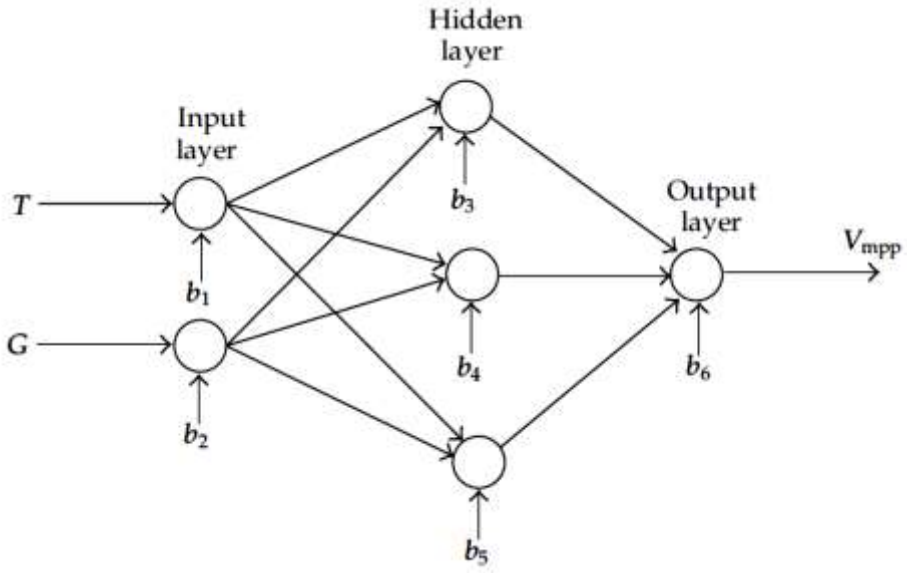

Figure 2.16 Generalized structure of ANN layer

In the hidden layer, there is no standard or norm for the number of neurons. When neurons in a transfer function ANN communicate, the synaptic weight of the connections between them processes the information inside the cell before transmitting it to another neuron. Here's the equation for the net activation input of unit k in the jth hidden layer:

$$net_j = \sum_{i=1}^{n} w_{ij} x_i + \theta_k \tag{2.21}$$

The weight of input neurons and hidden neurons may be calculated by multiplying the independent variables (xi) of the experimental sample and the bias of the hidden nodes (θk). A single neuron receives all the information from the neurons in the previous layer. During training and testing, the output (Oj) of the jth neuron is determined using a hyperbolic tangent sigmoid function in the hidden layer.

$$O_{jt} = \frac{2}{1+e^{-2net_j}} - 1 \tag{2.22}$$

A similar pattern is followed by neurons in both the output and hidden layers. During training, the weights must be adjusted to minimize a predefined error function. Calculating the mean squared error (MSE) can be done in various ways.

$$MSE = \left(\frac{1}{N}\right)\sum_i |t_i - o_i|^2 \tag{2.23}$$

The target value is denoted as t, the output value as o, and the number of neurons in the output layer of the network is N in equation (2.18).

Feed-forward Artificial Neural Networks (ANNs) facilitate unidirectional signal transmission, specifically from the input layer to the output layer. In pattern recognition, feed-forward ANNs that map inputs to outputs are often used [33]. This method is referred to as both bottom-up and top-down classification. The network's architecture involves at least three layers: an output layer, an input layer, and a hidden layer. Neurons are organized into layers, each with a certain number of neurons. Each neuron serves two separate functions. Neurons are assigned to the hidden layer through a process called trial and error. The processor's speed and memory requirements are affected by the network's size. Increased memory and computational needs go hand in hand as the total number of neurons increases. Conversely, fewer neurons may not accurately map the network's functionality. A non-linear activation function was used to increase the

hidden layer's training efficiency. A weighted average of 0.001 weight increment measures the learning rate, which is a crucial consideration in network design. If it is too small, the method's convergence may take a lengthy period.

The following activities are required for implementing the ANN framework:

1. Start by initializing an archive of weights with random values between 0 and 1, which helps evaluate the fitness of solutions using a feed-forward neural network object. Gather training data for ANN-based MPPT by conducting experiments. The input and output matrices for ANN1 are denoted as c and T*, respectively. Training data for ANN2 is derived from load current, losses, and efficiency measurements, all of which have been normalized to values between 0 and 1.

2. Repeat the previously described process until the training error limit is reached or the maximum number of repetitions is reached.

3. Utilize either 25 percent of the training data or a new batch of data for further testing once the algorithm has been trained. The ANN controller uses the Leven Berg-Marquardt approach to train motor operation data. This method was initially devised in 1960 for non-linear least squares issues. The formulae for a weight linking nodes in layer k to nodes in the nth epoch are used to update node weights.

$$\Delta w_{kj}\left(n\right) = \alpha * \delta_{j*} y_k + \mu * \Delta w_{kj(n-1)} \tag{2.24}$$

$$\delta_j = \left(t_j - y_j\right) * y_j * \left(1 - y_j\right) \tag{2.25}$$

Nodes in the previous layer can contribute to the calculation of a hidden layer's error term, as demonstrated in equation (2.18), which involves backpropagation. The Gauss-Newton method is used in combination with gradient descent in this approach. We continue to perform input/output mapping, comparisons, and weight adjustments until we have learned all the data from the training set within an acceptable overall error. Additionally, we evaluate the

overall training matrix error total and assessment error. This method does not require the computation of Hessian matrices to operate.

$$H = J^{t} * J + \mu * I \tag{2.26}$$

Assuming a combination coefficient of μ = 1, we obtain a gradient of G = J^{t} * e, where "I" is the identity matrix. The Jacobian Matrix J holds the differentiation of errors, and the e Matrix contains the network errors. Feed-forward neural networks are utilized in the Back Propagation technique for classification training. Because learning rates alter the weights, errors propagate backwards from the output layer during the process of backward learning. You have two options for changing the weights: working in both batch and incremental modes is possible. This study uses an incremental approach if weights are adjusted right away after the introduction of a training program. To use batch mode, adjust the weights after each training session.

2.6 Hybrid Fuzzy Logical/Neural Network-Based Variable-Step-Size P&O (Perturb and Observe) MPPT Algorithm

Traditional perturb and observe methods often use a constant step-size perturbation, leading to a trade-off between reducing oscillations in PV array power output around the peak power point and achieving a convergent increase in time towards the maximum power point (MPP). A large step size enables a quick dynamic response to abrupt changes in irradiance but results in significant steady-state fluctuations of the PV array power output near the peak power point and power loss. Smaller step sizes help reduce the fluctuation of PV array power output around the peak power point; however, this results in a slower response to abrupt changes in solar irradiance due to their slower dynamic response. Minimum steady-state oscillations and quick dynamic responsiveness require a variable step-size MPPT. To address the limitations of the typical fixed step-size P&O MPPT algorithm, a hybrid fuzzy logic/neural network approach has been

used here to control the step size. Figure 2.17 depicts a hybrid fuzzy logic/neural network-based variable step-size P&O MPPT algorithm.

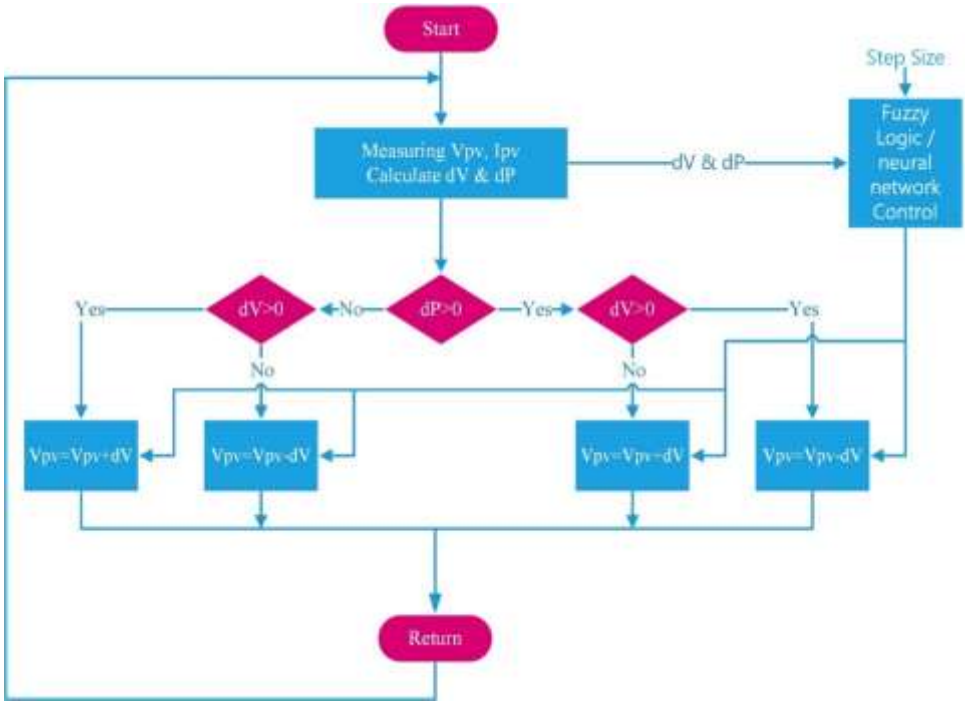

Figure 2.17. Flowchart for hybrid fuzzy logic/neural network (NN) variable step-size MPPT

The terminal current (I) and voltage (V) of the PV array are denoted as Ipv and Vpv, respectively. The proposed variable step-size P&O MPPT algorithm allows for automatic tuning of the PV array's operational point by supplying the associated power converter with a variable reference voltage Vpv. The variable step-size control action, based on Mamdani's fuzzy logic rules, was established using a framework of Max-Min operations. The fuzzy logic controller comprises four main components, as depicted in Figure 2.18. The controller is constructed using "If/Then" logic and includes a set of 25 rules. The fuzzy rule labels, as listed in Table 2.2, are "positive medium (PM)," "positive very small (PVS)," "positive small (PS)," "positive very high (PVH)," and "positive high (PH)."

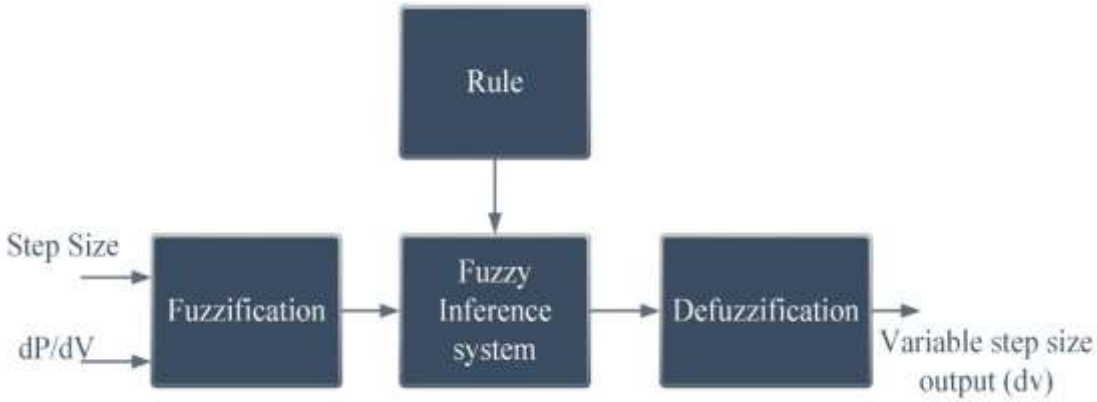

Figure 2.18. FLC-based variable step size control

Table 2.2: Fuzzy step size control rules

	Step Size					
		PVS	PS	PM	PH_p	PVH
dP/dV	PVS	PVH	PVS	PVS	PS	PS
	PS	PVH	PVS	PVS	PS	PS
	PM	PS	PS	PS	PVH	PVH
	PH_p	PS	PVH	PS	PVS	PVH
	PVH	PVS	PVS	PVH	PH_p	PVH

The FLC has two inputs: the variable perturbation step size and the constant perturbation step size of the PV voltage. The fuzzification block assesses the P-V curve's slope and the perturbation step size using the rules laid out in Table 2.2, and these rules are used to make inferences.

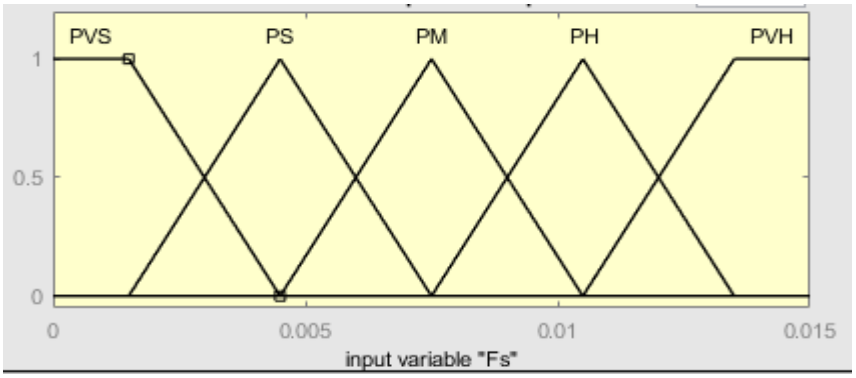

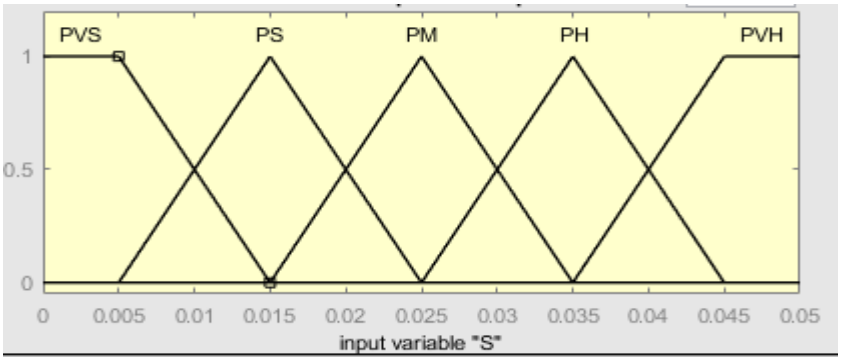

(a)

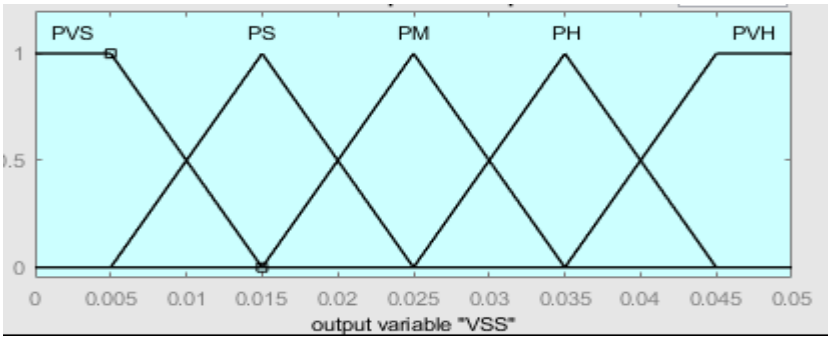

(b)

Figure 2.19 (a) The FLC's input membership function (b) The FLC's output membership function

The control signal for the variable step size controller is formed by de-fuzzifying the fuzzy sets generated by the inference process, using membership functions as illustrated in Figures 2.19(a) and 2.19(b). The output variable step size "dv" of the fuzzy logic controller (FLC) is the specified outcome of each of the 25 rules

it implements. The Centroid defuzzification method is used in the fuzzy inference system.

The Artificial Neural Network (ANN) variable-step-size MPPT is trained using data collected from fuzzy logic-based inconstant step-size MPPT. Finally, the outputs of the FL variable step-size MPPT and neural network (NN) variable step-size MPPT are averaged and sent to the PWM generator to control the DC-DC converter, which is implemented to maximize energy harvesting from the PV cell array. Figure 2.20 demonstrates the representation of a hybrid fuzzy/neural network (NN) inconstant step-size MPPT.

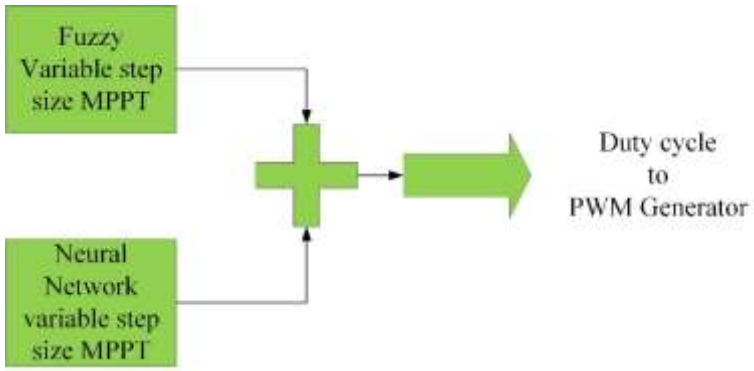

Figure 2.20. Hybrid fuzzy logic / neural-network (NN) variable-step-size MPPT

2.7 DC-DC CONVERTER

This study utilizes a high step-up (DC-DC) converter with an active switching LC network to achieve regulated output for the system. The converter taps into the front-end stage of a photovoltaic (PV) system to obtain the required DC bus voltage. What sets this transformer-less DC-DC converter apart is its simplicity, requiring only a single capacitor and a diode. However, despite its simplicity, it achieves a significantly increased voltage gain by combining the active switched inductor (ASL) and active switched capacitor (ASC) networks in a compound configuration. The key innovation of this converter lies in its use of a switched capacitor instead of a traditional capacitor. This design choice

mitigates the high instantaneous currents associated with capacitors, which is a common drawback in traditional voltage-boosting devices. Figure 2.21 provides a visual representation of the topology of the active switching LC network in the high step-up (DC-DC) converter with active switching, showcasing the arrangement and interplay of the ASL and ASC networks to achieve the desired voltage regulation and boost.

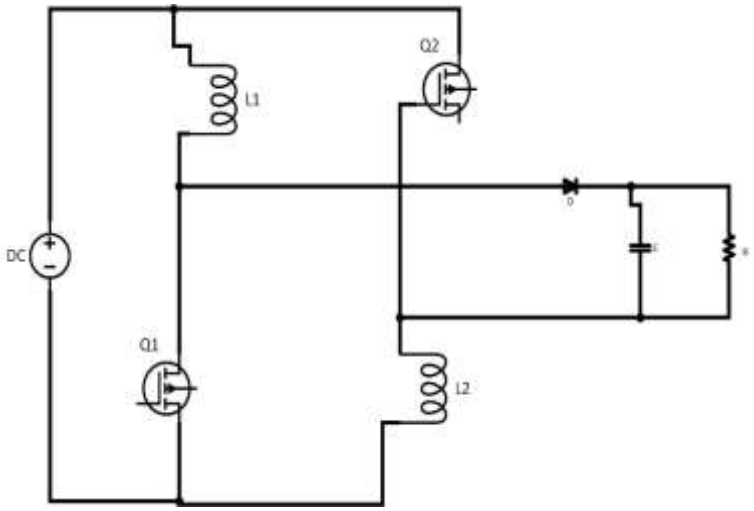

Figure 2.21. High step-up ratio DC-DC converter and an active switching LC network

2.8 SIMULATION RESULTS AND DISCUSSIONS

Evaluations are performed using MATLAB/Simulink, and relevant code is generated. The PV-array model, (DC-DC) Boost converter, and PWM (single-phase inverter) utilize the Fixed-Voltage (FV) method, Perturb & Observe (P&O), fuzzy logic, Incremental Conductance (InC), ANN, Hybrid ANN, and fuzzy-based MPPT techniques for the standalone system [77]-[80]. The (DC to DC) Boost Converter, Solar PV array, and DC Load are listed in Table 2.3. The MPPT's ability to adjust to changing irradiance conditions is assessed.

Table 2.3 Standalone Solar PV system's parameters

S. No	PV Array		DC-DC Boost Converter	
	Description	**Values**	**Description**	**Values**
1	Open Circuit Voltage of the Single Panel	36.3 V	Input voltage	348 V
2	Short Current of the Single Panel	7.84 A	Output voltage	600 V
3	The voltage at Peak Power point	29 V	Input capacitor (C_{in})	1200 µF
4	Current at the peak Power point	7.35 A	Filter Inductor (L)	5 mH
5	Peak Power at the standard test condition	213.5 W	Filter capacitor (C_{out})	1200 µF
6	Number of series panel	12	Switching Frequency	10 kHz
7	Number of Parallel String	40	Power rating	110 kW
8	PV array Power	102.3 kW	Rated current	183.3 amps

The simulation results are analyzed for fixed and varying irradiance conditions of the PV panel. The irradiance of the PV panel varies every 2 seconds from 1000 W/m2 to 800 W/m2, then to 600 W/m2, and finally to 400 W/m2. The simulation result of the Fixed Voltage technique is illustrated in Figure 2.22. The simulation result of the Perturb and Observe method/technique is shown in Figure 2.23. The simulation result of the Incremental Conductance method is shown in Figure 2.24. The simulation result of the Fuzzy MPPT method with triangular membership is shown in Figure 2.25. The simulation result of the Fuzzy MPPT method with trapezoidal membership is shown in Figure 2.26. The simulation result of the

Neural Network (NN) MPPT method is demonstrated in Figure 2.27. The simulation result of the hybrid Neural Network & Fuzzy MPPT method with triangular membership is illustrated in Figure 2.28. The simulation result of the hybrid Neural Network & Fuzzy MPPT method with trapezoidal membership is illustrated in Figure 2.29. In all the above cases the variation of the power is due to the change in irradiation condition of the PV array.

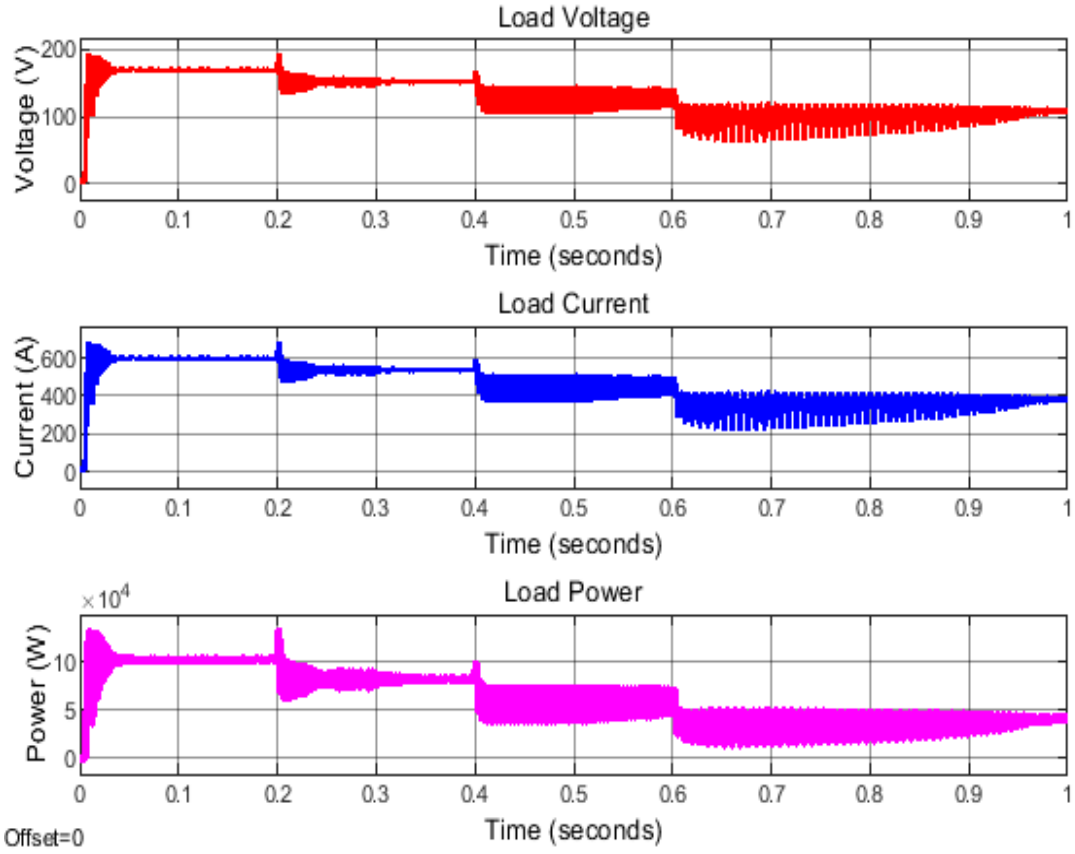

Figure 2.22 Simulation of Solar PV system with Fixed Voltage MPPT Method

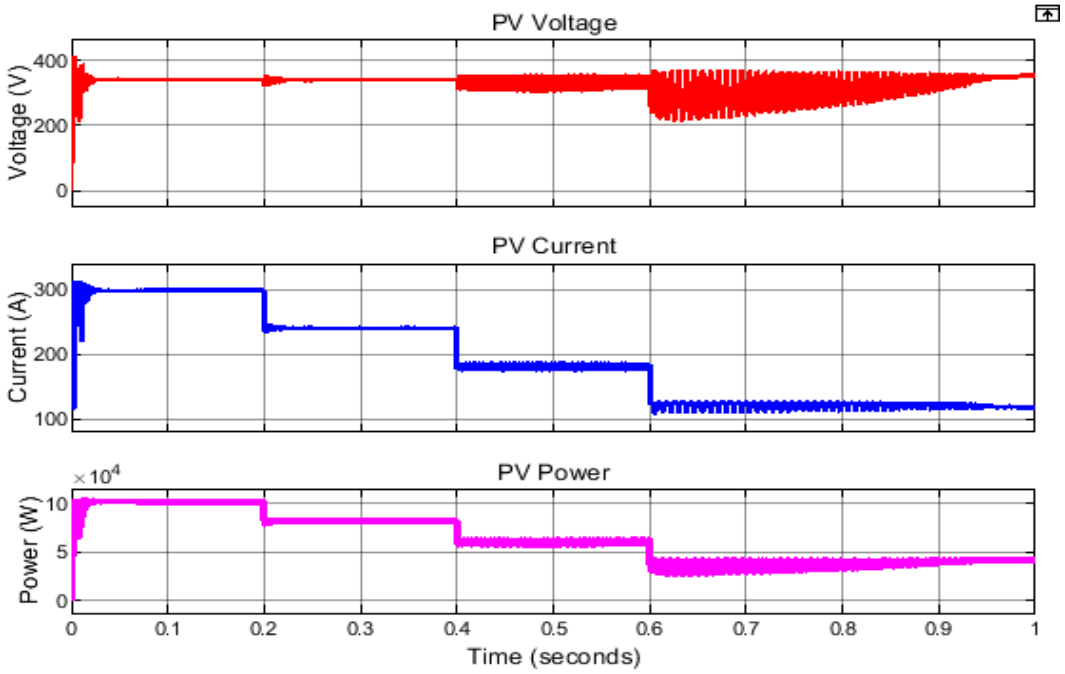

Figure 2.23 MATLAB Simulation of Solar-PV system with P&O MPPT Method

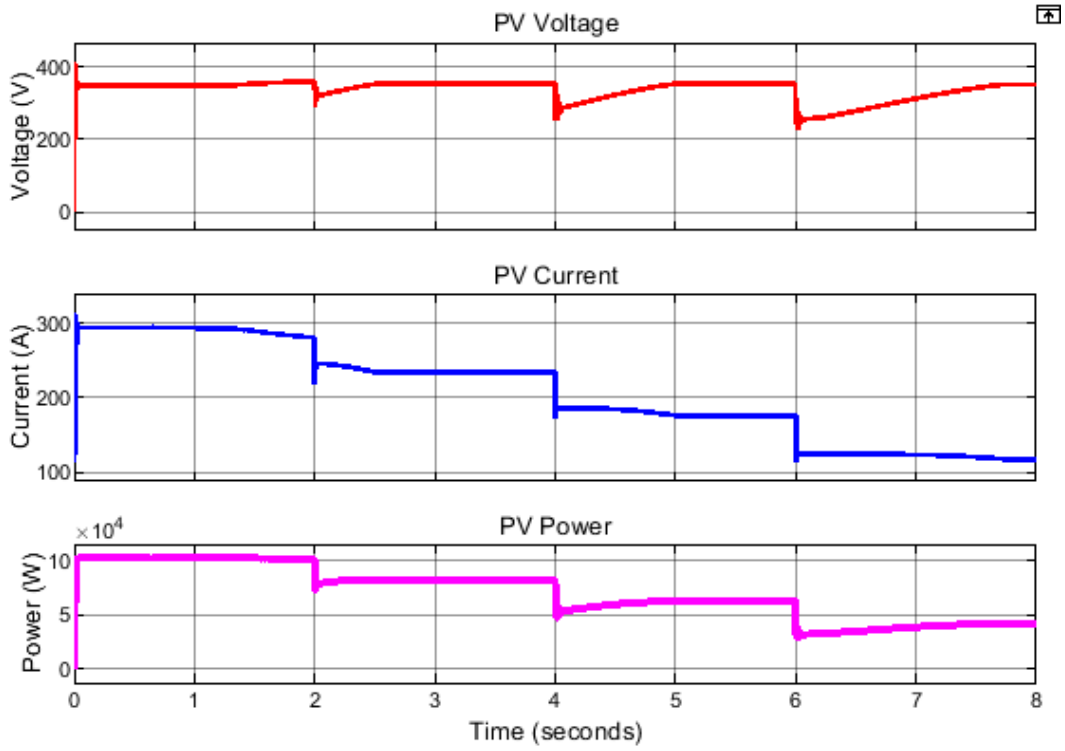

Figure 2.24 Simulation of Solar PV system with Incremental Conductance MPPT Method

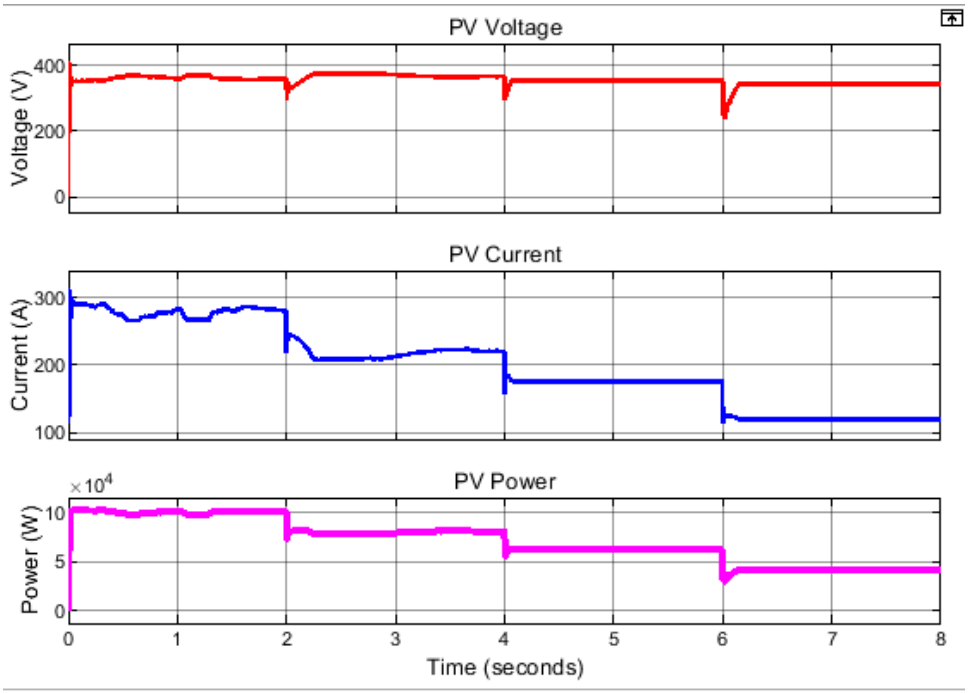

Figure 2.25 Simulation of Solar PV System using Fuzzy Logic MPPT (Triangular Membership)

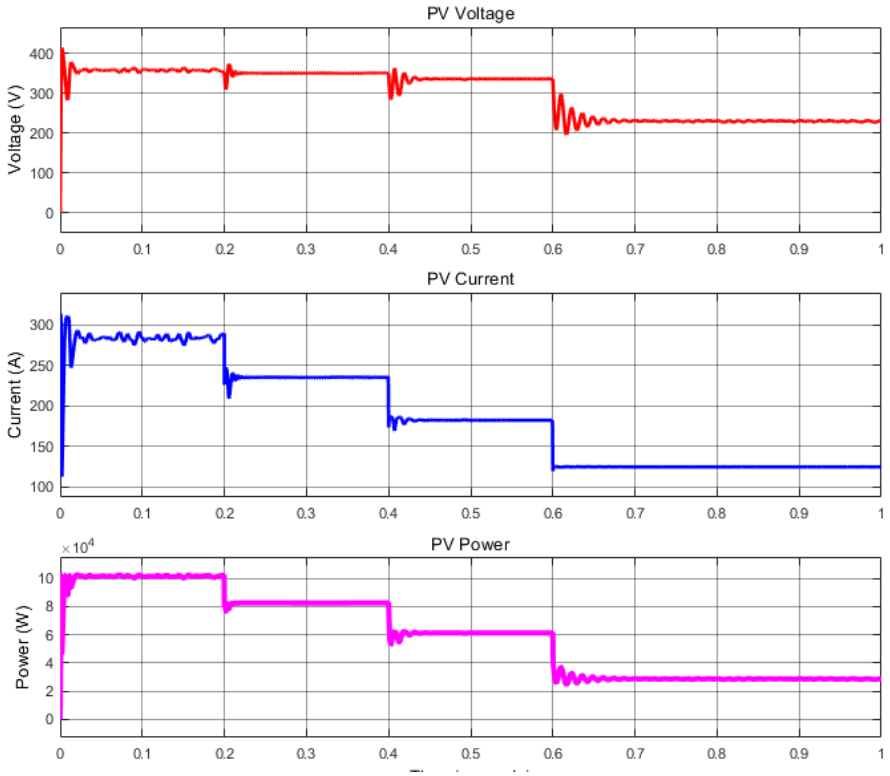

Figure 2.26 Simulation of Solar PV system using Fuzzy Logic MPPT (Trapezoidal Membership)

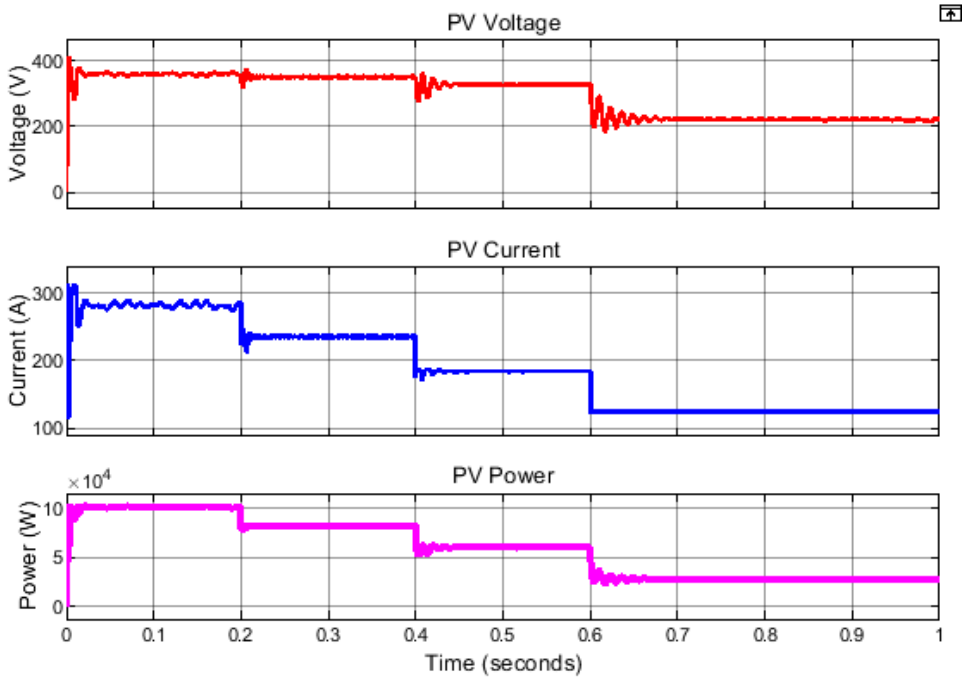

Figure 2.27 Simulation of Solar PV system using Neural Network MPPT Method

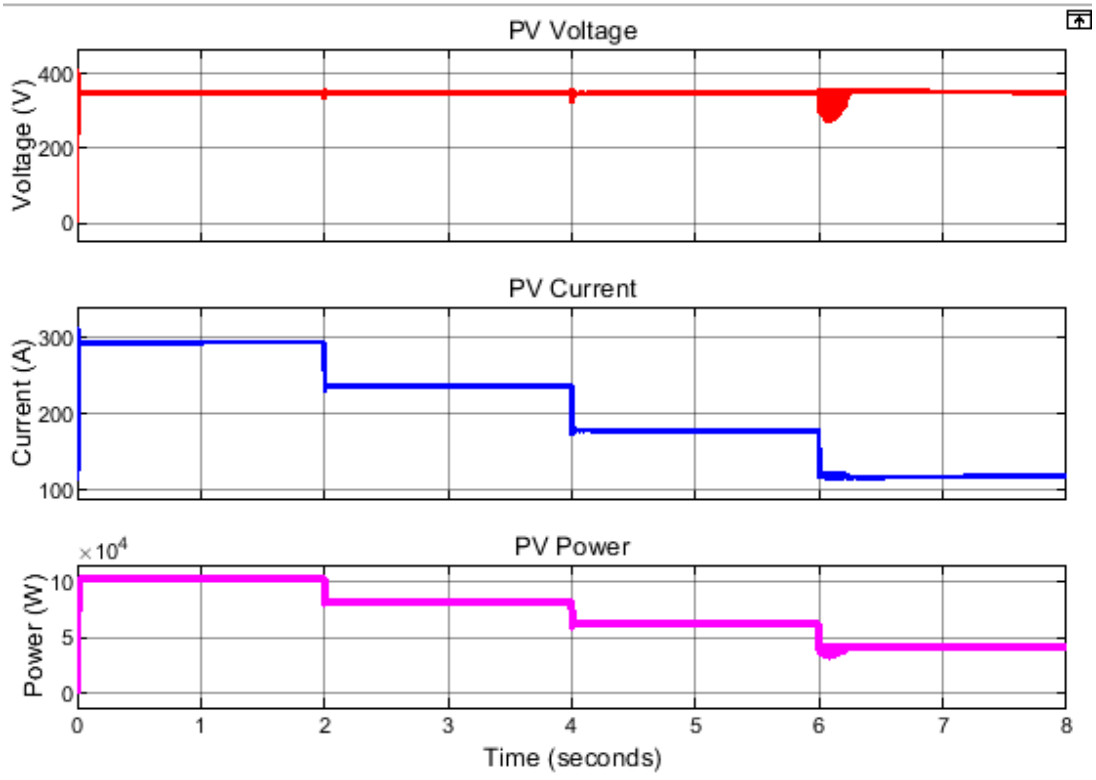

Figure 2.28 Simulation of Solar PV system using Hybrid Fuzzy Neural Network MPPT Method with Triangular Membership Function

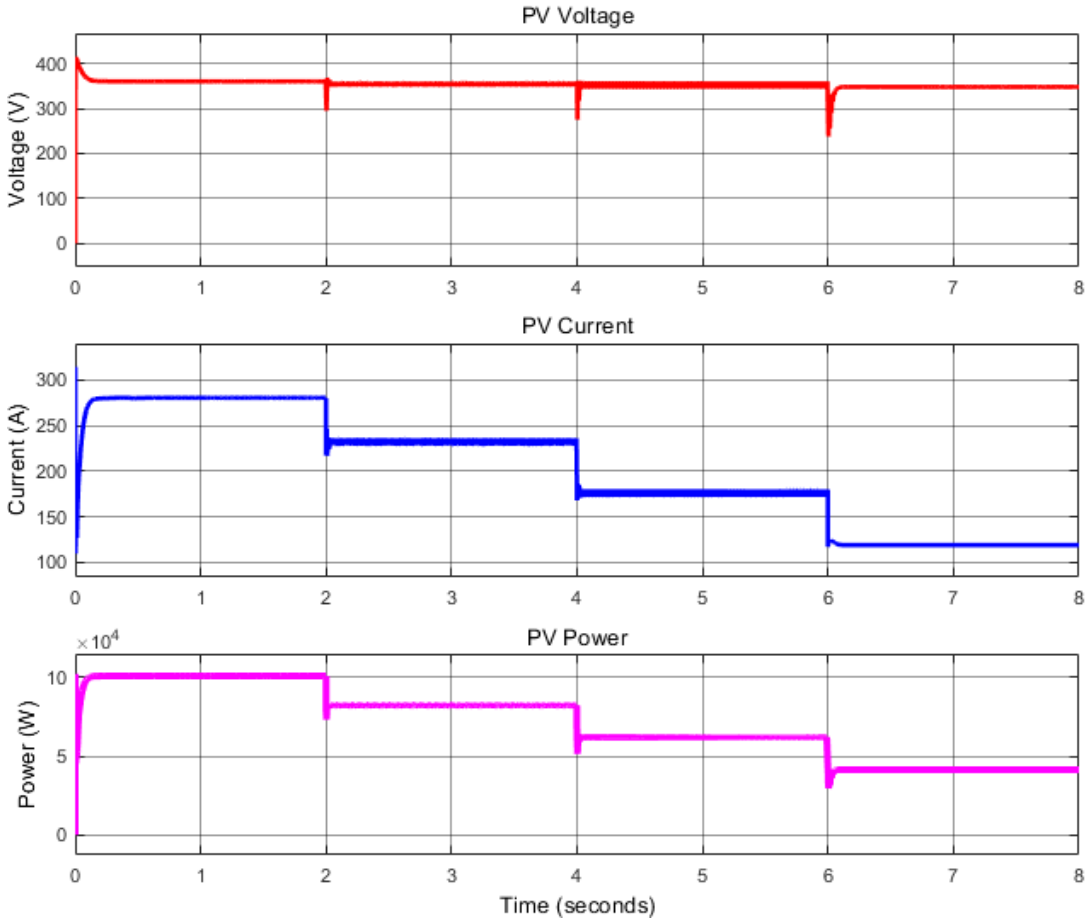

Figure 2.29 Simulation of Solar PV system with Hybrid Fuzzy Neural Network MPPT Method with Trapezoidal Membership Function

Table 2.4 Performance of MPPT at Different irradiance conditions

MPPT	Fixed Voltage	P&O	Incremental Conductance	Fuzzy Logic	Neural Network	**Hybrid Neural Network + Fuzzy (Trapezoidal Membership)**	**Hybrid Neural Network + Fuzzy (Triangular Membership)**
Irradiance W/m^2)	PV Power (kW)						
800	77.33	78.51	78.92	79.12	80.21	**81.78**	**82.22**
600	57.18	58.36	58.61	58.97	59.85	**61.22**	**62.12**
400	36.87	37.95	38.20	38.66	39.54	**40.40**	**41.38**

Table 2.5 Performance of MPPT at 1000 W/m^2 and 25 °C

MPPT	Rise Time (ms)	Settling Time (ms)	PV Power (kW)	Maximum Power ratio (%)
Fixed Voltage	150	190	97.9	95.70
P&O	120	180	98.46	96.25
Incremental Conductance	100	150	98.77	96.55
Fuzzy Logic (Triangular Membership)	80	120	99.72	97.50
Fuzzy Logic (Trapezoidal Membership)	79	119	99.64	97.39
Neural Network	60	80	99.8	97.55
Hybrid Neural Network + Fuzzy (Trapezoidal Membership)	56	45	101.02	98.74
Hybrid Neural Network + Fuzzy (Triangular Membership)	50	70	101.27	99

The performance of several Maximum Power Point Tracking (MPPT) methods at 1000 W/m2 solar irradiation and 25°C temperature is shown in Table 2.4. Tested MPPT approaches include Fixed Voltage, Perturb and Observe (P&O), Incremental Conductance, Fuzzy Logic, Neural Network, and two hybrid combinations of neural network and fuzzy logic with distinct membership functions. Results indicate that the hybrid approach with triangular membership achieves the fastest response times (50 ms rise time and 70 ms settling time) and the highest PV power output (101.27 kW) with a maximum power ratio of 99%. Other techniques exhibit slightly slower response times and lower power outputs, with the Fixed Voltage method showing the slowest response time (150 ms rise

time and 190 ms settling time) and the lowest power output (97.9 kW), yet still achieving a respectable maximum power ratio of 95.70%. These findings provide valuable insights for selecting the most suitable MPPT technique based on specific efficiency and response time requirements for solar power systems.

Table 2.5 provides a comparative analysis of various Maximum Power Point Tracking (MPPT) techniques under different solar irradiance levels. The evaluated MPPT techniques include Fixed Voltage, Perturb and Observe (P&O), Incremental Conductance, Fuzzy Logic, Neural Network, and two hybrid combinations of Neural Network and Fuzzy Logic with different membership functions. Table 2.4 presents the PV power output (measured in kilowatts, kW) achieved by each MPPT method at three distinct irradiance levels: 800 W/m2, 600 W/m2, and 400 W/m2. As the irradiance decreases, the PV power output for all MPPT techniques also decreases, which is expected due to the reduced availability of solar energy. Among the techniques, the Hybrid Neural Network + Fuzzy approach with triangular membership exhibits the highest PV power output at each irradiance level, with values of 81.78 kW, 61.22 kW, and 40.40 kW, respectively. This indicates the effectiveness of this hybrid approach in maximizing PV power production across varying irradiance conditions. Conversely, the Fixed Voltage MPPT method demonstrates the lowest PV power output across all irradiance levels, achieving 77.33 kW, 57.18 kW, and 36.87 kW, respectively. This suggests that the Fixed Voltage method may not adapt well to changing irradiance levels compared to the other MPPT techniques. These findings highlight the potential of the Hybrid Neural Network + Fuzzy (Triangular Membership) method in enhancing the performance of solar power systems by maximizing PV power generation under varying solar irradiance conditions.

2.9 Summary

Fixed Voltage MPPT, neural-network MPPT, Perturb and Observe (P&O) MPPT, Fuzzy MPPT, Incremental Conductance MPPT, and hybrid neural network & fuzzy MPPT were all discussed in this chapter, along with their operation in a PV system. In cases of low irradiance, the Fixed Voltage, P&O, Fuzzy, and Incremental Conductance MPPT methods struggle to accurately track the peak power from the solar PV array, posing an issue. The Incremental Conductance MPPT and Perturb and Observe MPPT methods took a long time to track the PV panel's peak power point accurately. However, under all irradiance conditions, the peak power in the hybrid neural network & fuzzy MPPT method can be quickly and accurately derived without oscillations.

Chapter 3

Grid-connected solar PV system with Horse herd optimization MPPT and Hybrid neural network (NN)/Fuzzy logic-based inconstant step-size MPPT

A grid-linked PV generation system, along with a two-stage grid-linked inverter (DC-AC), is composed of modular blocks. Depending on the scope and depth of the investigation, these building components may take on different configurations. Currently under investigation are PV arrays, a boost controller, an inverter, an LCL filter, a load, and the grid as various building blocks. Figure 3.1 depicts how these building components come together to form the common, yet complex system required for the current research. After a brief overview of each block, the design phase can begin. Subsequently, specific modelling techniques for each block will be discussed. Following that, MATLAB will be utilized to illustrate the entire two-stage, three-phase grid-linked switching model. The problems related to partial shading conditions are presented in [81]-[85].

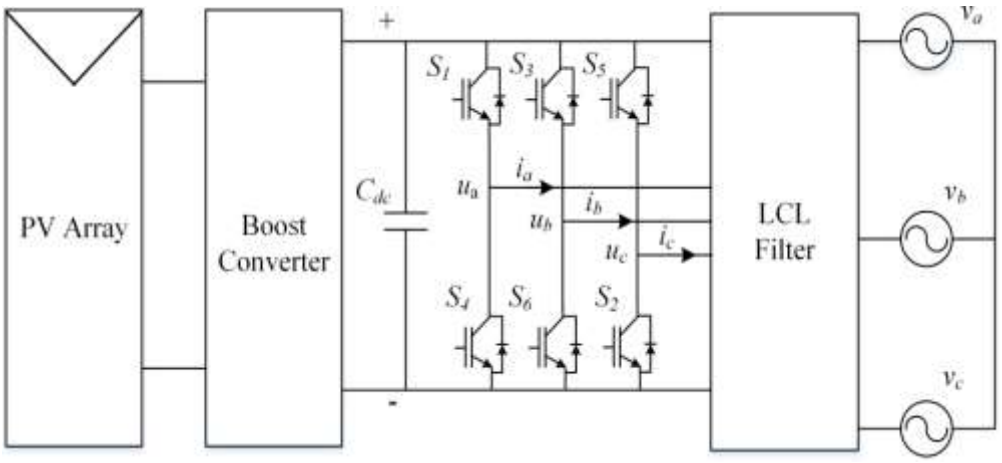

Figure 3.1. Graphical representation of PV grid system

Figure 3.2 illustrates a schematic design of the three-phase grid-linked PV system under examination. The PV system features a two-stage conversion structure, including DC-AC (inverter) and DC-DC stages. The boost converter receives its output from the solar PV and performs two tasks: (1) maximizing the PV's output power, and (2) boosting and regulating the DC voltage at the PV's output.

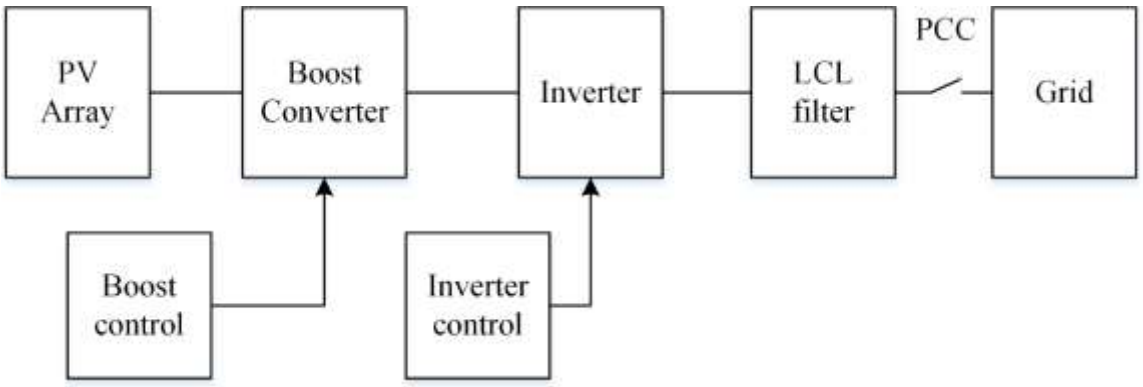

Figure 3.2. Double(two)-stage Grid-connected PV-system

The solar panels experience non-uniform irradiance conditions due to partial shading [73]-[76]. The next step involves the function of the inverter DC-AC conversion, which converts the DC input from the boost converter into AC (variable) power and sends it into the utility grid. LCL filters are installed between the inverter and the power grid to remove high-frequency harmonics from the inverter output. The different parameters are broken down as follows: the DC-link capacitance symbol, the three-phase output currents from the grid-connected inverter (ia, ib, and ic), the grid phase voltages (va, vb, vc), and the LCL filter connected between them. The per-phase voltages outputted by the inverter are Cdc, ua, ub, and uc. This section concludes with simulation results that demonstrate the model's ability to predict steady-state behaviors. The rest of this section focuses on each of the system's blocks.

3.1 Modelling of PV array

The process by which P-n junction diodes produce charge carriers involves the absorption of incident photons with energy levels surpassing their bandgap, which is the distance between two points in a semiconductor's band [21]. In addition to standard monocrystalline solar cells, various polycrystalline types are now available in the market. The features of solar cells are far from ideal; hence, much research is ongoing to find the equations for the solar cells that best describe their actual behavior. In the ideal model, a current source and a diode are connected in series [19].

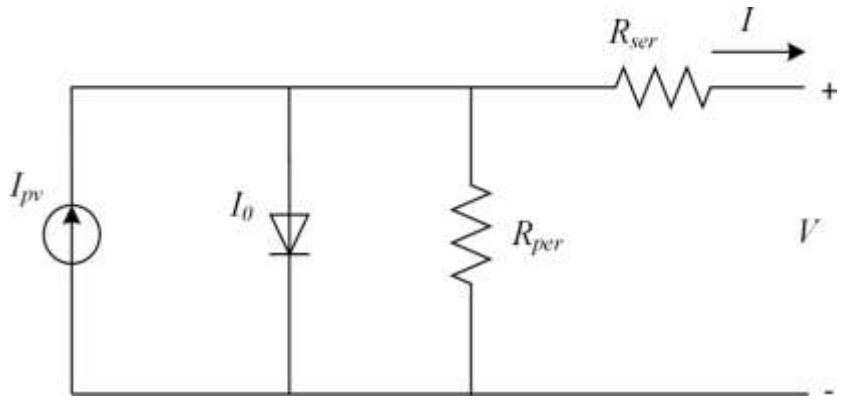

Figure 3.3. Single-cell PV equivalent circuit

In Figure 3.3, the photovoltaic cell's current source and the Shockley diode's behavior can be observed. The total output current of a solar cell is the sum of the diode current and the current source. Figure 3.3 illustrates the ideal solar cell model, including parallel and series resistance. The basic equation for a solar cell is as follows:

$$I = \mathrm{I_{pv}} \mathrm{I_0} \left[\mathrm{e}^{(\mathrm{qV/akT})} - 1\right] \tag{3.1}$$

The diode reverse saturation current is represented by "I_0," the current produced by solar irradiance is represented by "I_{PV}," the cell temperature is represented by "T," and the net current of a solar photovoltaic cell is represented by "I." "q" stands for electron charge, and "K" for the Boltzmann constant. Equation (1)

cannot fully describe the characteristics of a solar cell. Experimental data shows that the model is most accurate when it incorporates both series and parallel resistance.

$$I = I_{pv} - I_0 \left[\left(\frac{V+R_{ser}I}{V_t a}\right) - 1\right] - \frac{V+R_{ser}I}{R_{per}} \quad (3.2)$$

Series resistance is denoted by "Rser," parallel impedance is denoted by "Rper," and the thermal voltage of the PV cell is denoted by "Vt" and is expressed as Vt=kT/q. The series and parallel-combination solar PV cell terminal voltage is denoted by "V." Solar cells exhibit series and parallel resistances, which arise from differences in contact resistance between the cell and the connecting terminal. The number of parallel and series combinations of cells used in a PV array can modify Equation (3.2). Increasing the cells in series boosts the voltage of a PV array while increasing the number of parallel cells increases the current. It's evident how sunlight irradiation and temperature influence the amount of light-generated current by examining Equation (3.3).

$$I_{pv} = \left(I_{pv} + K_i \Delta T\right) \frac{G}{G_n} \quad (3.3)$$

Because the series resistance of the solar cell is significantly lower than the parallel resistance, it is hypothesized that the short-circuit current approximates the nominal photovoltaic current.

Table 3.1. Specification of PV arrays 1 & 2

PV Array 1 & 2		
S.No	**Description**	**Values**
1	PV open-circuit-voltage (V)	51.5V
2.	PV Short-circuit-current (A)	9.4A
3.	Current @ maximum power point (A)	8.13A
4.	Voltage @ maximum power point (V)	43V
5.	Series PV panel	3
6.	Parallel String	1
7.	PV array Rating (W)	1048.77

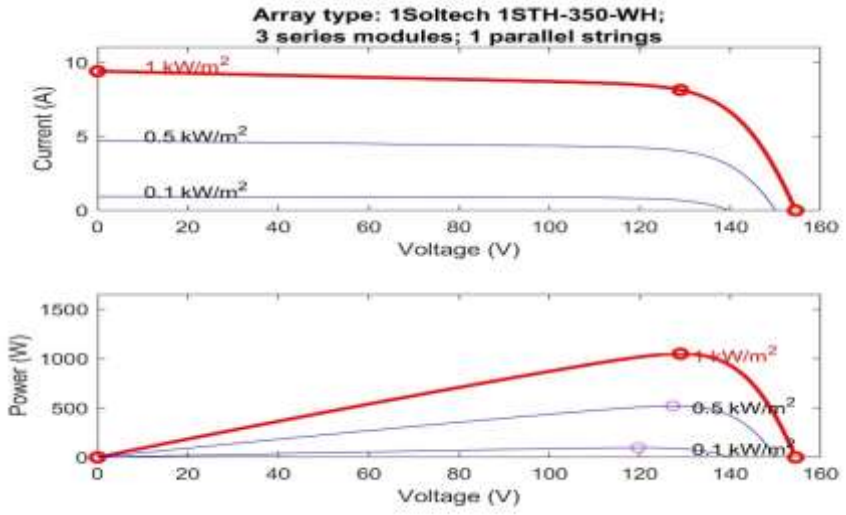

Figure 3.4. PV and IV Characteristics of PV array.

The photovoltaic generated current is represented by "I_{pvn}," the current coefficient is represented by "k_i," the temperature difference between actual and nominal is denoted by "ΔT," actual solar irradiance is denoted by "G," and standard solar irradiance is denoted by "G_n." Three PV arrays were used in the study, and Table 3.1 lists the specifications of a photovoltaic array. PV array 1

and PV array 2 each consist of 3 series and 1 parallel string [107]. The PV and IV characteristics of the PV array1 are shown in Figure 3.4.

3.2 Maximum(peak) Power-Point Tracking

Maximizing a solar panel's power output is crucial for solar power generation. A solar cell's non-linear behavior prevents it from producing electricity at a steady rate. Moreover, the power properties of the solar cell continually change due to external conditions like temperature and irradiance. To ensure solar cells operate at maximum power, their output voltages should be monitored closely so that, under varied irradiance and temperature conditions, they are near the peak power point. MPPT can increase a solar cell's total efficiency by capturing the PV array's peak output during regular daylight hours. MPPT algorithms are gaining popularity due to their upgraded versions and excellent efficiency [93]-[99].

The algorithm used by the MPPT controller includes several choices. The three most common methods are the fuzzy logic controller, perturbation and observation (P&O), and incremental conductance technique (IC). Techniques vary in terms of speed, intricacy, and stability. The approach used will depend on the needs of the system's design. In this system, the Horse Herd Optimization-based maximum power-point tracking algorithm and the Hybrid Neural Network (NN)/Fuzzy Logic based on constant step size MPPT have been used and compared in the chapter for grid-connected PV systems [39]-[44].

3.3 Horse Herd Optimization

To make the Horse Optimization Algorithm function, we looked into how horses act in their natural habitats. It is common for horses to exhibit grazing (A), hierarchical (B), social (C), imitation (E), and defence mechanisms (D) in roam behaviour (F). Consequently, the algorithm was inspired by the six distinct behaviours exhibited by horses at different stages of their development.

The equation expresses the movement imparted to horses at each repetition.

$$Z_i^{iter,AGE} = S_i^{iter,AGE} + Z_i^{(iter-1),AGE}, AGE = \alpha, \beta, \gamma, \delta \qquad (3.4)$$

$Z_x^{iter,AGE}$ displays the location of the ith horse, AGE shows the horse's age choice, Iter is the current repetition, and $S_i^{iter,AGE}$ shows the horse's velocity vector. At diverse ages, horses display a variety of diverse behaviours. Typically, a horse's lifespan is between 25 and 30 years old. Horses aged 0–5 years, 5–10 years, 10–15 years, and more than 15 years are denoted by α, β, γ, and δ, respectively, in this regard. To choose the age of horses, a full matrix of replies should be undertaken iteratively. By sorting based on the best replies, it is possible to choose 10% of horses from the entire matrix for added consideration. The following 20% of respondents belong to the category. Thirty percent of the remaining horses are chosen, while forty percent are selected as horses. Equine behaviour has been computationally simulated to determine the horse's speed.

They are herbivorous and graze on grass, fodder, and other plants. They spend 16 to 20 hours a day grazing on pasture, with little time for rest. It's called "continuous eating" when you're constantly eating all the time. In the pasture, perhaps you've seen the mares and their foals. For each horse, the HOA algorithm uses a coefficient of grass to estimate the grazing area surrounding the animal. Horses can be found grazing in the fields at any age. Grazing is mathematically implemented according to the following formula.

$$A_i^{iter,AGE} = {a_i}^{iter,AGE} \times (U + R \times L) \times \left(Z_i^{(iter-1)}\right), AGE = \alpha, \beta, \gamma, \delta \qquad (3.5)$$

$${a_i}^{iter,AGE} = {a_i}^{(iter-1),AGE} \times w_a \qquad (3.6)$$

The horse's propensity to graze is shown by $A_i^{iter,AGE}$, where Wa is the horse's motion parameter. wg per iteration is less linear when this factor is taken into account. This formula yields a range of values from 0 to 1, with R being a number

drawn at random within that range. Consider U and L values are 1.05 to 0.95, with the constant W_a equal to 1.5 for entirely age groups.

In the wild, horses aren't allowed to roam free. Following a leader, which is a common occurrence in human life, is what they do. The law of hierarchy states that a mature horse or stallion is also accountable for leading the herds of wild horses. The tendency of a herd of horses to track the greatest experienced and influential horse is considered by the coefficient h in HOA. In this instance, during the Central Ages (aged between 5 and 15 years), research has revealed that horses track the law of the ladder as expressed in the following equation.

$$B_i^{iter,AGE} = b_{iter}{}^{iter,AGE} \times \left(Z_*^{(iter-1)} - Z_i^{(iter-1)}\right), AGE = \alpha, \beta, \gamma \tag{3.7}$$

$$b_i{}^{iter,AGE} = b_i{}^{(iter-1),AGE} \times w_b \tag{3.8}$$

The best horse location has a significant impact on the velocity parameter, as shown by $B_i^{iter,AGE}$, and $Z_*^{(iter-1)}$ displays the exact location of the best horse.

Horses need to be among other animals and may even share a home with them. Since horses are preyed upon by predators, herd life provides them with a sense of safety. Survival and emancipation are both made easier by plurality. Fights among horses are common due to their social characteristics, and excitability is a result of their unique traits. Some horses enjoy spending time with other creatures like cows and ewes, but they dislike being alone. This behavior is seen as a tendency to move toward the average position of other horses. Young horses (aged 5–15 years) show a keen interest in the herd, as demonstrated by the following equation:

$$C_i^{iter,AGE} = c_{iter}{}^{iter,AGE} \times \left(\left(\frac{1}{N}\sum_{k=1}^{N} Z_k^{(iter-1)}\right) - Z_i^{(iter-1)}\right), AGE = \beta, \gamma \tag{3.9}$$

$$c_i{}^{iter,AGE} = c_i{}^{(iter-1),AGE} \times w_c \tag{3.10}$$

$C_i^{iter,AGE}$ is the ith horse's social signal vector, and ${c_i}^{iter,AGE}$ represents the ith iteration's orientation toward the herd. With each iteration, ${c_i}^{iter,AGE}$ lowers by a w_c factor. Both the number of horses and the age choice of each horse are shown in the N field. As part of the sensitivity analysis of parameters, we calculate the c coefficients for $\beta and\ \gamma$ hand and horses, respectively. It's common knowledge that horses learn from each other, both good and bad habits, such as how to locate a pasture.

Equine mimicry is also considered in the current algorithm. A young horse's desire to imitate others persists throughout its life and is expressed as the following equation:

$$E_i^{iter,AGE} = {e_{iter}}^{iter,AGE} \times \left(\left(\frac{1}{pN} \sum_{k=1}^{pN} Z_k^{(iter-1)} \right) - Z_i^{(iter-1)} \right), AGE = \gamma \tag{3.11}$$

$${e_i}^{iter,AGE} = {e_i}^{(iter-1),AGE} \times w_e \tag{3.12}$$

$E_i^{iter,AGE}$represents the horse's path toward the mean of the finest horses in the area at $Z_k^{(iter-1)}$ places. The number of horses with the greatest placements is represented by pN. Ten percent of the horses have been nominated as p. According to the preceding example, w_e is the reduction factor.

Predators have historically threatened horses, shaping their behaviour accordingly. They exhibit a fight-or-flight response to protect themselves, with escape being their primary instinct. Additionally, they may buck if caught. Horses fight for resources like nutrition and water to fend off competitors and escape dangerous conditions, such as wolves, by instinct. In the HOA algorithm, a horse's defensive system works by avoiding horses that provide incorrect responses. Factor "d" plays a crucial role in their defence strategy. As mentioned earlier, horses must either flee or confront threats. This defensive strategy is utilized by both young and adult horses throughout their lives. The horse's defensive system

is represented by a negative coefficient, preventing the animal from assuming improper postures.

$$D_i^{iter,AGE} = -d_{iter}{}^{iter,AGE} \times \left(\left(\frac{1}{qN} \sum_{k=1}^{qN} Z_k^{(iter-1)} \right) - Z_i^{(iter-1)} \right), AGE = \alpha, \beta, \gamma \quad (3.13)$$

$$d_i{}^{iter,AGE} = d_i{}^{(iter-1),AGE} \times w_d \quad (3.14)$$

where $D_i^{iter,AGE}$ is the ith horse's escape vector from the average of the $Z_k^{(iter-1)}$ vector's worst-case placements. Also included in qN is the total numbers of horses in the worst-case scenario. According to certain estimates, q represents 20% of all horses. w_d is the reduction factor. Horses spend hours foraging for nourishment across the landscape, moving from one meadow to another. While there are exceptions, most horses are kept in

stables.

When a horse needs to graze, it may wander off to a different site unexpectedly. Horses are inherently curious creatures, always seeking new pastures and areas to explore. They can visually perceive each other along the lateral boundaries, satisfying their innate curiosity about their environment. This is simulated as random movements multiplied by an appropriate factor (r). Roaming behavior starts at a young age in horses and gradually diminishes as they mature.

$$F_i^{iter,AGE} = f_{iter}{}^{iter,AGE} \times \mathcal{P}\left(Z_i^{(iter-1)}\right), AGE = \gamma, \delta \quad (3.15)$$

$$f_i{}^{iter,AGE} = f_i{}^{(iter-1),AGE} \times w_f \quad (3.16)$$

The present study considers the arbitrary rate vector of the ith horse for local exploration and outflow from minimums, where $F_i^{iter,AGE}$ represents the arbitrary rate vector of ith horse for local-search and w_f displays the decrease the factor superscript very sequence.

The following equation may be used to write the signal vector of horses at several ages throughout each sequence of the process.

$$S_i^{iter,\alpha} = A_i^{iter,\alpha} + D_i^{iter,\alpha} \quad (3.17)$$

$$S_i^{iter,\beta} = A_i^{iter,\beta} + B_i^{iter,\beta} + C_i^{iter,\beta} + D_i^{iter,\beta} \quad (3.18)$$

$$S_i^{iter,\gamma} = A_i^{iter,\gamma} + B_i^{iter,\gamma} + C_i^{iter,\gamma} + E_i^{iter,\gamma} + D_i^{iter,\gamma} + F_i^{iter,\gamma} \quad (3.19)$$

$$S_i^{iter,\delta} = A_i^{iter,\delta} + E_i^{iter,\delta} + F_i^{iter,\delta} \quad (3.20)$$

The optimal parameters used for the horse herd MPPT are as follows: Grazing, Defence Mechanism, and Hierarchy constants for alpha horses are 1.5, 0.5, and 1.5. For beta horses, the constants are 1.5, 0.9, 0.2, and 0.2 for Grazing, Defence Mechanism, Sociability, and Hierarchy, respectively. Gamma horses have constants of 1.5, 0.5, 0.1, 0.3, 0.1, and 0.05 for Grazing, Hierarchy, Sociability, Imitation, Defence Mechanism, and Wandering & Curiosity. Delta horses have constants of 1.5 and 0.1 for Grazing Wandering & Curiosity. The maximum population is 4, and the iteration is 100.

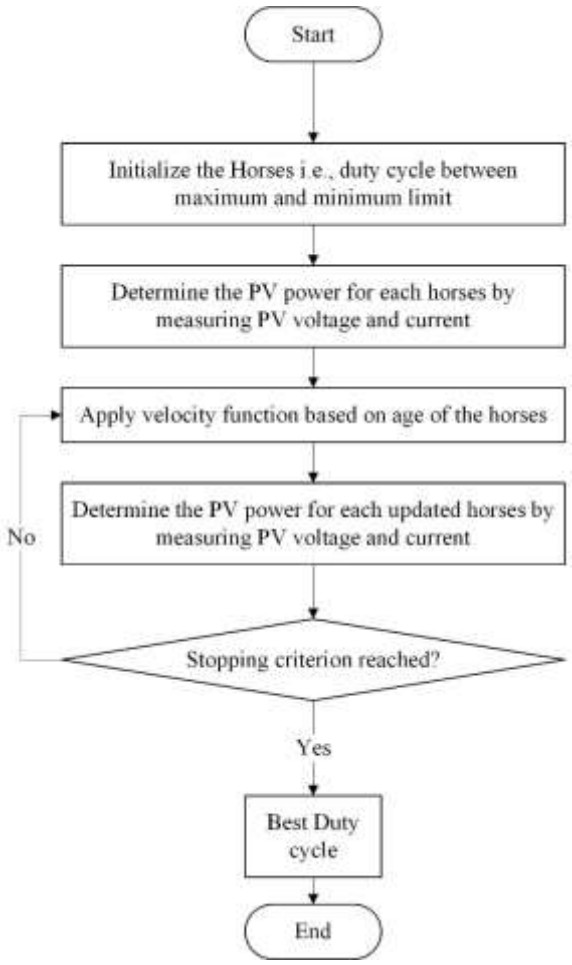

Fig.3.5. Horse Herd MPPT Flowchart

3.4 Horse Herd Optimization MPPT Algorithm

The Maximum power tracking algorithm by Horse herd optimization is explained in this section.

1. Initialize the parameter of the Horse herd optimization
2. Initialize the random Horses (Duty cycle) and find PV power for each horse by measuring PV Voltage and current.
3. Apply the operator of the Horse Herd optimization such as grazing (A), hierarchical (B), social (C), Imitation (E), and defence mechanisms (D) in their behaviour (F) and find a new duty cycle.

4. Again, calculate the PV power and compare it with the previous iteration's maximum power and replace the global duty cycle and global fitness value.
5. Again, go to step 3 up to stopping criterion stratified.
6. Transmit the ultimate optimal/best duty cycle to the (DC-DC) converter to extract the utmost power.

The flowchart of the Horse Herd MPPT is shown in Fig 3.5. The main characteristics of the Horse Herd Optimization MPPT method are its direction and accurate orientation, which differ greatly from the new maximum power point. In other words, this occurs only when the irradiance rises. Because of this, the efficiency of P Horse Herd Optimization MPPTs will decrease. As a solution to these issues, a novel approach utilizing a hybrid fuzzy logic/neural network-based variable step size maximum power-point tracking (MPPT) algorithm has been developed. Due to the limitations of the conventional Horse Herd Optimization MPPT approach, alternative solutions utilizing artificial intelligence techniques have been proposed for PV-MPPT optimization. Chapter 2 provides an explanation of the Hybrid Fuzzy logic/neural network-based variable step size MPPT.

3.5 High Step-Up DC-DC Converter

To achieve the required DC bus voltage for the system, this study employs a high step-up (DC-DC) converter with an active switching LC network, which utilizes the front-end stage of a photovoltaic (PV) system to provide the necessary DC bus voltage. In this transformer-less DC-DC converter, only a single capacitor and a diode are required, yet the voltage gain is significantly increased by combining the ASL (active switched inductor) and ASC (active switched capacitor) networks in a compound configuration. By using a switched capacitor instead of a traditional capacitor, this converter avoids the high instantaneous currents associated with capacitors, which is a drawback of traditional voltage-

boosting devices. Figure 3.6 illustrates the topology of the active switching LC network in the high step-up (DC-DC) converter with active switching. The ASLC converter topology combines an ASC system network with the original ASL system network. There is a common switch, S1, between the original ASL and ASC networks, which includes inductors L1 and L2 as well as switches Q1 and Q2. Because only a single diode and a single capacitor are added to this, the basic structure is maintained.

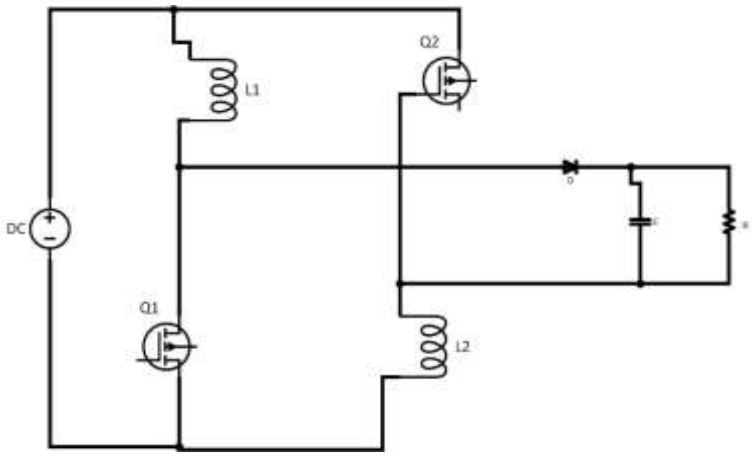

Figure 3.6. High step-up ratio DC-DC converter and an active switching LC network

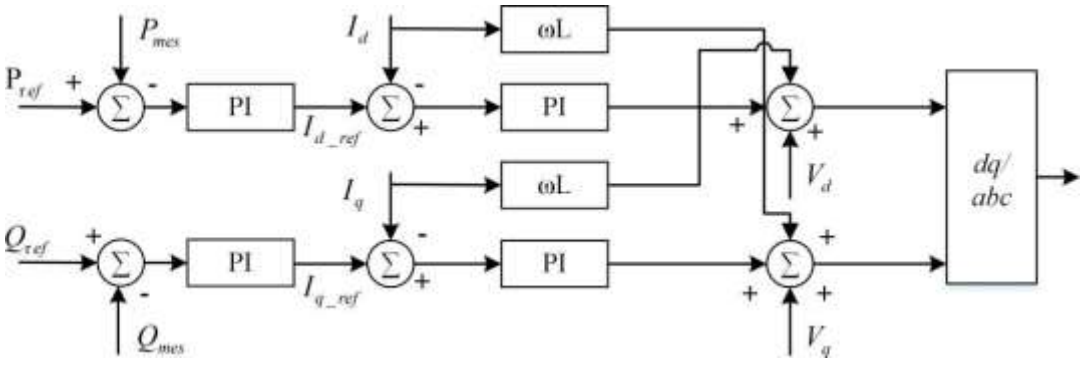

Figure 3.7. Inverter conventional current controller

3.6 Inverter and Controller Design

VSIs and CSIs are both typical inverter types found in utility hybrid grids, each with distinct pros and cons. The mode of operation influences the selection of the control strategy to be used. For example, droop control is the most common method of controlling a ship in an isolated situation, allowing voltage and frequency adjustments depending on load changes. The hybrid grid must supply power following the central controller's commands or the hybrid grid's ability to do so, depending on the grid's voltage and frequency. As a result, power regulation of the grid-connected inverter is a key consideration. Aside from that, regulating the grid's injected current is critical to maintaining high power quality and safeguarding the system. The VSI inverters chosen to meet these needs are currently controlled. Figure 3.7 shows the conventional grid-connected inverter control system, which controls the DC-link voltage and the inner AC control loop. The PI controller controls both the reactive and active power flow in the outer loop. An internal reference point is provided by the error signal in the inner current control loop. Typically, the frequency (f) of the outer loop is set low to reduce sensitivity to changes in the inner current controller. The control bandwidth of the outer loop is between 10 and 20 Hz, resulting in slower movement compared to the inner loop. An essential aspect of AC control is feed-forward voltage regulation. The control system regulates the currents along the d- and q-axes of the inverter. The loop frequency is around 100 Hz, approximately ten times faster than the outer loop. The reference point and component along the d-axis are set based on a load's reactive power requirements. The voltage components along the d- and q-axes are converted into appropriate three-phase voltage for current tracking. Subsequently, the three-phase voltage generates the gating signal for the inverter. To maintain a constant grid frequency, a phase-locked loop (PLL) is necessary. Calibration of the PI controller parameters, specifically the integral gain and proportional gain, is carried out through experimentation and refinement.

3.7 LCL Filter

Power electronics devices have been utilized in recent years for applications in solar and wind power systems, contributing to the growth of renewable energy sources. Optimizing power transmission from the PV system to the utility grid necessitates the use of power converters. However, the use of power conversion equipment can lead to harmonic issues that may adversely affect connected loads and sensitive electronics. Therefore, Total Harmonic Distortion (THD) is a critical consideration in the system.

An LCL filter is commonly employed to mitigate the harmonic waves generated by the inverter. Traditionally, the inductance of the input or output circuits of power conversion devices has been utilized to reduce these harmonics. Placing an LCL filter between the grid and the inverter helps attenuate the switching frequency harmonics produced by the grid-connected inverter. Compared to an L filter, an LCL filter offers better attenuation capabilities and cost savings for high-order harmonics. Its ability to attenuate higher harmonics allows for the use of lower switching frequencies to comply with harmonic restrictions outlined in established standards such as IEEE-519 and IEEE-1547.When designing an LCL filter, several factors need to be taken into account, including but not limited to current ripple, filter dimensions, and attenuation of switching ripple. The presence of reactive power demand has the potential to induce resonance in the capacitor when it interacts with the grid. Several factors, including output phase voltage, rated power, line voltage, grid frequency, and switching frequency, DC voltage must be taken into account while designing an LCL filter. grid-connected solar power systems.

The following are the LCL filter's design parameters: base resistance,

$$Z_b = \frac{V_{LL}^2}{P} \tag{3.21}$$

Base capacitance,

$$C_b = \frac{1}{\omega_g Z_b} \tag{3.22}$$

The maximum permitted power factor change for the grid is 5%, which forms the basis of the filter capacity design. The filter's capacitance may be calculated in this way:

$$C_i = 0.05 \times C_b \tag{3.23}$$

The goal is to ascertain the inverter side inductance filter design such that the current flowing through the output ripple is limited to no more than 10% of the nominal amplitude. The calculation of inductance can be determined by a specific formula or equation.

$$L_i = \frac{V_{DC}}{6 f_{sw} \Delta I_{Lmax}} \tag{3.24}$$

where $\Delta ILmax$is the 10 % current ripple denoted by:

$$\Delta I_{Lmax} = 0.01 \frac{P\sqrt{2}}{V_{LL}} \tag{3.25}$$

The inductance component serves to restrict the output current ripple to a maximum of 10% of its standard amplitude. The calculation of grid-side inductance is performed as follows.

$$L_g = \frac{\sqrt{\frac{1}{k_a^2}+1}}{C_i \omega_{sw}^2} \tag{3.26}$$

The designed filter value for the LCL filter: L1 and L2 are 0.03H and C is 100µF.

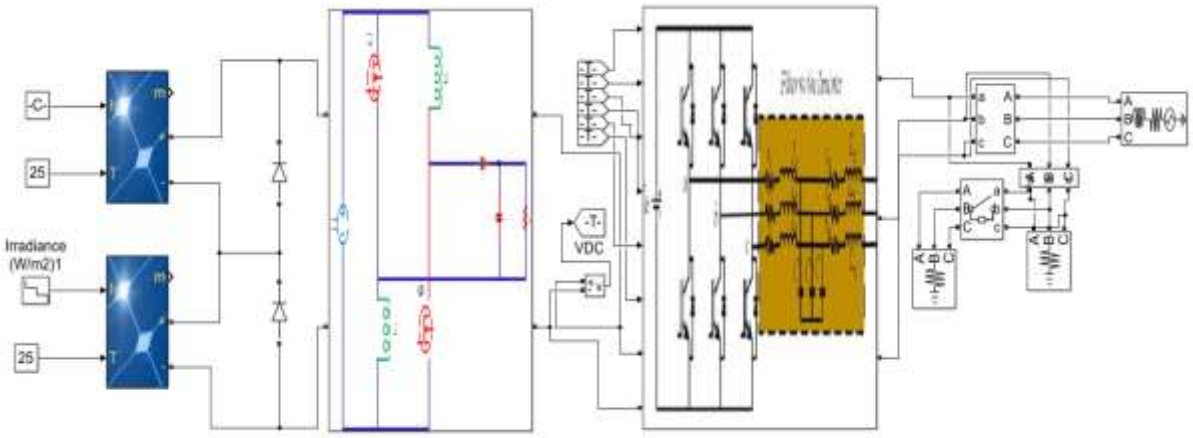

Fig.3.8. MATLAB Simulink of Grid-connected PV system with partial shading with horse herd MPPT.

3.8 MATLAB Simulation Results of Grid-connected PV-system with Horse Herd Optimization

The developed grid-connected PV system with horse herd MPPT control for partial shading scenarios was simulated using MATLAB and the developed Simulink model, as shown in Fig 3.8. The irradiance for the first group of the PV array was maintained at 1000 W/m², while the irradiance for the second group varied every 1 second to create partial shading effects. Specifically, the irradiance changed from 1000 W/m² from 0 to 1 second, 800 W/m² from 1 to 2 seconds, and 600 W/m² from 2 to 3 seconds. Fig. 3.9 presents the simulation results for the PV system, including PV voltage, PV current (I), PV power, and DC link voltage. During the 0 to 1-second interval, the PV array power was 2049 W, with the PV voltage maintained at 250 V and the PV current at 8.19 A. In the next second (1 to 2 seconds), the PV power was reduced to 1540 W, with the PV voltage dropping to 220 V and the PV current decreasing to 7 A. Finally, from 2 to 3 seconds, the PV power further decreased to 1000 W, with the PV voltage at 198 V and the PV current at 5.05 A. The PV voltage response varied based on different partial shading conditions, as observed in Fig. 3.9,

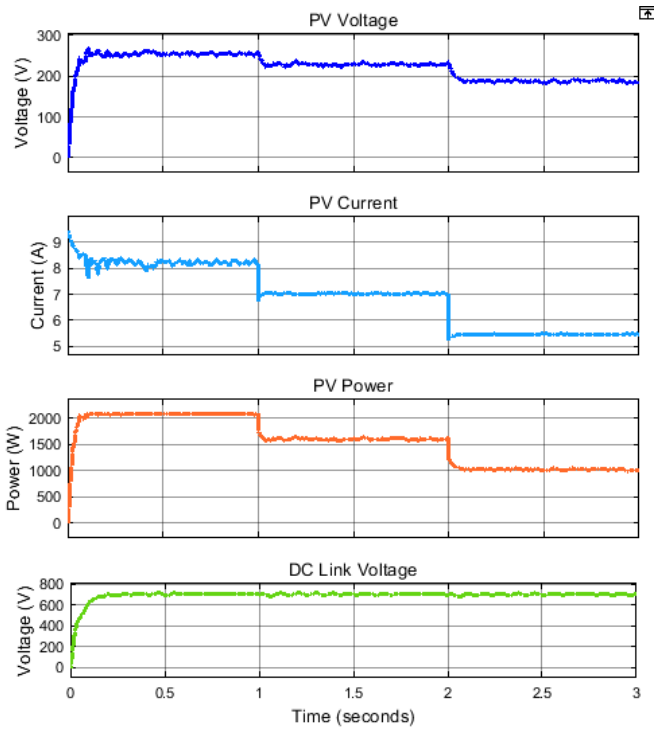

Fig.3.9. Simulation result of PV voltage, current, power and DC link voltage with optimal HOA parameter.

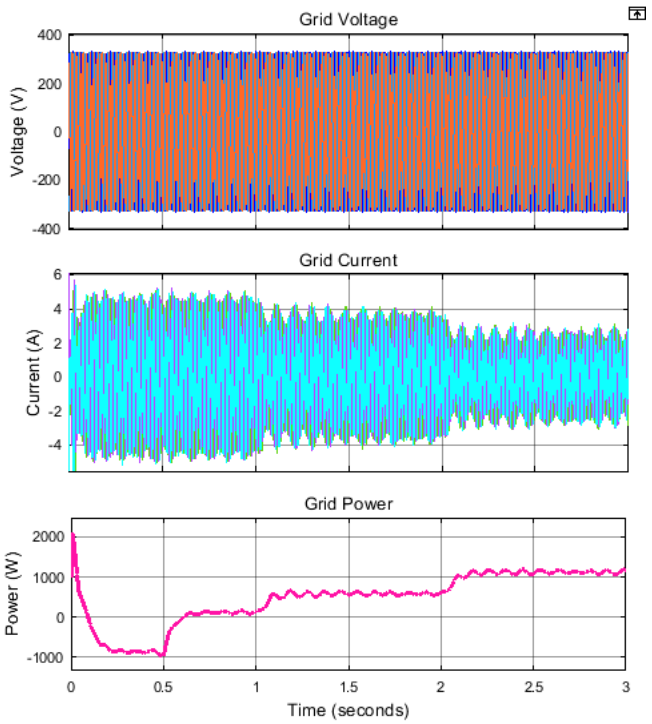

Fig.3.10. Simulation result of grid voltage(V), current(I) and power(P)

demonstrating the effective extraction of maximum power from the PV array using the horse herd optimization MPPT algorithm.

The simulation result of the grid such as grid voltage, grid current and grid-power is demonstrated in Fig 3.10. The grid voltage is maintained at 400 V. The grid current and power are changing based on power output from the PV array as seen in Fig 3.10. The grid receives power around 950 W from 0 to 0.5 sec because PV has more excess power than load. The grid supplies power to load during 0.5 to 3 sec due to PV power being less than load power.

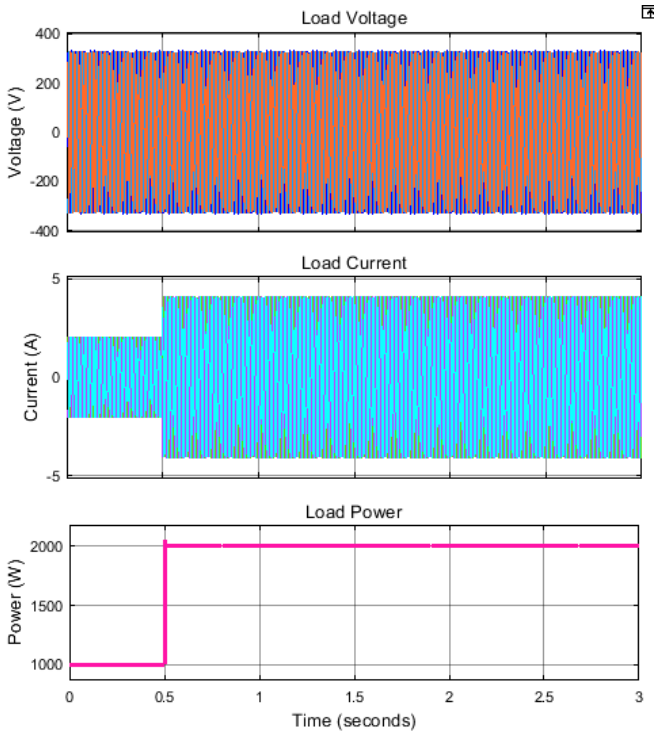

Fig.3.11. Simulation result of grid voltage, current and power.

Figure 3.11 depicts the simulation outcomes of load parameters, specifically load voltage, load current, and load power. The load voltage was consistently maintained at 400 V, the load-current changing based on the load added into the system. The load power is 1000 W from 0 to 0.5 sec and 2000 W from 0.5 to 3 sec. From the test results (Fig 3.9 to Fig 3.11), the Power balance

maintained between sources and load and maximum(peak) power from PV is extracted/obtained effectively using horse herd optimization.

The same system was tested with the following random parameters of the horse herd i.e., Grazing, Defence Mechanism, and Hierarchy constant for alpha horses is 1, 0.2, and 1. Grazing, Defence Mechanism, sociability, Hierarchy constant for beta horses is 1, 0.5, 0.1 and 0.1. Grazing, Hierarchy, sociability, imitation, Defence Mechanism and Wandering & Curiosity constants for gamma horses are 1, 0.2, 0.2, 0.1, 0.2 and 0.1. Grazing and Wandering & Curiosity constant for delta horses are 1 and 0.2. the maximum population is 4 and the iteration is 100. Figure 3.12 Provide the results of the PV system with random HOA parameters and the results are similar to the optimal parameter of the HOA.

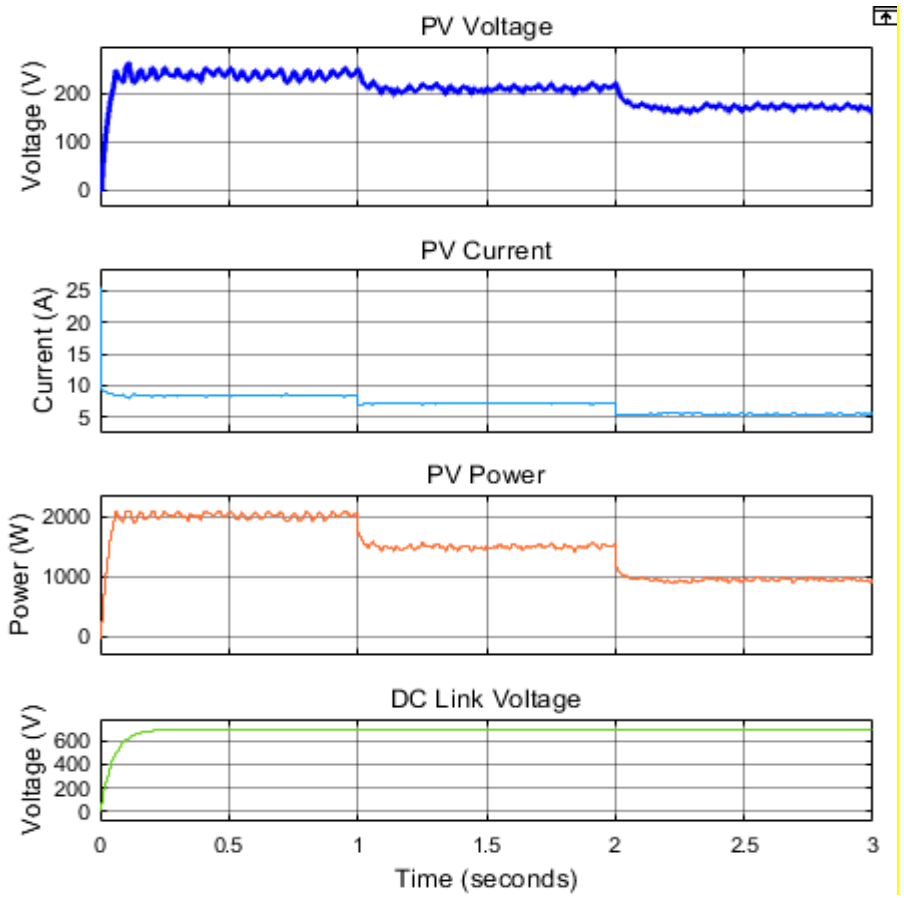

Fig.3.12. Simulation result of PV voltage, current, power and DC link voltage with random HOA parameter.

3.9 Simulation Results of Grid-connected PV system with Hybrid Fuzzy logic/neural network (NN)-based variable step size MPPT

A Simulink diagram of a Hybrid Fuzzy logic/neural-network (NN)-based variable step-size MPPT-controlled PV system connected to a three-phase network is depicted in Figure 3.13. The system includes a DC-DC converter and a three-phase full-bridge inverter to link the solar panels to the grid for power generation. The control algorithm comprises an MPPT controller and a phase-locked loop (PLL), with all controllers integrated, including the inverter DC bus controller, boost converter, the inverter, and the MPPT controller.

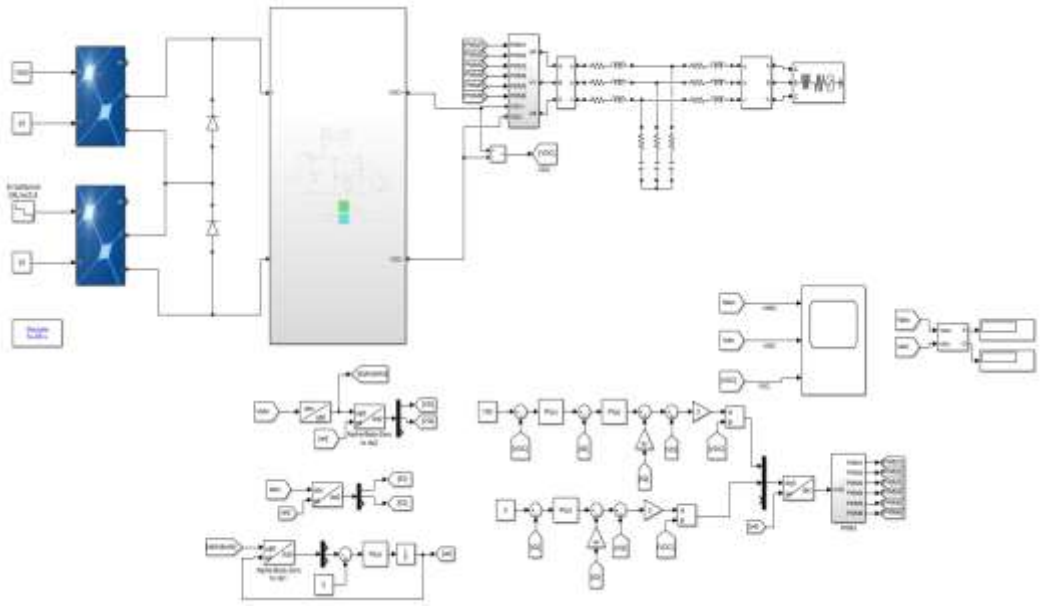

Figure 3.13. Simulink model of the solar PV three-phase grid system with Hybrid Fuzzy logic/neural network-based variable step size MPPT

The grid controls the output terminal current of the grid-linked inverter as well as the DC link voltage. The duty cycle generated by the hybrid (fuzzy logic and neural network) MPPT algorithm is then followed by the controller of the high gain boost converter. DC energy is converted to AC energy by an inverter that

also manages synchronized current output with the DC-link voltage and grid voltage. The controller includes a voltage-regulating outer loop and a current-controlling inner loop. The inverter plays a crucial role in maintaining a constant DC-link voltage and keeping the output current synchronized with the grid voltage. The power rating of the two series-connected PV panels is 2100 W and 258 V, while the grid rating is 400 V and 50 Hz.

(i) Under uniform irradiance

The PV panel is connected in series, and the irradiance is fixed at 1000 watts per square meter (W/m2). The corresponding PV power, grid voltage, grid current, DC link voltage, and grid power are shown in Figure 3.14. The simulated results indicate that the PV power is around 2080 W, and the grid power is around 1990 W. It has also been noted that the voltage across the DC connection is maintained at 700 V, with the grid voltage at 400 V and the grid current at 4.975 A.

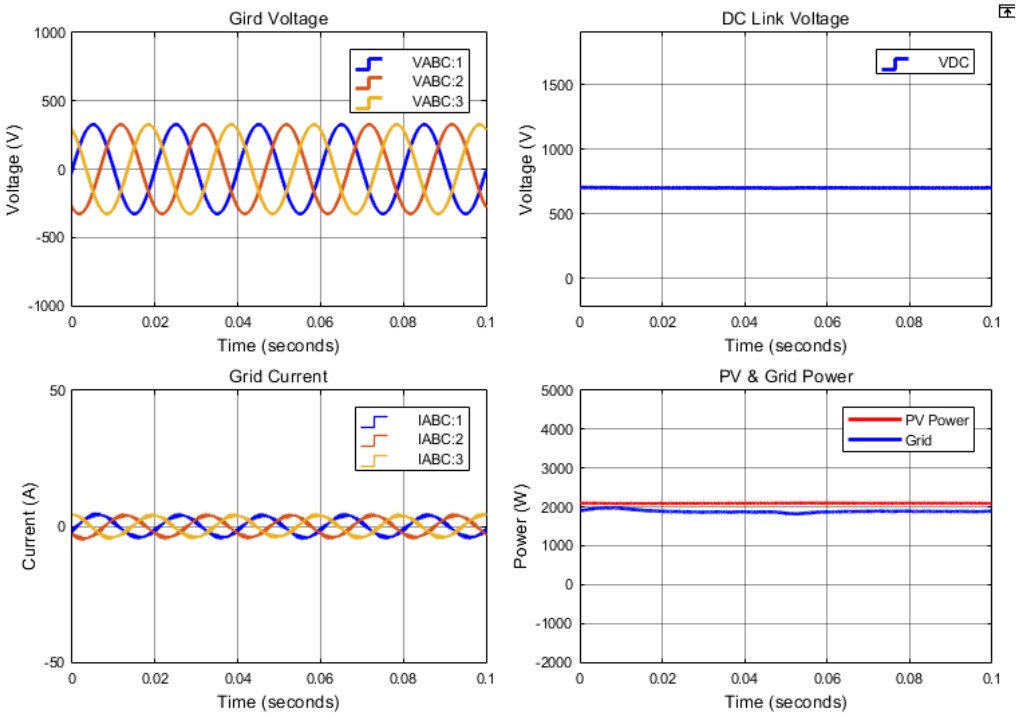

Figure 3.14. Simulation results at 1000 W/m^2

The efficiency is calculated for the present operating condition and found to be 95.67%. Similarly, in the second condition, the irradiance is fixed at 500 W/m2, and results such as PV power, grid voltage, grid current, DC-link voltage, and electrical grid power are simulated.

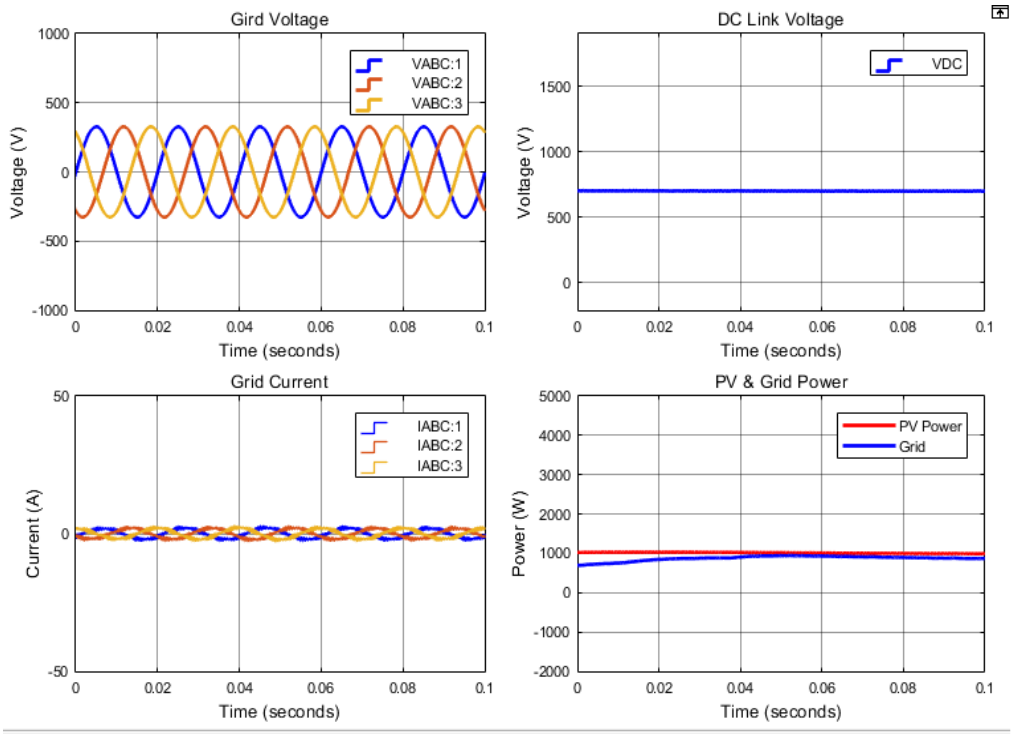

Figure 3.15. Simulation results at 500 W/m^2

The simulated outputs are demonstrated in Figure 3.15. The results report that the PV power and grid power are 1010 W and 990 W, respectively. The DC-link voltage is 700V, along with the electrical grid voltage and current at 400 V and 2.52 A. Therefore, the efficiency of the system at 500 W/m2 is 98.02%.

(ii) Under Partial Shaded Conditions

The first PV panel's irradiance is fixed at 1000 W/m2, whereas the irradiance on the second PV panel is changed from 1000, 800, 600, and 400 W/m2 every 0.2 seconds to create a partial shading effect. The corresponding results such as PV power, grid voltage, grid current, DC-link voltage, and grid power are shown in

Figure 3.16. When the second PV panel's irradiance is 800 W/m2, the PV power is around 1700 W, the grid power is around 1600 W, the voltage of the DC connection is maintained at 700V, the grid voltage is 400 V, and the grid current is 4 A. The efficiency in this condition is 94.11%. When the second PV panel's irradiance is 600 W/m2, the PV power is around 1400 W, the grid power is around 1300 W, the DC link voltage is maintained at 700 V, the grid voltage is 400 V, and the grid current is 3.125 A, the efficiency in this condition is 92.85%.

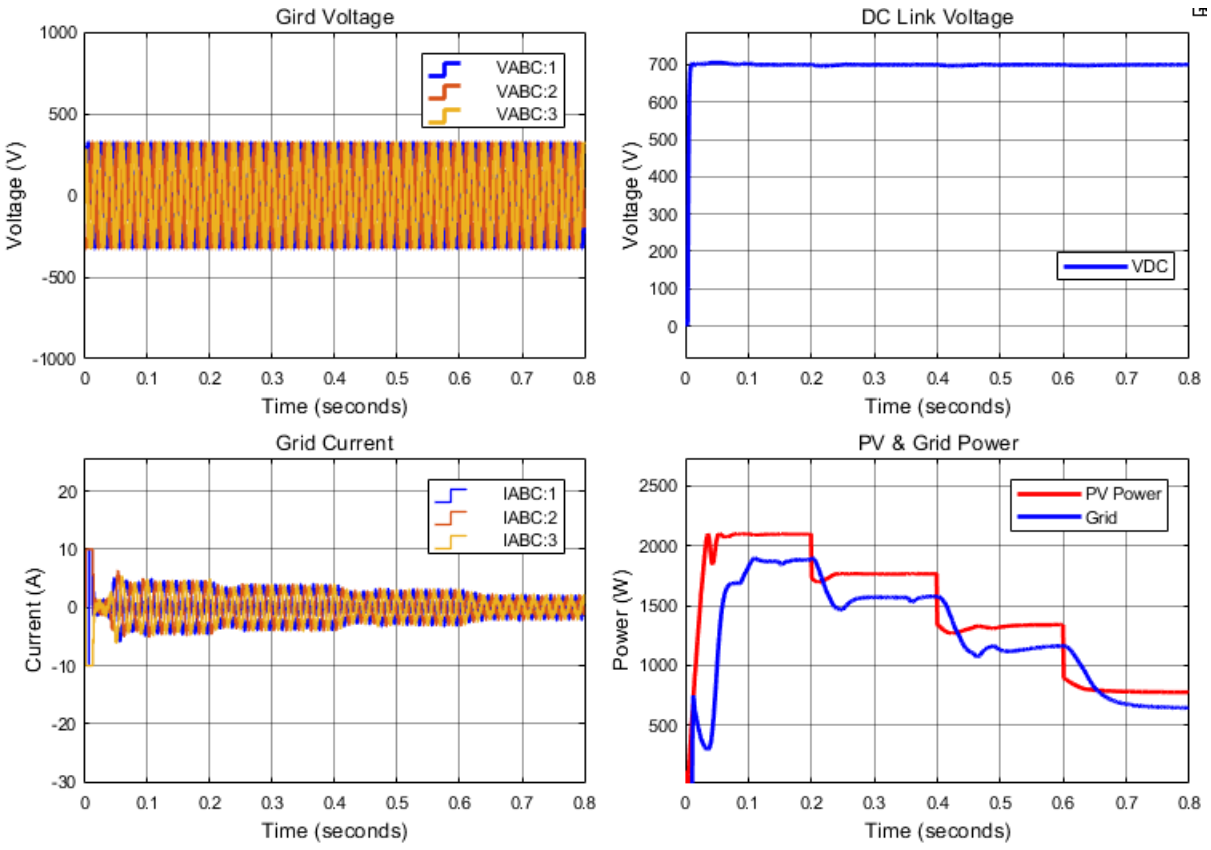

Figure 3.16. Simulation results under the partial shading effect

When the second PV panel's irradiance is 400 W/m2, the PV power is around 850 W, the grid power is around 780 W, the DC link voltage is constantly maintained at 700 V, the grid voltage is 400 V, and the grid current is 1.95A. The efficiency in this condition is 91.76%. The maximum power from the PV panel is effectively extracted to the peak point employing hybrid fuzzy logic/neural network-based variable step-size MPPT. Tables 3.2 and 3.3

demonstrate the output parameters and efficiency of the proposed MPPT under different operating conditions and with other MPPT algorithms.

Table 3.2 presents the outcomes of the proposed Maximum Power Point Tracking (MPPT) algorithm under various operating conditions. The table includes parameters such as PV power, grid power, grid current, and efficiency (%) for different irradiance levels on Panel 1 and Panel 2.

Table 3.2. The outcome of the proposed MPPT under different operating parameters

Operating Conditions	Parameters			Efficiency (η) (%)
	PV Power (W)	Grid Power (W)	Grid current (A)	
Irradiance of Panel 1 and Panel 2: 1000 W/m^2	2080	1990	4.975	95.67
Irradiance of Panel 1 and Panel 2: 500 W/m^2	1010	990	2.4750	98.02
Irradiance of Panel-1: 1000 W/m^2 and Panel 2: 800 W/m^2	1700	1600	4	94.11
Irradiance of Panel-1: 1000 W/m^2 and Panel 2: 600 W/m^2	1400	1300	3.25	92.85
Irradiance of Panel-1: 1000 W/m^2 and Panel 2: 400 W/m^2	850	780	1.95	91.76

At an irradiance of 1000 W/m2 on both panels, the PV power ranges from 850 W to 2080 W, with corresponding grid power values and grid currents. As the irradiance decreases to 500 W/m2 on both panels, the PV power and grid power reduce accordingly, while the grid current remains relatively stable. Similar trends are observed when Panel 1 has higher irradiance than Panel 2, indicating the algorithm's ability to adjust MPPT settings based on varying irradiance levels to maximize efficiency, as reflected in the efficiency values ranging from

91.76% to 98.02%. Table 3.3 provides a comparative analysis of the proposed hybrid Maximum Power Point Tracking (MPPT) technique with various other MPPT techniques from different references. The table includes references, MPPT techniques, parameters such as PV power, grid power, and grid current, along with efficiency (%) values

Table 3.3. Comparisons of proposed hybrid MPPT with other MPPTs

References	MPPT Technique	Parameters			Efficiency (η) (%)
		PV Power (W)	Grid Power (W)	Grid current (A)	
[15]	Fuzzy	2076	1978.4	4.94	95.3
[18]	Neural Network	2075	1975.4	4.93	95.2
[33]	Fuzzy	2070	1958.2	4.89	94.6
[34]	Fuzzy	2072	1966.3	4.91	94.9
[35]	Fuzzy	2071	1963.3	4.90	94.8
[36]	Fuzzy, Neural with evolutionary algorithms	2073	1971.4	4.92	95.1
[37]	Neural Network Estimator	2074	1968.2	4.92	94.9
[38]	fuzzy	2073	1965.2	4.91	94.8
[39]	SASV-MPPT approach and Lyapunov design method	2077	1981.4	4.98	95.39
Horse Herd MPPT	Horse Herd MPPT	2078	1983.45	4.95	95.45
Hybrid Fuzzy Neural Network	Hybrid Fuzzy Neural Network	2080	1990	4.975	95.67

Different MPPT techniques such as Fuzzy, Neural Networks, Hybrid Fuzzy Neural Networks, and others are evaluated based on their performance metrics. The efficiency values range from 94.6% to 95.67%, indicating the effectiveness of the hybrid approach in maximizing power generation from the photovoltaic (PV) system. The table also includes a unique "Horse Herd MPPT" technique, showcasing the diversity of methods explored in MPPT optimization for solar PV systems.

3.10. Experimental Verification

Figure 3.17 illustrates the hardware setup for the hybrid fuzzy logic/neural network-based variable step-size MPPT for a grid-linked photovoltaic system. The experimental setup consists of eight panels rated at 250 W each installed on the rooftop, a high step-up boost converter, a DC-AC inverter, a single-phase AC grid, and a PIC microcontroller for implementing MPPT and grid inverter control.

Figure.3.17. The hardware setup of the Proposed Work.

The hardware model is tested with uniform irradiance and partially shaded conditions. Figure 3.18 shows the PV voltage and current for constant irradiance. PV voltage is 255 V and PV current is 7.58 A and PV power is 1932.9 W. Figure 3.19 shows the DC link voltage, grid phase ‘a’ voltage and current for the same conditions. The DC link voltage is maintained at 698 volts, phase ‘a’ voltage is sustained at 228 V and phase ‘a’ current is maintained at 2.56 A and power from Inverter is 1766.4 W. The efficiency of the system is 91.38 %.

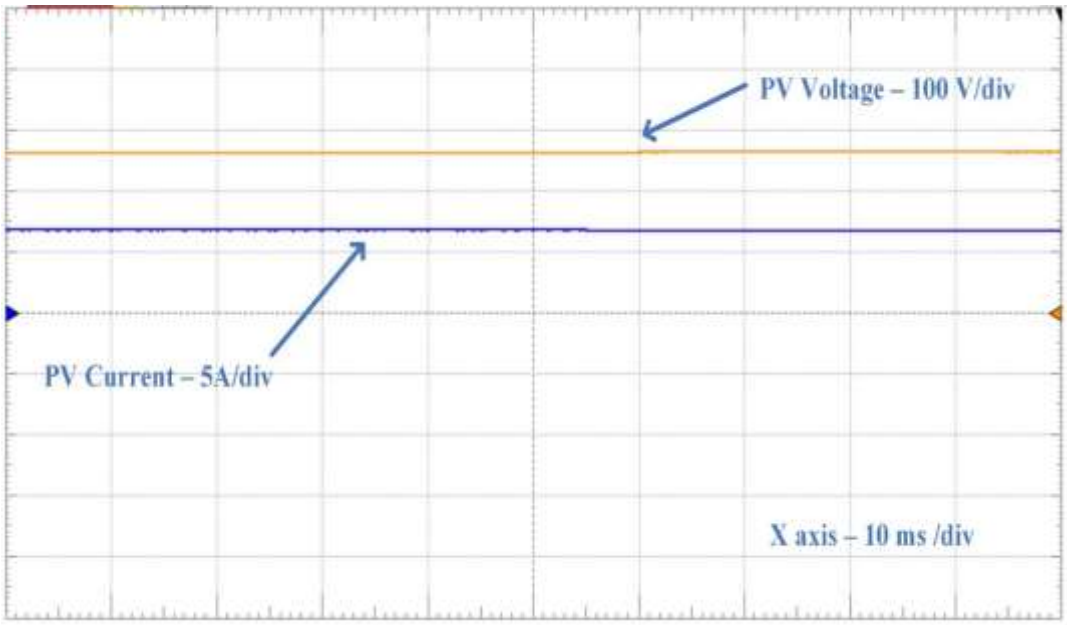

Figure.3.18. PV Voltage and current for constant Irradiance.

Partial shading conditions are created for the four panels by covering each panel with metal sheets, and corresponding results are measured during these conditions. Figure 3.20 shows the PV voltage and current for partially shaded conditions. The PV voltage, current, and power after partial shading is 210 V, 3.89 A, and 816.9 W, respectively.

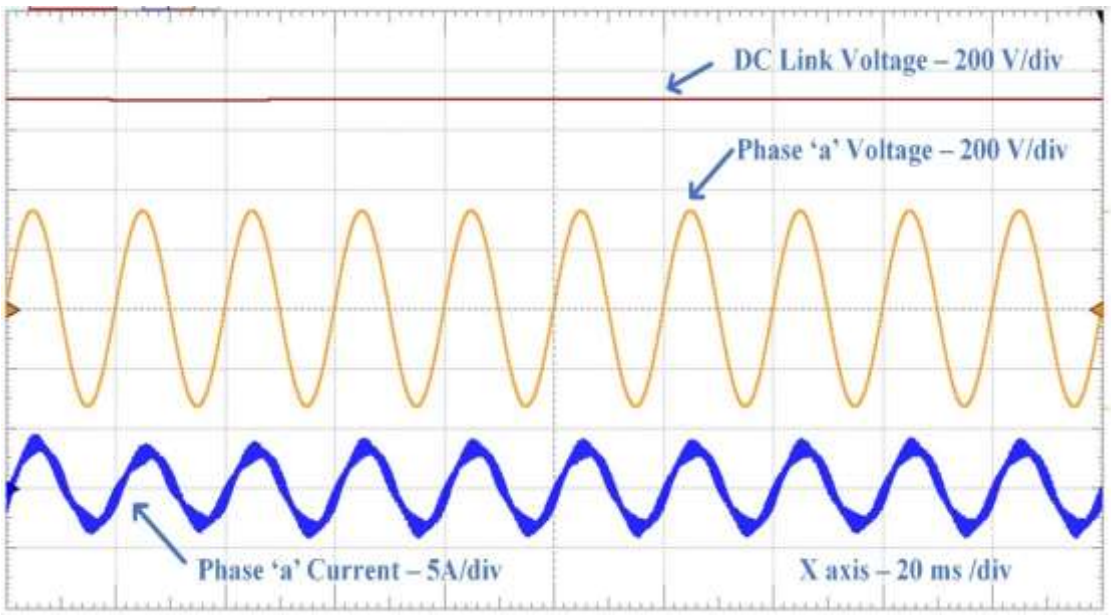

Figure.3.19. DC link Voltage, grid Phase 'a' voltage and current for constant Irradiance.

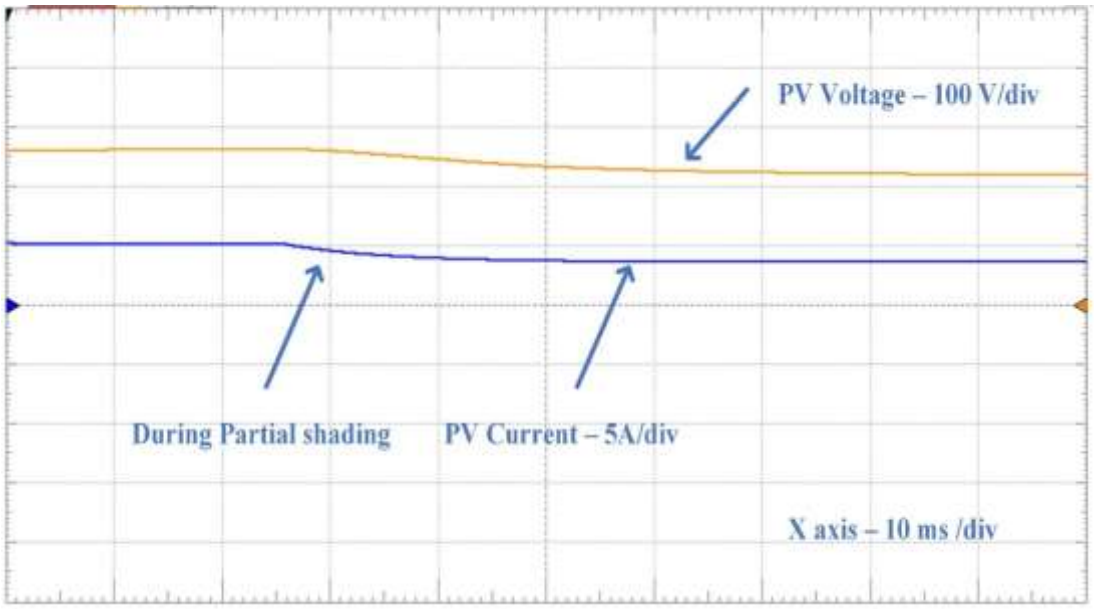

Figure 3.20. PV Voltage and current for partially shaded conditions.

Figure 3.21 shows the DC link voltage, phase 'a voltage, and current for the same conditions. The DC link voltage, phase 'a' voltage, current, and power from the inverter after partial shading are 697 V, 230 V, 1.1 A, and 759 W. The efficiency of the system is 92.91%.

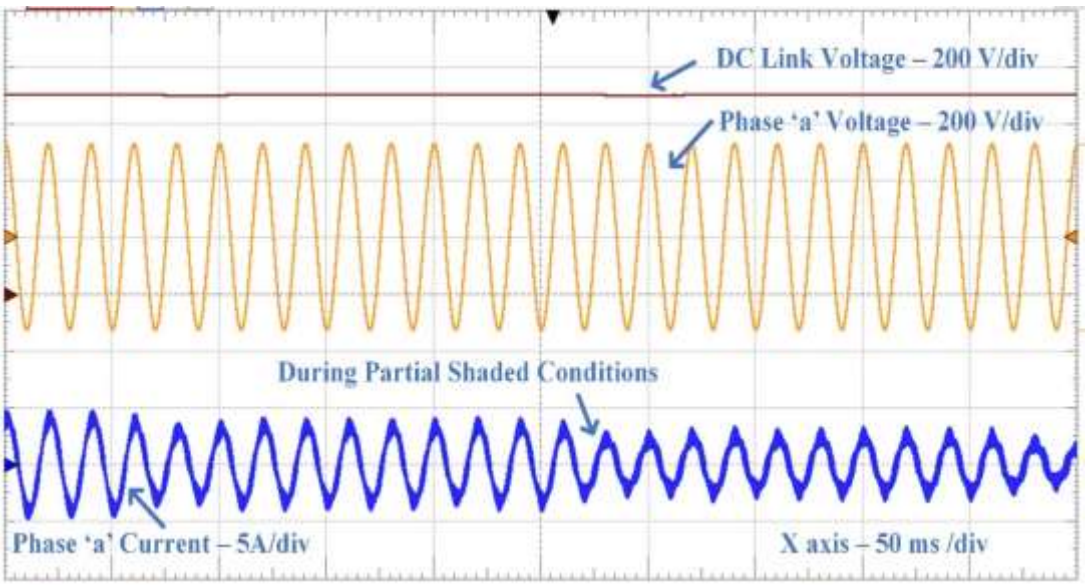

Figure.3.21. DC link Voltage, grid Phase 'a' voltage and current for partially shaded conditions.

3.11 Summary

This chapter describes how a grid-linked PV system with a hybrid fuzzy neural network variable step-size MPPT and horse herd optimization-based MPPT operates. Both partial shade and uniform irradiance conditions were investigated for the model's simulation findings. According to test findings, hybrid fuzzy neural network variable step-size MPPT outperforms other MPPTs in terms of accuracy and quality. Lastly, measurements and analyses are done on the hybrid fuzzy neural network variable step-size MPPT experimental findings.

Chapter 4

Artificial Ecosystem Optimization algorithm tuned PI-controlled Grid-connected PV system

4.1 Introduction

This research demonstrates the crucial role of optimization approaches in designing the most efficient PI controller for power converters in Grid-connected PV systems. In this study, the PI controller parameters are optimized using the best optimization method. The power quality and stability of a three-phase grid-linked PV inverter scheme are enhanced through real-time Kp and Ki data. To implement the proposed controller method, a PI controller and synchronous reference frame are utilized. High dynamic responsiveness is achieved by incorporating feed-forward compensation within the current control loop. Artificial Ecosystem Optimization offers advantages over traditional PI and Augmented full state feedback controllers in terms of calculation time, robustness, and process information. However, not all effects of optimizing a PV inverter linked to the grid were covered, including those related to DC link voltage fluctuations, power quality performance, output voltage and current stability, harmonics reduction, smooth power flow, and frequency stabilization. This cutting-edge research focuses on enhancing the power quality of the inverter system, expertly minimizing temporal transient response and overshooting while simultaneously achieving zero steady-state error. Our innovative approach effectively addresses challenges posed by load variation and DC link stability, enabling rapid improvements in voltage and frequency stability with reduced complexity using the Artificial Ecosystem Optimization approach to optimize PI control settings. The development of inverter control for a 2.1 kW solar PV system is conducted in MATLAB/Simulink, with the Artificial Ecosystem Optimization technique implemented using a MATLAB m-file script. THD variation is minimized in both simulated and real-world experiments when

comparing PI and Augmented full state feedback controller performances with and without an optimization method [50]-[55] here are some of the most important aspects and contributions of the planned research:

i. To enhance power quality and stability on a three-phase grid, this study proposes using a controller-based Artificial Ecosystem Optimization to optimize Kp and Ki in PV converter systems in real time.
ii. The purpose of this method is to minimize the steady-state error caused by power-load variations while simultaneously optimizing the PI controllers' settings to reduce transient response and temporal overshoot.
iii. With the help of an optimized controller, PV converter systems can employ a better controller in real-time, which, in turn, determines the best possible PI controller settings in response to changing loads.

4.2. Grid-Linked PV Inverter System

In this research, the link between the solar photovoltaic (PV) array and the utility grid was established using a three-phase voltage source inverter (VSI). The hybrid fuzzy neural network variable step size MPPT regulators, DC link, a high-voltage gain boost converter, inverter, and filter are all included in the device's circuitry, which is shown in Figure 4.1. A hybrid fuzzy neural network with variable step size maximum power point tracking technique is combined with a high voltage gain boost converter to maximize the power produced by the PV system. To facilitate distribution, a three-phase AC grid is connected to a three-phase voltage source inverter, a low-pass (LCL) filter,

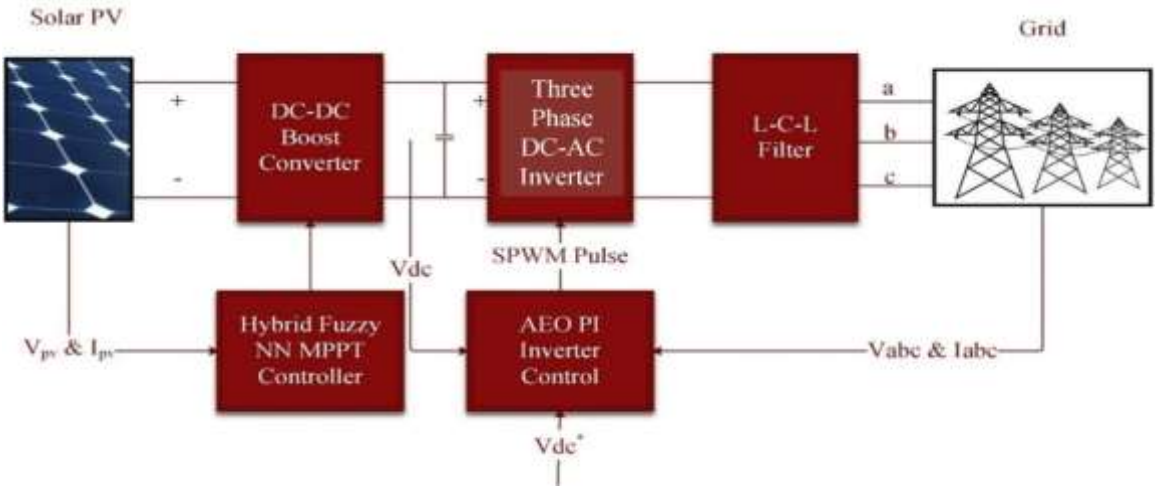

Figure 4.1. Three-phase Grid linked PV system

and its control. Extensive details on solar PV-integrated three-phase grids are provided in the next section [67]-[70].

4.3 PV system model

The solar cell is the fundamental building block of any photovoltaic system. It harnesses the power of multiple solar cells working in unison within a PV cell. The PV cell's analogous circuit, depicted in Figure 4.2, comprises a parallel diode (D), a photocurrent source (I_{ph}), a shunt resistance (R_{sh}), and a series resistance (Rs) interconnected in series with the source. This circuit allows for the discovery of the fascinating relationship between output current and output voltage, as demonstrated in Eq (4.1).

$$.I_{pv} = I_{ph} - I_{sh}\left(e^{\left(\frac{V_{pv}+I_{pv}R_S}{AN_SkT}\right)} - 1\right) - \frac{V_{pv}+I_{pv}R_S}{R_{sh}} \qquad (4.1)$$

Where the saturation current is represented by Ish, photocurrent is represented by Iph, Boltzmann's constant is symbolized by k with a value of 1.3811 × 10^-23, the electron charge is represented by q with a value of 1.6021 × 10^-19 C, the ideal diode factor is denoted by “A”, the series connected PV cell is denoted

by Ns, and the cell temperature at standard conditions is denoted by “T”. The photocurrent of a PV cell can be calculated at any temperature and solar irradiance using Eqs. (4.2), (4.3), and (4.4).

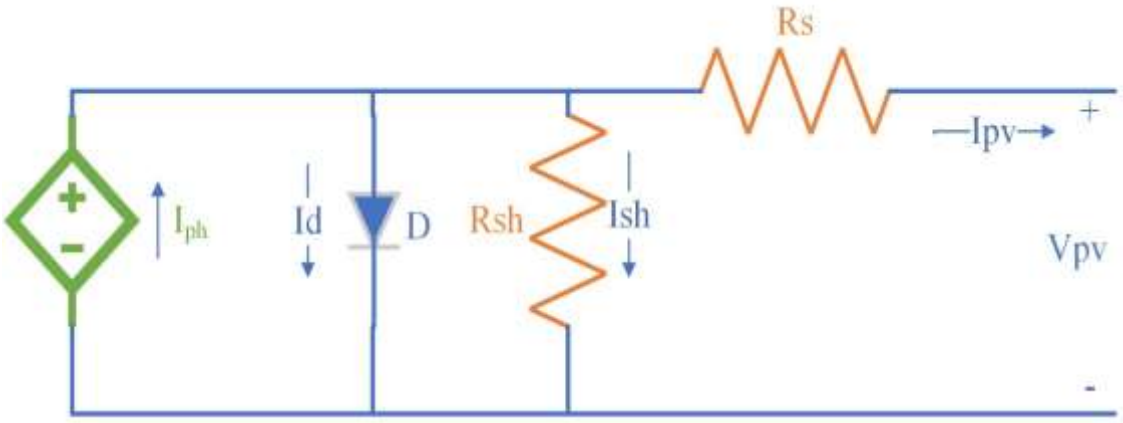

Figure 4.2. Equivalent circuit of Solar PV cell

Table 4.1. PV panel specifications

S. No.	Description	Values	Unit
1	Open-circuit voltage	44.86	V
2	Short-circuit current	5.5	A
3	Peak-power point voltage	37.73	V
4	Peak-power point current	5.04	A
5	Coefficient of Voltage/temperature	-0.364	%/°C
6	coefficient of current/temperature	0.102	%/°C
7	Panel in Series	11	
8	Strings in parallel	1	
9	Peak power at STC	2092	W

$$I_{ph} = \frac{G}{G_{ref}}\left(I_{sc} + K_i\left(T - T_{ref}\right)\right) \tag{4.2}$$

$$I_{sc} = I_{sc,ref}\left(\frac{R_P + R_S}{R_P}\right) \tag{4.3}$$

$$I_{sat} = \frac{I_{sc,ref} + K_i(T - T_{ref})}{exp^{q\left(V_{oc,ref} + \frac{K_v(T - T_{ref})}{AN_S kT}\right)} - 1} \quad (4.4)$$

Where G_{ref} and G represent the current and reference solar irradiance, the temperature coefficient at short-circuit current is denoted by K_i; T_{rk} represents the absolute temperature of the module in Kelvin, and the open-circuit voltage temperature coefficient is denoted by K_v. Furthermore, $V_{oc,\,ref}$, and I_{SC}, ref denote the open-circuit voltage and short-circuit current of the PV panel at standard test conditions [87

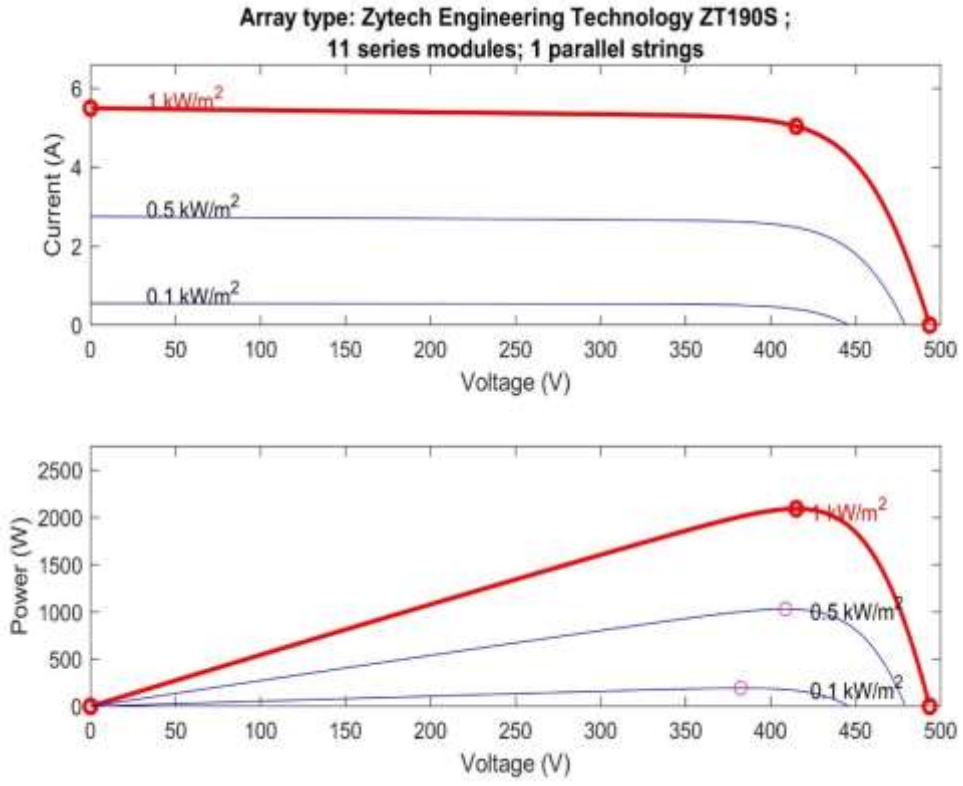

Figure 4.3. PV and IV Characteristics of the PV panel

]. Table 4.1 presents the specifications of the PV unit based on Eqs (4.1)–(4.4). Under typical test conditions, the Simulink model confirms the I–V and P–V characteristic curves (G_{ref} = 1000 W/m2 and T_{rk} = 25°C), as shown in Fig. 4.3.

4.4 Peak power tracking algorithm and DC-DC boost converter

The photovoltaic array uses 11 series modules and 1 parallel string to achieve a maximum power output of 2.1 kW. Figure 4.3 displays the PV system array's characteristic curves for various temperatures and irradiance levels. The voltage and current produced by PV arrays fluctuate significantly due to changes in temperature and irradiance, impacting these parameters. In this setup, a high voltage gain DC-DC boost converter is used in conjunction with the Hybrid Fuzzy Neural Network variable step size MPPT approach to monitor PV output based on irradiance and temperature. The maximum PV output can be regulated using the Hybrid Fuzzy Neural Network variable step size MPPT by sensing PV current (I_{pv}) and PV voltage (V_{pv}). Increasing the DC voltage (V_{dc}) to 400 volts allows adjusting the duty cycle D of the high voltage gain boost converter to raise the PV voltage and extract power at its peak. PV solar systems connected to the power grid typically use a DC connection. The DC side voltage of the grid inverter should be regulated near its peak PV voltage, with no fluctuations in the inverter's output current. The nominal voltage of the inverter should match that of the DC connection, ensuring the inverter's current and voltage are well-matched with those of the array. An equivalent mathematical expression for a high-voltage-gain DC-DC step-up converter can be written as follows: (4.5).

$$V_{dclink} = \frac{V_{pv}}{1-D} \tag{4.5}$$

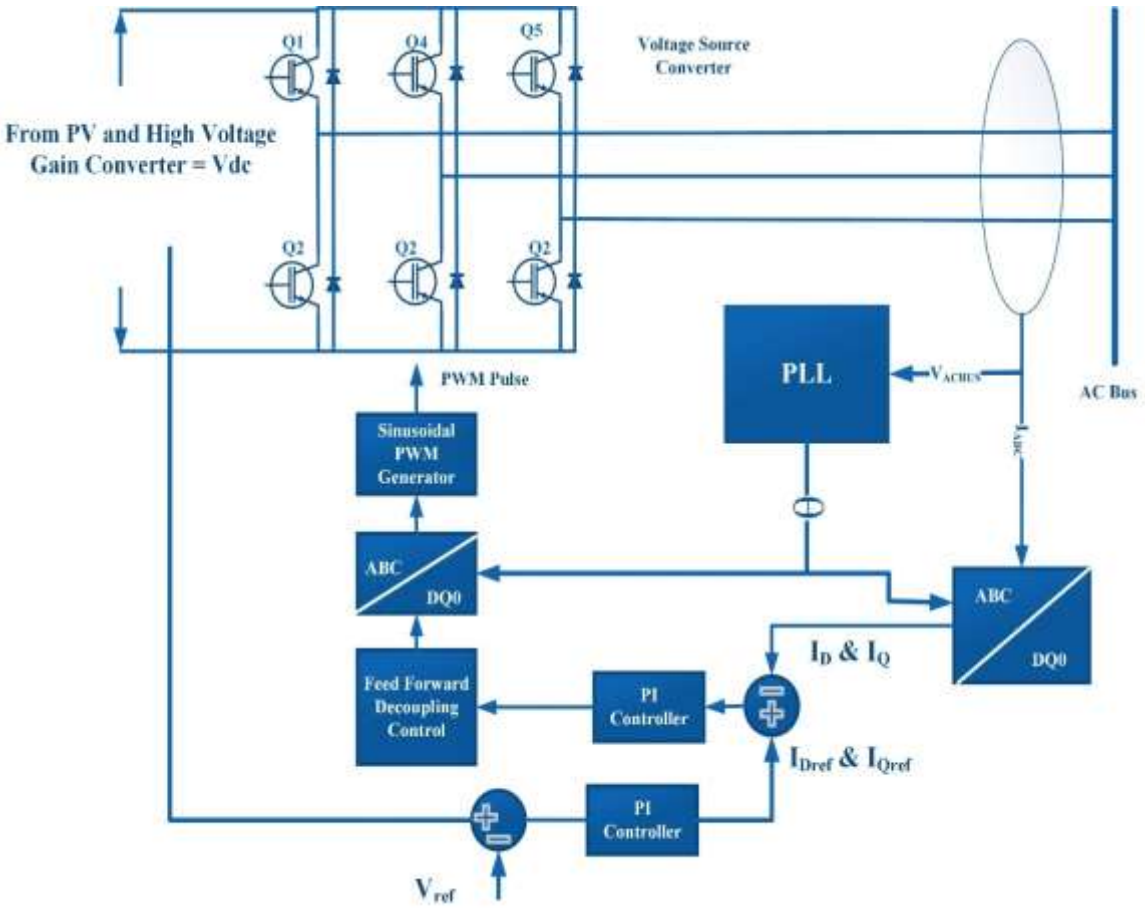

Figure 4.4. Three Phase grid-linked PV systems with inverter control

4.5 DC–AC converter

High-frequency harmonics in the grid system are reduced by the inverter's integrated AC filter, which converts DC energy into AC power. Based on the output of the parameter control technique, the controller generates PWM logic signals for the switches of the inverter. Figure 4.4 illustrates a block schematic of a typical inverter control system. The DC connector and filtering circuitry are auxiliary components, while the IGBTs and filters are the main components. A 600 µF capacitor stabilizes the input voltage to the inverter system from the DC power source. To mitigate the impact of grid harmonics from the inverter's high-frequency components, an alternating current (AC) filter [25] connects the device to the grid. The inverter's regulator system consists of a voltage control

loop and an inner current loop. The PI controller utilizes an inner current loop and a DC link voltage control to regulate and stabilize the DC link voltage Vdc. The inner loop control current controller energizes the VSI inverter with a predetermined amount of energy, enhancing the reliability of the electricity. Table 4.2 provides details on grid-connected inverter systems.

Table 4.2. Inverter-fed grid system specification

S. No.	Description	Values	Unit
1	Voltage per phase of the grid (V_g)	230	V
2	DC link voltage (V_{dclink})	400	V
3	DC link capacitor (C_{dc})	600	µF
4	Grid Frequency (F)	50	Hz
5	Inverter Frequency (F_{sw})	10	kHz
6	Inductor Filter (L_1)	4.06	mH
7	Inductor Filter (L_2)	4.305	mH
8	Capacitor Filter (C)	6.23	µF

4.6 Closed loop system modelling

4.6.1 Phase-Lock Loop (PLL)

PLL systems, like the one shown in Figure 4.4, enable grid-connected inverters to ascertain the phase angle of the grid swiftly and accurately. Figure 4.5 displays the layout of the synchronous PLL frame block. By setting Vdq to 0 and employing the PI regulator to constrain error, the rotational frequency can be adjusted. It is necessary to integrate the angular frequency before computing the phase angle.

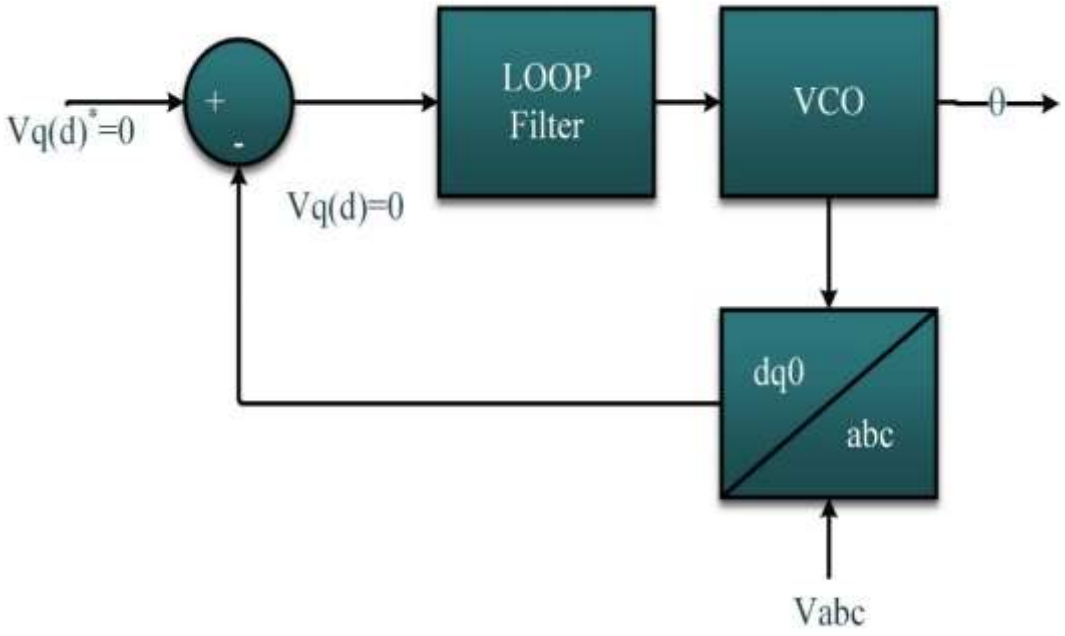

Figure 4.5. Phase Locked Loop structure

4.6.2 Voltage regulator controller

The DC link capacitor is positioned between the inverter's DC bus and the high-gain boost converter in a solar photovoltaic (PV) grid system. It enhances electricity quality and safety while meeting the standards set by the grid system. The DC link capacitor voltage controller, responsible for power distribution control, can be adjusted. A reference peak current for the entire grid is generated using a PI controller. The input to the inner loop is provided by the output of the outer loop. Equation (4.6) illustrates the DC-link voltage regulator model.

$$I_{ref} = \int K_{I1} \times e + K_{p1} \times e \qquad (4.6)$$

Where e represents the voltage drop between the measured values and the reference values. The PI controller receives the expected error to maintain the voltage across the DC link as low as possible. Consistent DC connection voltage across the high-gain boost converter and the inverter is essential to prevent total harmonic distortion (THD), which is a primary cause of poor grid power quality

4.6.3 Current controller

The current controller is crucial for improving power quality in grid-connected mode. It is constructed with a PI controller for connection voltage to compensate for current inaccuracies, as shown in Figure 4.4.

4.7 Artificial Ecosystem Algorithm Optimized PI Controller

PI controllers are a type of response loop control built using linear parameters, and they are used in processes dependent on load conditions. When selecting an inverter controller, performance, ease of installation, and dependability are crucial factors. To effectively regulate the injection of actual power into the utility system and maintain the voltage of the DC link on the inverter side, the PI controller is commonly used in AC voltage systems. The voltage and current harmonics, crucial for the overall power quality of the power system, are strongly influenced by the nonlinearity performance of loads and inverters. The use of an inductive filter in grid-connected inverters has been the subject of various studies. Controller settings can be conveniently chosen from the full range of allowable controller parameters for the system when the current controller and active damping interact appropriately.

Reductions in grid impedance can significantly impact system stability, as indicated by research on grid current control. The PI controller's reliability and ease of use in synchronous reference frames have led to its frequent deployment. However, achieving a stable and optimal solution in the face of nonlinear load variations and grid disturbances remains challenging with PI controllers. The use of fractional-order PI controllers has been shown to enhance the performance of three-phase solar PV systems. Additionally, using finite model predictive control, it has been demonstrated that the filter inductor, also utilized in grid-

linked inverter systems, can minimize current harmonics. Consequently, this type of control introduces additional layers of complexity to an inverter system.

In this study, the Artificial Ecosystem algorithm optimization approach is utilized to reduce transient response, achieve low steady-state error, and eliminate temporal overshoot caused by abrupt changes in load in a three-phase grid-connected PV inverter system. The optimal Kp and Ki parameters can be quickly determined by a real-time optimization approach using the Artificial Ecosystem algorithm. In case of an input error, the Artificial Ecosystem employs an optimization algorithm to respond promptly. The suggested inverter control system with the Artificial Ecosystem algorithm is depicted in Figure 5.6. By minimizing the error between the voltage regulator and the current controllers through the use of an artificial ecosystem, the PI controller's parameters are optimized. Further details about the limitations and objectives of the Artificial Ecosystem method are discussed later on. The merits and demerits of various methods, including the traditional Ziegler-Nichols (ZN) approach, evolutionary algorithms, neural fuzzy logic, fuzzy logic, and the Artificial Ecosystem algorithm, are outlined in Table 4.3. It can be observed in the table below that the Artificial Ecosystem algorithm is generally faster. Consequently, the Artificial Ecosystem approach does not require the use of inference rules during construction, unlike the Augmented full-state feedback controller, neural fuzzy logic, and fuzzy logic controllers. The ideal PI controller parameter values with reduced response times can be quickly and easily identified using a single solution space and the Artificial Ecosystem technique.

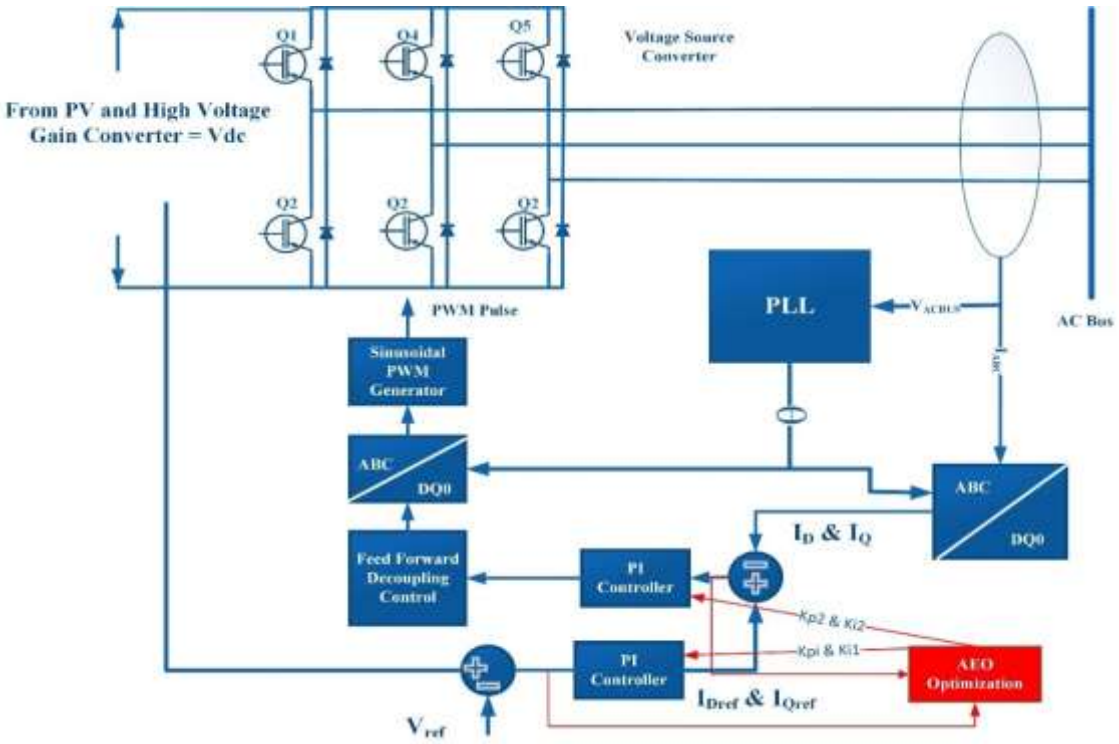

Figure 4.6. Proposed AEO-optimized PI-controlled inverter for grid-linked PV

4.7.1 Objective function

The PI controller's parameters are adjusted by minimizing the error between the voltage regulator and the current controllers using an artificial ecosystem. Later, we discuss the purpose and constraints of the Artificial Ecosystem technique in more detail. The error is denoted by the function E(t), the weight coefficients by C1 and C2, the maximum time by Tmax, and the total harmonic distortion of the output current by THDI.

$$\min f(y) = C1 \times \int_0^{Tmax} e(t)^2 dt + C2 \times \sum_0^{Tmax} THD_I \qquad (4.7)$$

Table 4.3. Merits and demerits of the control method

S. No.	Method	Data Training	Rules	Function calculation	Parameters settling	Reference Paper
1	ZN Method PI	NA	NA	NA	Calculation is simple	[6]
2	The augmented full-state feedback controller	NA	Yes	NA	trial and error method	[7]
3	Fuzzy neuro system	Yes	Yes	NA	It needs huge parameters	[9-11]
4	GA	NA	NA	Yes	It needs huge parameters	[12]
5	Artificial Ecosystem	NA	NA	Yes	It needs fewer parameters	[17-18]

4.7.2 Problem constraints

When operating in grid-linked mode, a PV system is governed by optimal parameters, including four decoupled PI controller parameters (Kp1, Ki1, Ki2, and Ki3). The formulation of an inverter for a three-phase PV system connected to the grid includes a DC link voltage and current controller.

$$\min f(y) = C1 \times \int_0^{T_{max}} e(t)^2 dt + C2 \times \sum_0^{T_{max}} THD_I$$

$$time \quad \begin{array}{c} L_1 \le K_{p1} \le U_1 \\ L_2 \le K_{i1} \le U_2 \\ L_3 \le K_{p2} \le U_3 \\ L_4 \le K_{i2} \le U_4 \end{array} \tag{4.8}$$

$$y = \{K_{p1}, K_{i1}, K_{p2}, K_{i2}\} \tag{4.9}$$

L1, L2, L3, L4, U1, U2, U3, and U4 specify the upper and lower bounds for the Kp1, Ki1, Kp2, and Ki2 parameters in this optimization problem. Then, we introduce the Artificial Ecosystem method to solve for these parameters, namely Kp1, Ki1, Kp2, and Ki2.

4.8 Artificial Ecosystem Algorithm

Our optimization technique employs three operators: production, consumption, and destruction, all based on a synthetic ecosystem. The primary objective of the initial operator is to enhance the ratio of exploration to exploitation. Introducing a second operator enhances the algorithm's capacity to explore new spaces. Recommendations are provided to encourage the adoption of the algorithm for the third operator. Figure 4.7 (a) illustrates some of the most crucial criteria used by AEO when attempting to find a solution.

- Producers, consumers, and decomposers make up the three major classes of organisms in every given ecosystem.
- A population has a single producer.
- There is only ever one of each kind of decomposer in every given population.
- The rest of a population is made up of eaters, and each individual in this group has an equal chance of evolving into a carnivore, herbivore, or omnivore.

- Each person's level of healthiness in a population may be quantified by calculating their "fitness value" in terms of the population function. Since a higher function fitness value indicates a higher energy level in a minimization problem, the population is sorted from highest to lowest in terms of function fitness value.

In this ecosystem, each creature has its fitness rankings displayed, and the black arrows represent the flow of energy. Individuals with a fitness value for a function greater than zero are classified as producers, while those with a fitness value less than zero are classified as decomposers. Figure 4.7 (b) indicates that the consumer group includes herbivores (x2 and x5), omnivores (x3), and carnivores (x4 and x6).

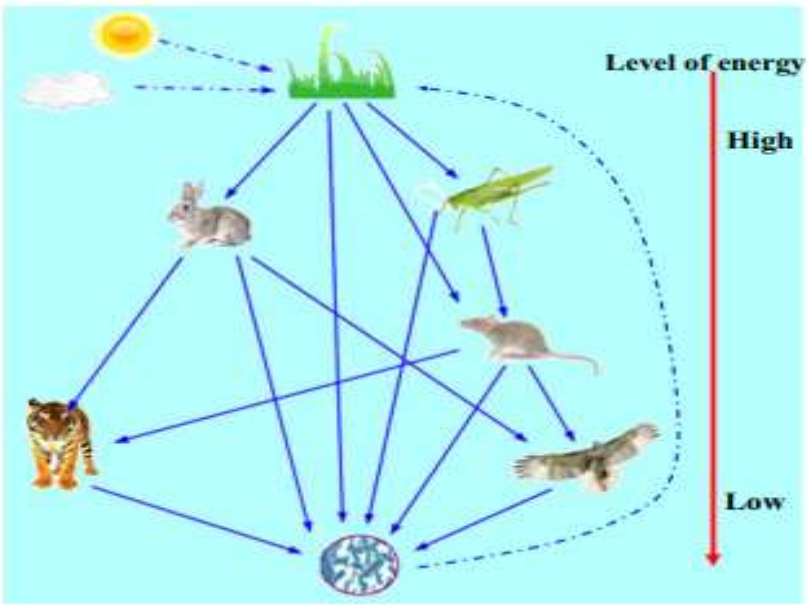

Fig. 4.7. (a) Energy flow in an ecosystem

In an ecosystem, producers utilize carbon dioxide, water, sunlight, and nutrients from decomposers to create food energy. In AEO, the best individual (the decomposer) in a population updates the poorest individual (the producer) on the lower and upper boundaries of the search space. The producer then uses this

information to guide the rest of the population (herbivores and omnivores) toward more productive regions. After the factory finishes producing the operator, anyone who wants to buy one may do so. Each consumer has the option of obtaining their calories from either a high-energy producer or

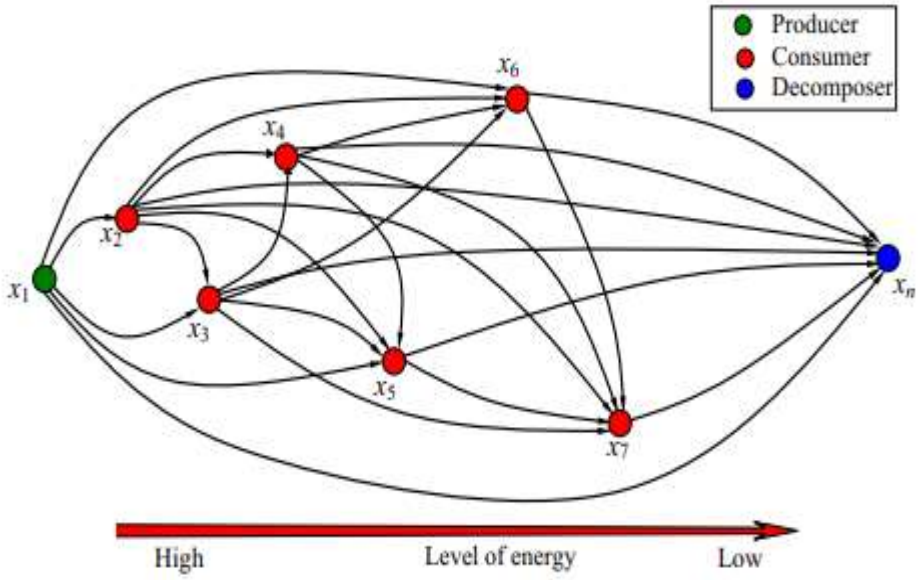

Fig. 4.7.(b) AEO ecosystem structure

a low-energy consumer chosen at random. Several species, such as cuckoos, bumblebees, deer, and lions, exhibit foraging behaviours similar to the mathematical operator known as the Levy flight. Given that certain steps are significantly longer in the long run, the Levy flight is a promising random walk for finding the global optimum as it can effectively explore the search space. To enhance the optimization effectiveness in biomimetic algorithms, Levy flying has been widely adopted. In a balanced environment, nutrients released during decomposition are utilized by producers. There will be a natural death rate for the population, and the decomposer will use chemical reactions to break down the bodies as they decompose. The pseudocode for the AEO algorithm is depicted in Fig. 4.7 (c).

The AEO method generates a random particle [88] to initiate fitness computation and determine the elite value for each parameter across the entire swarm. We utilized MATLAB code for the AEO algorithm on a PC with 2.50 GHz and 8GB of RAM. The flowchart of the AEO algorithm is depicted in Figure 4.7 (c). Using the AEO approach, optimal parameter standards for an inverter's PI controller are obtained to provide an active controller and higher switching state.

Randomly initialize an ecosystem X_i (solutions) and caculate the fitness Fit_i, and X_{best}= the best solution found so far.
While the stop criterion is not satisfied do
//Production//
For individual X_1, update its solution using equation (1).
//Consumption//
For individual X_i (i=2,...,n),
// Herbivore //
If $rand$<1/3 then update its solution using equation (6),
// Omnivore //
Else If 1/3≤$rand$≤2/3 then update its solution using equation (7),
// Carnivore //
Else update its solution using equation (8),
End If.
End If.
Caculate the fitness of each individual.
Update the best solution found so far X_{best}.
// Decomposition//
Update the position of each individual using equation (9).
Caculate the fitness of each individual.
Update the best solution found so far X_{best}.
End While.
Return X_{best}.

Fig. 4.7 (c) AEO algorithm pseudocode

4.9. Simulation results and discussion

To evaluate the effectiveness of the proposed Artificial Ecosystem approach for adjusting the PI controller settings in the inverter control technique, MATLAB/Simulink was used to create a 2-kW grid-linked PV system with a three-phase setup. The validation of the suggested Artificial Ecosystem method for the inverter control system was carried out using the following MATLAB implementation and testing results. The key findings include optimal PI controller settings, a comprehensive comparison of results achieved with and without optimization, and a voltage Total Harmonic Distortion (THD) analysis. Specifically, it demonstrates how the suggested approach enhances the characteristics of the single-phase grid system integrated with solar PV.

The final PI controller settings for the three-phase grid-linked PV system are presented in Table 4.4. These settings were incorporated into the control algorithm of the inverter controller to improve the overall performance of the inverter system. The initial values for the PI controllers of the inverters were determined through trial and error, which was the method used in the first Simulink/MATLAB implementation of the three-phase grid-linked PV system. During the modeling process of the Artificial Ecosystem's operation, the model underwent one hundred iterations. Table 4.4 showcases the final values of the PI controllers after 100 iterations.

Table 4.4 presents the optimal values of Proportional-Integral (PI) controllers for both voltage and current control, obtained using the Artificial Ecosystem (AEO) algorithm, and compares them with values obtained from the Ziegler-Nichols (ZN) method. For the PI voltage controller, the ZN method yields a proportional gain (Kp1) of 0.01 and an integral gain (Ki1) of 1.5, while the AEO algorithm recommends slightly higher values of Kp1 as 0.02 and Ki1 as 2.

Table 4.4. Optimum Value of PI voltage and current controller using AEO algorithm

Method	**PI Voltage Controller**		**PI Current Controller**	
	K_{p1}	**K_{i1}**	**K_{p2}**	**K_{i2}**
ZN method	0.01	1.5	7.6	125
Artificial Ecosystem	0.02	2	8.5	100
Parameter	**Worst**	**Best**	**Mean**	**Standard Deviation**
Artificial Ecosystem	35.55	31.02	31.56	1.305

Similarly, for the PI current controller, the ZN method results in Kp2 of 7.6 and Ki2 of 125, whereas the AEO algorithm suggests Kp2 as 8.5 and Ki2 as 100. The table also presents the performance evaluation of the AEO algorithm by listing the worst, best, mean, and standard deviation of the parameter values. For the AEO algorithm, the worst, best, and mean values of the PI controller parameters are 35.55, 31.02, and 31.56, respectively, while the standard deviation is 1.305. These results indicate that the AEO algorithm successfully optimizes the PI controller parameters, leading to improved performance and stability in voltage and current control applications. The optimized values are closer to the best-performing configurations, and there is a relatively low deviation, highlighting the effectiveness of the AEO algorithm in controller parameter optimization.

The Augmented Full-State Feedback controller, the Ziegler-Nichols (ZN) algorithm technique, and the Artificial Ecosystem (AEO) algorithm are depicted in Figure 4.8 for controlling the DC link voltage. The results reveal that the rise time of the PI controller is just 0.02 seconds when the Artificial Ecosystem technique is used, 0.025 seconds when the ZN method is used, and 0.03 seconds

when the Augmented Full-State Feedback controller approach is used. The inverter system's input power is stabilized with the use of the Artificial Ecosystem algorithm rather than a regular PI controller. Finally, in terms of steady-state performance, the Artificial Ecosystem's PI controller algorithm fared better than the standard PI controller. The inverter can maintain a consistent DC input from the Artificial Ecosystem thanks to the algorithm's ability to compensate for transient impacts. By stabilizing the DC link input voltage, the inverter may produce an AC output waveform with a low ripple factor %.

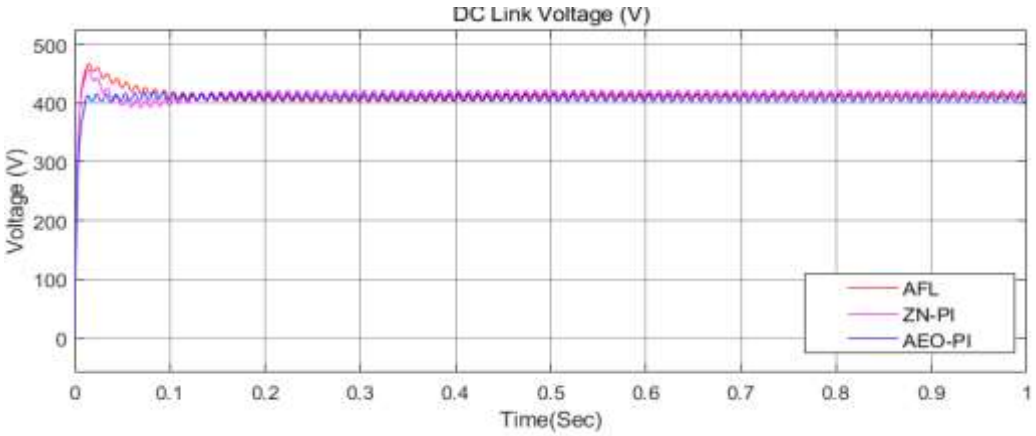

Figure 4.8. The response of the DC link Voltage

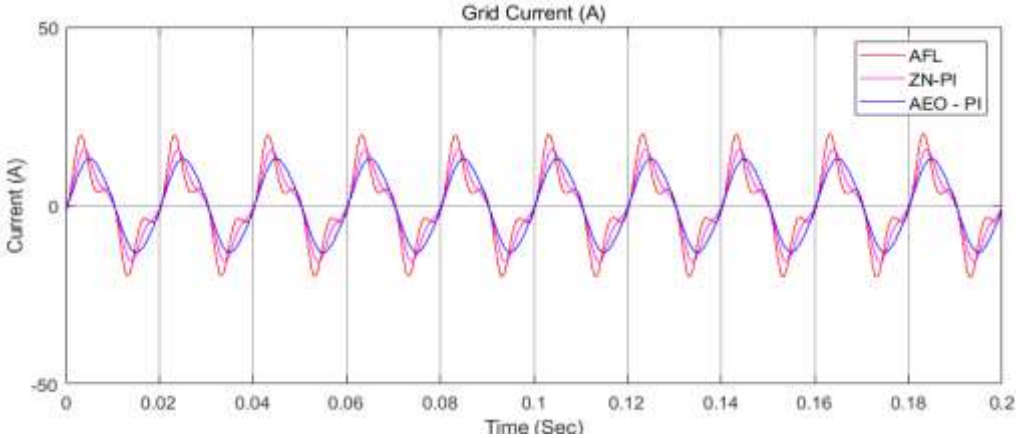

Figure 4.9. The response of the grid current at 1000 W/m^2

The single-phase grid current of the three-phase system is depicted in Fig. 4.9 and 4.10, respectively, for constant irradiance and step change in irradiance using

the controller. Simulations with PI controllers using the Ziegler-Nichols (ZN) method, an Augmented Full-State Feedback controller, and the Artificial Ecosystem algorithm method resulted in the grid system current seen in Fig. 4.9.

Minor noise and non-sinusoidal behaviour may be observed in the amplitude of the grid current produced by the PI controller with the Ziegler-Nichols (ZN) method and the augmented full-state feedback controller approach. As shown in Fig. 4.9, the grid current generated by a traditional ZN-PI controller exhibits a higher number of harmonics compared to the grid current generated by a PI controller employing the Artificial Ecosystem algorithm method, which produces a current waveform with fewer harmonics. This is attributed to the inverter control scheme utilizing an appropriate control algorithm that reduces the harmonic level in the grid current while maintaining stable output voltage.

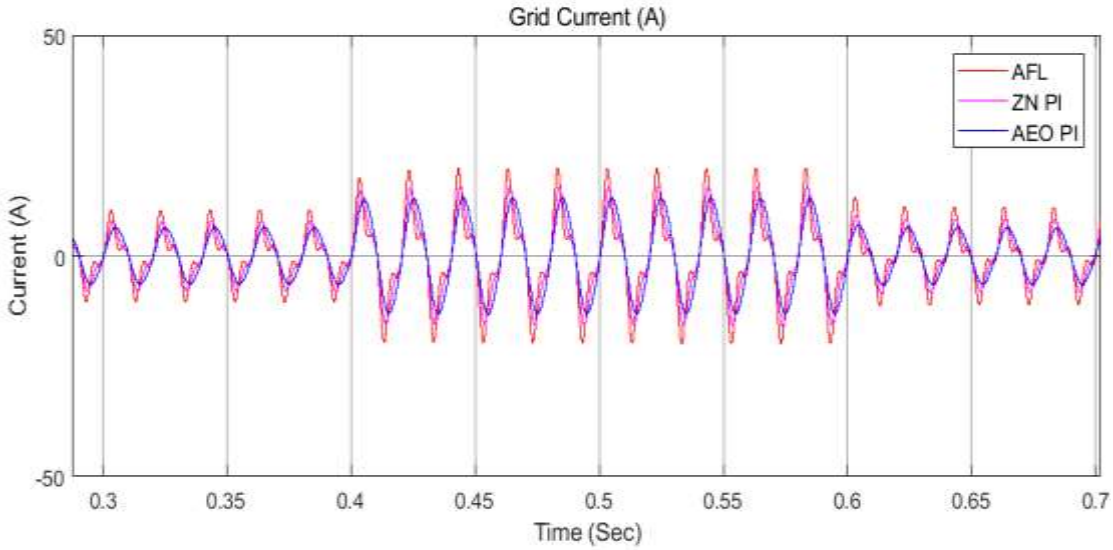

Figure 4.10. The response of the grid current at varying irradiance conditions

The grid currents of systems with a Ziegler-Nichols (ZN) PI controller and systems with a PI controller utilizing the Artificial Ecosystem algorithm approach are compared in Figure 4.10. There is a statistically significant impact on grid current between (0.4-0.6) s due to irradiance changes in PV systems.

Currents vary because the grid receives more electricity when the sun is shining brightly. The current waveform of the PI controller without the Artificial Ecosystem algorithm has a greater harmonic level than that with the Artificial Ecosystem approach. Based on this finding, we can conclude that the control system effectively maintains stable voltage and current amplitudes regardless of varying irradiance conditions.

The inverter demonstrates its potential for power flow analysis when used in conjunction with a grid-connected inverter system to extract solar PV power and feed it back into the utility. Figure 4.11 depicts the step-momentary scenario, which occurs when there is a sudden shift in available light. Sometimes it's possible to assess the overshoot. The fluctuating nature of the grid-linked system is directly proportional to the flexibility of solar irradiation. Figures 11(a) and 11(b) show that the inverter system exhibits numerous transients and overshoots in the grid and PV-contributed power when a step transient condition occurs, unlike the PI controller using the Artificial Ecosystem algorithm technique. In Fig. 11(c), we can see that the Artificial Ecosystem's algorithm-based control system mitigates transient impacts overall and prevents overshoot, allowing the system to return to a steady state.

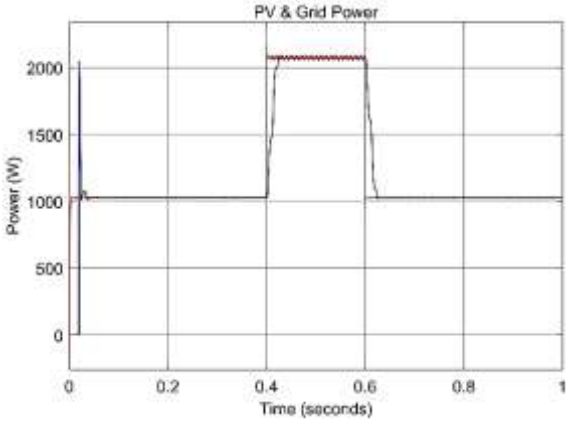

(a) AFL

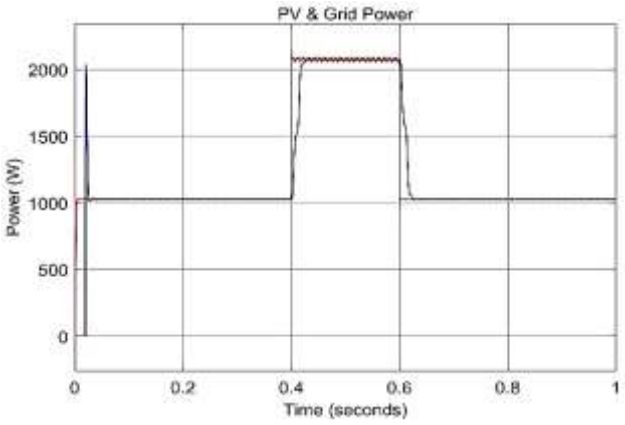

(b) ZN PI

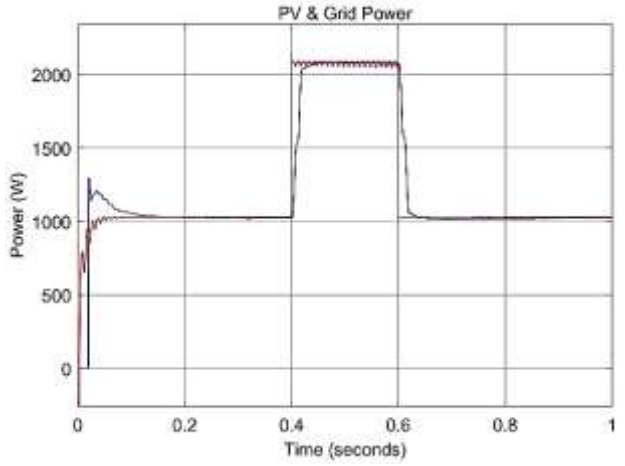

(c) AEO PI

Figure.4.11. PV Power and Grid Power

Electricity from a system with low harmonic content is essential for grid connection. A low total harmonic distortion (THD) on the current waveform indicates better and more linear power for the user, resulting in lower energy consumption. The power factor of the load suffers when the THD factor of the load is high. The THD factor of the grid system

is high due to the low load consumption. An improved regulator and Fast Fourier Transform analysis might be used to reduce the THD of the grid current to around 5%, representing a significant improvement.

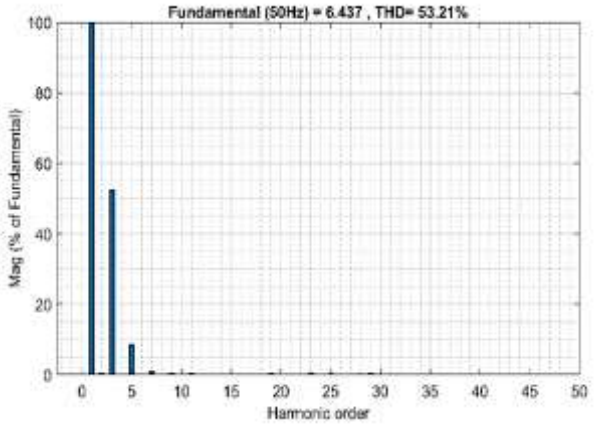

(a) AFL

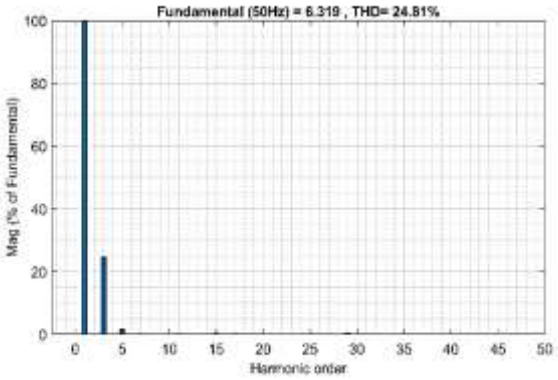

(b) ZN PI

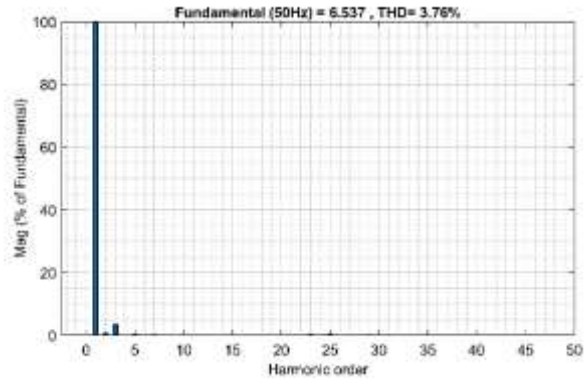

(c) AEO PI

Figure.4.12. THD of the Grid Current

In Figure. 4.12, the harmonic spectrum of grid current waveforms is shown using a ZN-PI controller, an augmented full-state feedback controller, and a PI controller based on an Artificial Ecosystem algorithm. The total harmonic distortion (THD) of the grid current is 53.21% when using the ZN-PI controller,

24.81% when using the augmented full-state feedback controller method, and 3.76% when using the Artificial Ecosystem algorithm. The use of the Artificial Ecosystem algorithm can improve the controller algorithm of the inverter system and, consequently, enhance the system's performance.

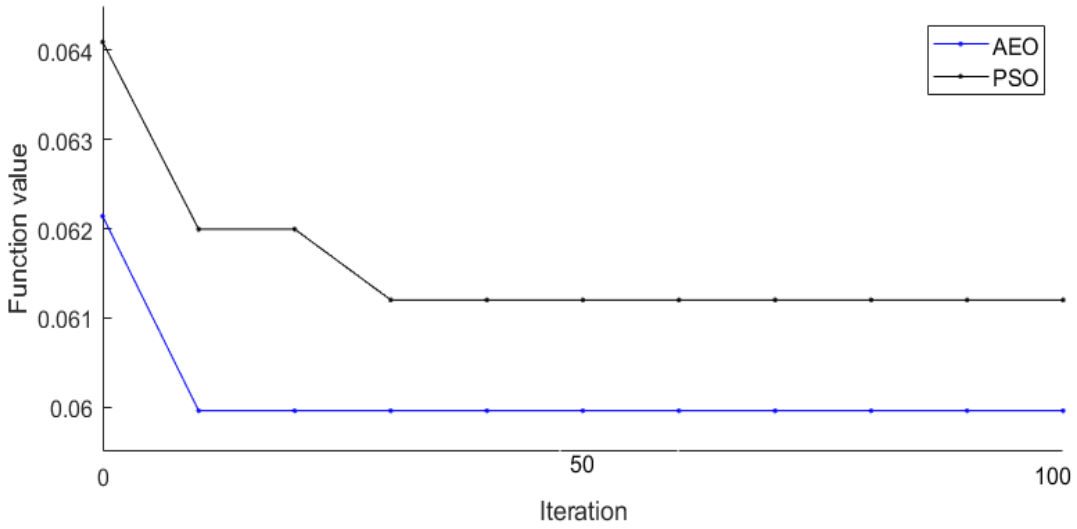

Figure.4.13. Convergence Plot

Contrasting with Figure 4.13, where the PSO approach converges after 30 iterations, the Artificial Ecosystem procedure reduces the fitness function and reaches the value in just 10 iterations. After 100 optimization cycles, the most effective PI controller settings were discovered to be Kp1, Ki1, and Ki2. The optimum settings for a three-phase inverter's current controller, voltage regulators, and PI controller may be determined with the use of an Artificial Ecosystem. The outcomes show that the Artificial Ecosystem approach is superior to the PSO algorithm in determining the optimal PI controller settings when compared to the enhanced full-state feedback controller, ZN technique.

Table 4.5 Comparison of augmented full-state feedback controller, ZN method, PSO Method and Artificial Ecosystem Algorithm

Method	Time domain specification of DC link Voltage			Current THD (%)	Efficiency (%)
	Rise Time (ms)	Overshoot (%)	Settling Time (ms)		
ZN method	30	21	250	53.21	94
The augmented full-state feedback controller	25	20	240	24.81	96
PSO Method	23	15	200	4.21	97
Artificial Ecosystem Algorithm	20	2	160	3.76	98

Table 4.5 presents a comprehensive comparison between the performance of the standard Proportional-Integral (PI) controller and the optimization achieved through the Artificial Ecosystem algorithm, along with other techniques such as the Augmented full-state feedback controller, Ziegler-Nichols (ZN) method, and Particle Swarm Optimization (PSO) method. The table evaluates critical parameters including rise time, overshoot, settling time, current Total Harmonic Distortion (THD), and system efficiency. The results demonstrate that the recommended method, i.e., the Artificial Ecosystem algorithm, surpasses the alternatives in several aspects. Notably, the THD for grid current achieved using the Artificial Ecosystem algorithm is notably lower at 3.76%, showcasing its ability to reduce harmonic distortions in the system. Moreover, improvements in time domain specifications such as settling time (20 ms) and rise time (160 ms) are achieved more rapidly compared to other optimization methods, indicating the efficiency of the Artificial Ecosystem approach in achieving quicker response times. Additionally, the negligible overshoot of about 2% with the

Artificial Ecosystem algorithm is favourable compared to other techniques, further highlighting its stability and precision. However, it's worth noting that the overall system efficiency is recorded at 98%, which, while relatively high, is slightly lower compared to some alternative approaches.

4.10 Simulation Results During Partial Shading Conditions

The simulation process involved the use of MATLAB and Simulink to analyze the effects of partial shading on the photovoltaic (PV) system. One group of the PV array was kept at a constant irradiance of 1000 W/m², while the irradiance for another group varied every second to mimic partial shading. For instance, the irradiance changed from 1000 W/m² to 800 W/m² within the first

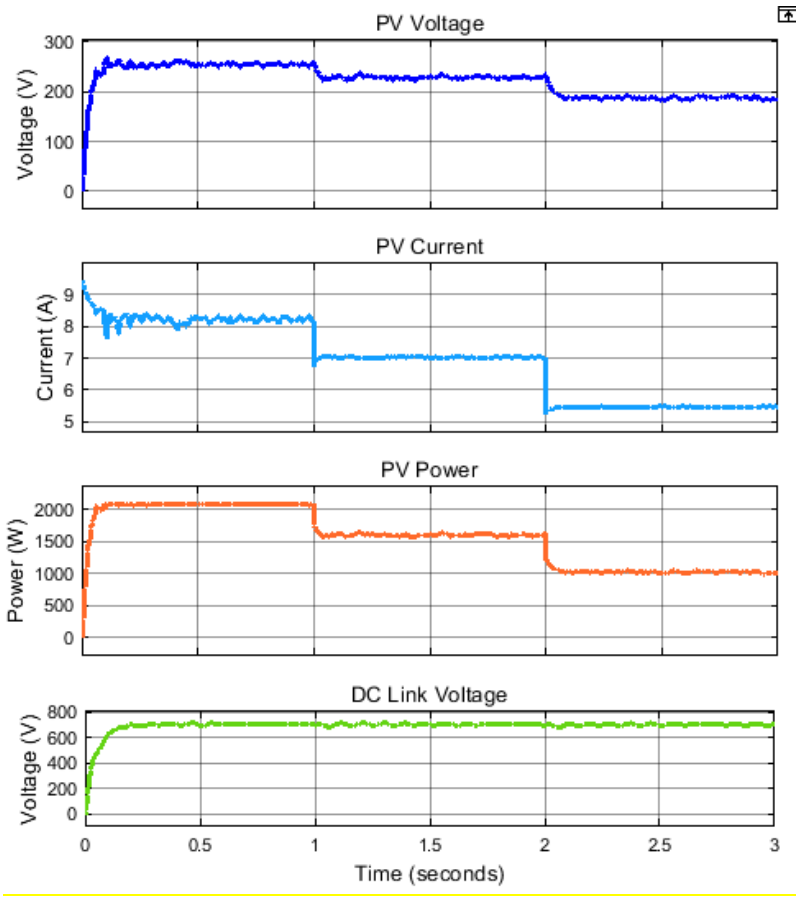

Fig.4.14. Simulation result of PV voltage, current, power and DC link voltage with optimal HOA parameter.

second and further decreased to 600 W/m² in the subsequent second. Figure 4.14 illustrates the simulation results, including PV voltage, PV current (I), PV power, and DC link voltage. During the first second, the PV array generated 2049 W of power with a PV voltage of 250 V and a PV current of 8.19 A. In the second second, the power was reduced to 1540 W, accompanied by a decrease in PV voltage to 220 V and PV current to 7 A. Finally, in the third second, the power dropped to 1000 W with a PV voltage of 198 V and a PV current of 5.05 A.

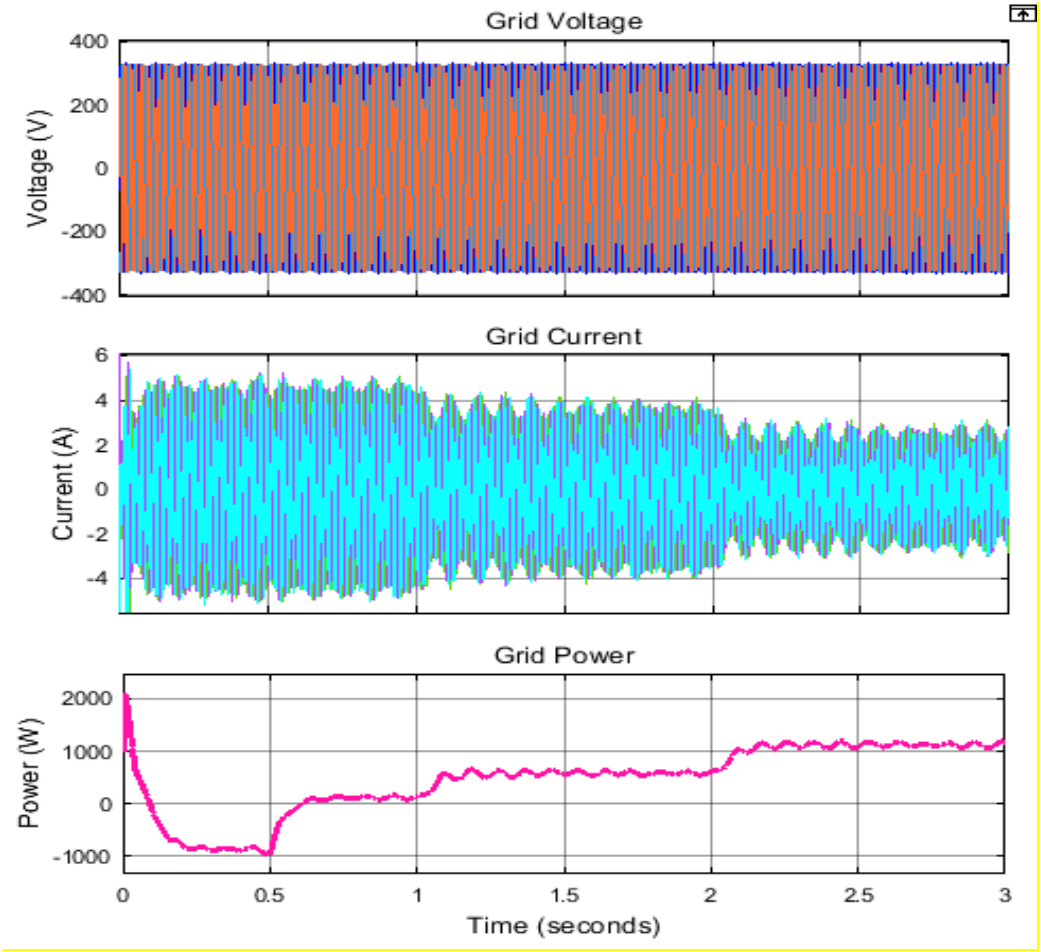

Fig.4.15 Simulation result of grid voltage(V), current(I) and power(P).

The simulation results for the grid, including grid voltage, grid current, and grid power, are shown in Figure 4.15. The grid voltage remains stable at 400 V throughout the simulation. The grid current and power vary depending on the

power output from the PV array, as indicated in the figure. Initially, from 0 to 0.5 seconds, the grid receives around 950 W of power because the PV array generates more excess power than the load requires. However, from 0.5 to 3 seconds, the grid supplies power to the load as the PV power becomes insufficient to meet the load demand.

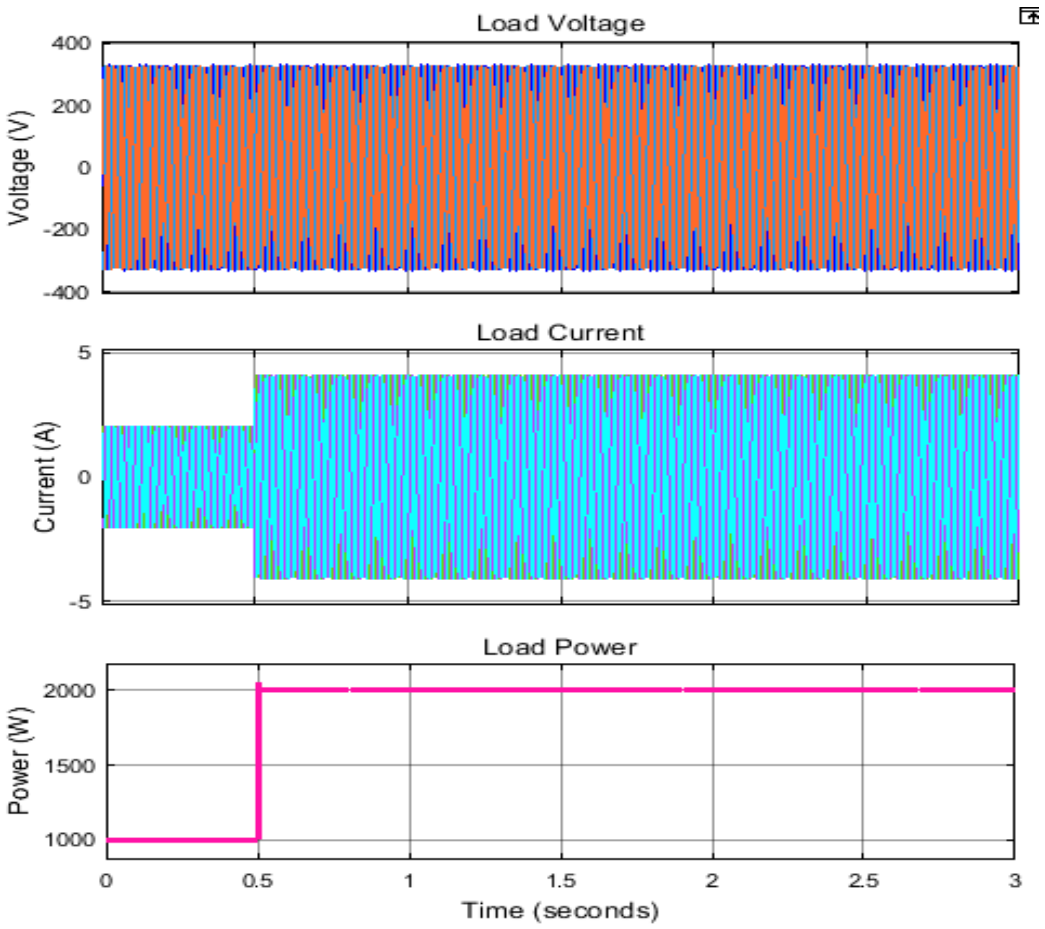

Fig.4.16. Simulation result of grid voltage, current and power.

Figure 4.16 illustrates the simulation results for load parameters, specifically load voltage, load current, and load power. The load voltage is consistently maintained at 400 V, while the load current changes based on the load added to the system. The load power is 1000 W from 0 to 0.5 seconds and increases to 2000 W from 0.5 to 3 seconds.

The test results show that there is a maintained power balance between the energy sources and the load.

4.11. Experimental results and discussion

This section presents experimental verification of the efficiency of the suggested AEO algorithm-optimized PI-controlled three-phase grid-linked system. The hardware configuration for the suggested task is depicted in Fig. 4.17.

Figure. 4.17 Hardware Setup of the Proposed Work.

The test rig includes a 2-kilowatt photovoltaic (PV) panel on a rooftop, a boost converter and inverter power module, a PIC microcontroller for maximum power point tracking, a DC link voltage controller and inverter control logic, a digital storage oscilloscope, and a power quality analyser. PIC microcontrollers are used to implement the AEO-optimized PI controller's control logic through a C application. The experimental system is put through a series of tests with a steady load.

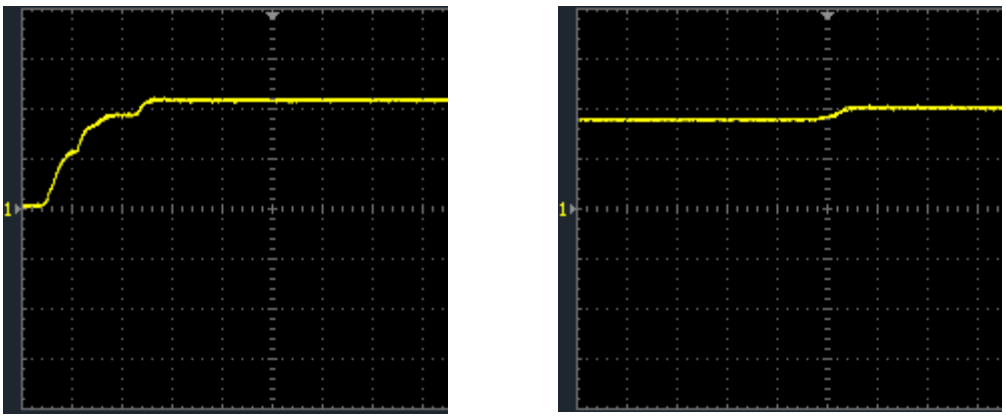

(a) PV Voltage (left) & Current (Right)

X-axis – 10ms/div & Y axis – 200 V/div (Left) & 2 A/div (Right)

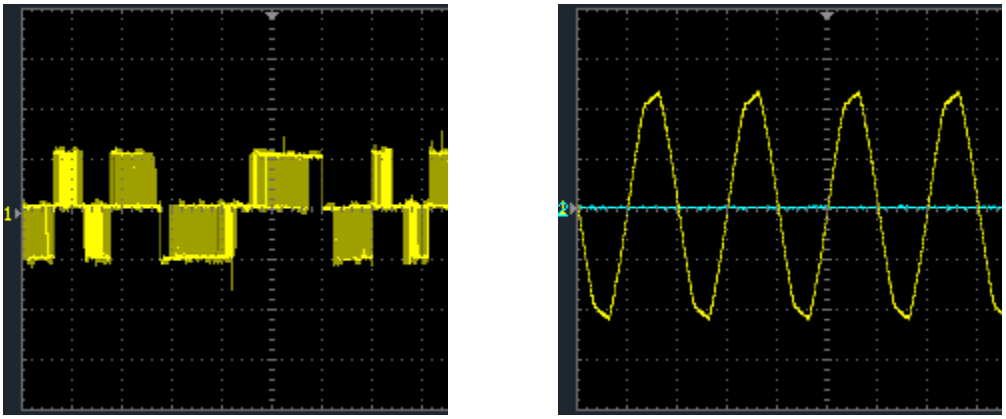

(b) Inverter Voltage (left) & grid Voltage (Right)

X-axis – 10ms/div & Y axis – 400 V/div (Left) & 150 V/div (Right)

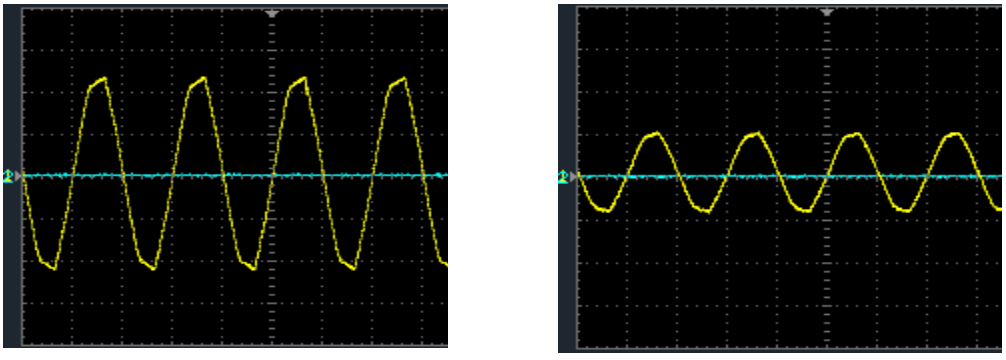

(c) Grid Current (left) & Load Current (Right)

X-axis – 10ms/div & Y axis – 4 A/div (Left) & 2A/div (Right)

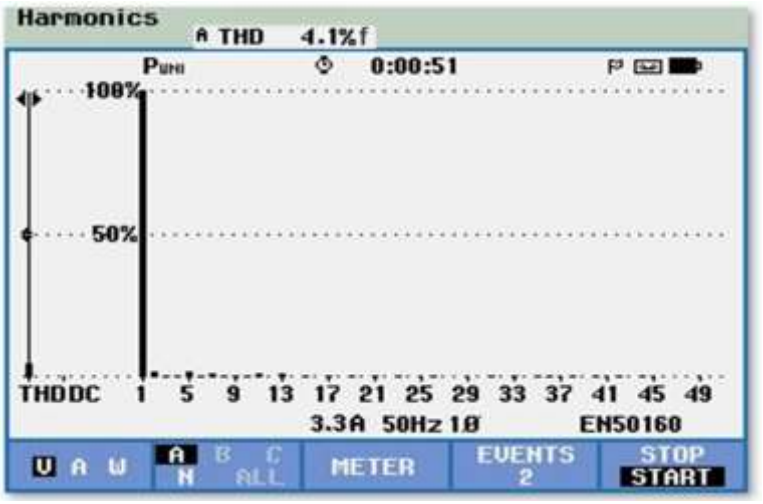

(d) THD of the Grid current

Figure. 4.18. Experimental results of the proposed system

The experimental findings for the proposed system are summarized in Fig. 4.18. PV voltage and current are displayed in Figure 4.18 (a). The power output from the PV panel is 1858.5 W, with a voltage of about 413 V and a current of about 4.5 A, resulting in a power output of around 413 V * 4.5 A. Voltage from the inverter and the grid is shown in Figure 4.18 (b). The inverter's peak voltage is 413 V, which is filtered by a harmonic LCL filter before being sent into the grid. The average voltage on the grid is about 233.3 V, with a peak value of roughly 330 V. The grid and load current are depicted in Figure 4.18(c). The grid current peaks at 9 A, while the load current peaks at 2 A. The grid current is 6.36 A, and the load current is 1.41 A, both expressed as root-mean-squared (RMS) values. Electricity consumption by the load is 328.9 W, while power output to the grid is 1483.8 W. There is a total of 1812.7 W of electricity available, resulting in a remarkable 97.5% efficiency. The THD spectra of the grid current are shown in Figure 4.18 (d), indicating a THD in the grid current of 4.1%. A comparison

between the modelling and experimental findings of the suggested work is presented in Table 4.6. Table 4.6 illustrates that there are minimal differences between the simulation and experimental data. In the simulation, the PV system generates 1992 W of power, whereas, in practice, it produces 1858.5 W. Similarly, the power at the grid and load in the virtual environment is 1952.2 W, while in the real world, it amounts to 1812.7 W.

Table 4.6. Parameter Comparisons in Experimentation and Simulation

Parameter	**Experimentation Results**	**Simulation Results**
PV Voltage (V)	413	415
PV Current (A)	4.5	4.8
PV Power (W)	1858.5	1992
Grid & Load Voltage (V)	233.3	230
Grid + Load Current (A)	7.77	8.48
Grid + Load Power (W)	1812.7	1952.2
Efficiency (%)	97.5	98
THD of the Grid current (%)	4.1	3.76

Both theoretical and practical evaluations indicate the system's effectiveness at approximately 98%. In terms of Total Harmonic Distortion (THD) of the grid current, the simulation records 3.56%, whereas the experiment shows 4.1%. These results highlight that an AEO-optimized PI voltage and current-regulated three-phase grid-connected PV system performs exceptionally well across various scenarios. The minor discrepancies between simulation and actual performance demonstrate the robustness and accuracy of the AEO optimization in enhancing system efficiency and stability.

4.11 Summary

This chapter describes how to tune the PI controller using AEO optimization and compares it to the AFL and ZN PI controllers. From the test results, the AEO-optimized PI controller provides better results than a conventional PI controller and AFL controller in terms of rise time, overshoot, settling time, current THD, and system efficiency. Finally, experimental results of the AEO-optimized PI-controlled grid-connected PV system are measured and analysed

Chapter 5

Conclusions and Future Scope of Work

5.1. Conclusions

This thesis examines the integration of various Maximum Power Point Tracking (MPPT) algorithms into grid-connected solar PV systems. It starts with a literature review and explains the research's purpose, outlining the thesis structure and research goals. Chapter 2 presents findings and discussions on multiple MPPT algorithms, including fixed voltage, Perturb and Observe, incremental conductance, fuzzy logic-based, and neural network-based algorithms, which are examined and simulated. Chapter 3 focuses on a grid-connected solar PV system, discussing a hybrid fuzzy logic/neural network-based variable step size MPPT algorithm and Horse Herd Optimization MPPT [71]. It covers PV array modelling, MPPT techniques, DC-DC converters, inverter design, simulation results, and experimental verification. Chapter 4 introduces an Artificial Ecosystem Optimization method to tune a PI controller in a grid-connected photovoltaic system, involving closed-loop system modelling, PV system modelling, and Peak Power Tracking algorithms, with presentation of experiment, simulation, and optimization outcomes. Chapter 5 summarizes and discusses the dissertation's findings and suggests ideas for future research in this area.

The findings of this dissertation's study are presented below.

- The implementation of Maximum Power Point Tracking (MPPT) for Photovoltaic Power Systems involves utilizing various techniques such as P&O MPPT, Incremental Conductance MPPT, ANN MPPT, Fuzzy Logic MPPT, and Hybrid Fuzzy Neural Variable Step Size P&O MPPT. MATLAB simulation results are compared for a 100 kW PV standalone system under

different climatic conditions in this proposed model [29], showcasing the simulation results of the proposed model. Among these

methods, tracking with Hybrid Fuzzy Neural-Network Variable Step Size P&O MPPT yielded the highest output power in terms of settling time, rise time, and peak power compared to other methods.

- The chapter presents a study on grid-connected photovoltaic systems that utilize Horse Herd Optimization Maximum Power Point Tracking (MPPT) and Hybrid Fuzzy Neural Network Variable Step Size Perturb and Observe (P&O) MPPT. The photovoltaic system connected to the grid was evaluated under both uniform irradiance and partial shading scenarios. The test results indicate that the Hybrid Fuzzy Neural Network with variable step size Perturb and Observe Maximum Power Point Tracking algorithm is efficient in extracting the maximum power from the photovoltaic array under both uniform irradiance and partially shaded conditions while considering load resistance conditions.

- The design and modelling of a grid-connected PV system with an AEO-optimized PI controller are explained. A detailed simulation of the artificial ecosystem-optimized PI voltage and current-controlled grid-connected PV energy conversion system is conducted for various operating conditions and compared with the ZN PI controller and AFL controller. The test results indicate that the AEO-optimized PI-controlled grid-connected PV system outperforms other methods in terms of THD, rise time, and settling time.

5.2 Future Scope of Work

The future scope of research in grid-connected PV systems encompasses several key areas for further advancement. Firstly, there is a need to develop more efficient and adaptive & Bioinspired MPPT algorithms that can dynamically adjust to changing environmental conditions, such as partial

shading or fluctuations in solar irradiance. These advanced algorithms have the potential to significantly enhance the energy yield of solar PV systems and improve their overall performance, especially under challenging operational circumstances. By focusing on the creation of novel MPPT algorithms, researchers can contribute to the continual improvement and optimization of grid-connected PV systems, making them more resilient and effective in harnessing solar energy.

Secondly, the integration of energy storage solutions, particularly batteries, with grid-connected PV systems represents a promising avenue for future research. This involves developing sophisticated control strategies and algorithms that can optimize the utilization of energy storage to ensure a continuous and stable power supply to the grid, even during periods of low solar irradiance or fluctuating demand. Investigating the economic aspects, such as cost-effectiveness and return on investment, will also be crucial in evaluating the viability and scalability of integrating energy storage with grid-connected PV systems. By addressing these aspects, researchers can pave the way for the widespread adoption of renewable energy sources and contribute significantly to the advancement of sustainable energy generation and grid stability.

References

1. International Energy Agency, https:// www.iea.org/statistics/topics/electricity/
2. Ministry of New and Renewable Energy (MNRE), The Government of India, 30-08-18, https://mnre.gov.in/
3. Luna-Rubio, R., Trejo-Perea, M., Vargas-Vázquez, D. and Ríos-Moreno, G.J., 2012. Optimal sizing of renewable hybrids energy systems: A review of methodologies. Solar Energy, 86(4), pp.1077-1088.
4. Siddaiah, R. and Saini, R.P., 2016. A review of planning, configurations, modelling and optimization techniques of hybrid renewable energy systems for off-grid applications. Renewable and Sustainable Energy Reviews, 58, pp.376-396.
5. Al-Falahi, M.D., Jayasinghe, S.D.G. and Enshaei, H., 2017. A review of recent size optimization methodologies for standalone solar and wind hybrid renewable energy systems. Energy conversion and management, 143, pp.252-274.
6. Tudu, B., Mandal, K.K. and Chakraborty, N., 2018. Optimal design and development of PV-wind-battery based nano-grid system: A field-on-laboratory demonstration. Frontiers in Energy, pp.1-15.
7. Upadhyay, S. and Sharma, M.P., 2014. A review of configurations, control and sizing methodologies of hybrid energy systems. Renewable and Sustainable Energy Reviews, 38, pp.47-63.
8. Cho J-H, Chun M-G, Hong W-P., 2016. Structure optimization of stand-alone renewable power systems based on multi-object function. Energies,9, 649.
9. Amutha, W.M. and Rajini, V., 2015. Techno-economic evaluation of various hybrid power systems for rural telecom. Renewable and Sustainable Energy Reviews, 43, pp.553-561.

10. Maleki, A., Ameri, M. and Keynia, F., 2015. Scrutiny of multifarious particle swarm optimization for finding the optimal size of a PV/wind/battery hybrid system. Renewable Energy, 80, pp.552-563.

11. Maleki, A., Khajeh, M.G. and Ameri, M., 2016. Optimal sizing of a grid-independent hybrid renewable energy system incorporating resource uncertainty, and load uncertainty. International Journal of Electrical Power & Energy Systems, 83, pp.514- 524.

12. Nehrir, M.H., Wang, C., Strunz, K., Aki, H., Ramakumar, R., Bing, J., Miao, Z. and Salameh, Z., 2011. A review of hybrid renewable/alternative energy systems for electric power generation: Configurations, control, and applications. IEEE Transactions on Sustainable Energy, 2(4), pp.392-403.

13. Malheiro, A., Castro, P.M., Lima, R.M. and Estanqueiro, A., 2015. Integrated sizing and scheduling of wind/PV/diesel/battery isolated systems. Renewable Energy, 83, pp.646- 657.

14. Bhuiyan, F.A., Yazdani, A. and Primak, S.L., 2014. Optimal sizing approach for islanded microgrids. IET Renewable Power Generation, 9(2), pp.166-175.

15. Zhao, B., Zhang, X., Li, P., Wang, K., Xue, M. and Wang, C., 2014. Optimal sizing, operating strategy and operational experience of a stand-alone microgrid on Dongfushan Island. Applied Energy, 113, pp.1656-1666.

16. Chauhan, A. and Saini, R.P., 2014. A review on integrated renewable energy system based power generation for stand-alone applications: configurations, storage options, sizing methodologies and control. Renewable and Sustainable Energy Reviews, 38, pp.99-120.

17. Sanajaoba, S. and Fernandez, E., 2016. Maiden application of Cuckoo Search algorithm for optimal sizing of a remote hybrid renewable energy System. Renewable Energy, 96, pp.1-10.

18. Hosseinalizadeh, R., Shakouri, H., Amalnick, M.S. and Taghipour, P., 2016. Economic sizing of a hybrid (PV–WT–FC) renewable energy system (HRES) for stand-alone usages by an optimization-simulation model: a case study of Iran. Renewable and Sustainable Energy Reviews, 54, pp.139-150.

19. Chenni, R, Makhlouf, M, Kerbache, T & Bouzid, 2007, 'A detailed modelling method for photovoltaic cells', Energy, Vol. 32, pp. 1724-1730.

20. Chian-Song Chiu, Ya-Lun Ouyang & Chan-Yu Ku 2012, 'Terminal sliding mode control for maximum power point tracking of photovoltaic power generation systems, Solar Energy, Vol. 86, pp. 2986-2995.

21. Chih-Tang 1957, Carrier generation and recombination in P–N junctions and P–N junction characteristics: Proc IRE , pp. 1228-1243.

22. Choudera, A, Silvestreb, S, Taghezouita, B & Karatepe, E 2013, 'Monitoring, modelling and simulation of PV systems using LabVIEW ', Solar Energy, Vol. 91, pp. 337-349.

23. Chouder, A, Silvestre, S, Sadaoui, N & Rahmani, L 2012, 'Modeling and simulation of a grid connected PV system based on the evaluation of main PV module parameters', Simulation Modelling Practice and Theory, Vol. 20, pp. 46-58.

24. Kashif, Zainal & George 2014, 'The performance of perturb and observe and incremental conductance maximum power point tracking method under dynamic weather conditions', Applied Energy, Vol. 119, pp. 228-236.

25. Sundareswaran, K., Vigneshkumar, V., Sankar, P., Simon, S.P., Nayak, P.S.R. and Palani, S., “Development of an improved P&O algorithm assisted through a colony of foraging ants for MPPT in PV system,” IEEE transactions on industrial informatics, 12(1), pp. 187-200, 2015.

26. Won CY, Kim DH, Kim SC, Kim WS, Kim HS. A New maximum power point tracker of photovoltaic arrays using fuzzy controller. Proceedings of the IEEE Power Elec. Specialists Conference, red Stick, the USA, 1994, p.396-403.

27. Subiyanto S, Mohamed A, Hannan MA. Intelligent maximum power point tracking for PV system using Hopfield neural network optimized fuzzy logic controller . Energy and Buildings, 2012; 51: 29-38.

28. Abd El-Shafy AN, Fahmy FH, Abou El-Zahab EM. Maximum-power operation of a stand-alone PV system using fuzzy logic control . Int J Numer Model, 2002;15:385-98. [29]. Mamdani EH, Assilian S. An experiment in linguistic synthesis with a fuzzy logic controller. Int.J Man-Machine Studies, 1975; 7(1):1-13.

29. Wai, R.J., Lin, C.Y., Lin, C.Y., Duan, R.Y. and Chang, Y.R., "High efficiency power conversion system for kilowatt-level stand-alone generation unit with low input voltage," IEEE Transactions on Industrial Electronics, 55(10), pp. 3702-3714, 2008.

30. Liang, Z., Guo, R., Li, J. and Huang, A.Q., "A high-efficiency PV module integrated DC/DC converter for PV energy harvest in FREEDM systems," IEEE Transactions on Power Electronics, 26(3), pp. 897-909, 2011.

31. Errouissi, R., Al-Durra, A. and Muyeen, S.M., "A robust continuous-time MPC of a DC-DC boost converter interfaced with a grid-connected photovoltaic system," IEEE Journal of Photovoltaics, 6(6), pp. 1619-1629, 2016.

32. Anthoula Menti, Dimitrios Barkas, Stavros Kaminaris, Constantinos S. Psomopoulos, Supraharmonic emission from a three-phase PV system connected to the LV grid, Energy Reports, 7(5), pp. 527-542, 2021.

33. Abdel Khalik, AS, Elserougi, A, Massoud, A, & Ahmed, S 2013, 'A Power Control Strategy for Flywheel Doubly-Fed Induction Machine Storage System Using Artificial Neural Network', Electric Power Systems Research, vol. 1, no. 96, pp. 267-276.

34. Adeola, Olorunfemi, O, Frank, O & Sosthenes, K 2013, 'Determination of Steady-State and Dynamic Control Laws of Doubly Fed Induction Generator Using Natural & Power Variables', IEEE Transactions on Industrial Electronics, vol.49, no.3, pp. 124-133.

35. Ahmed G Abo Khalil 2012, 'Synchronization of DFIG output voltage to utility grid in wind power system', Renewable energy, vol. 1, no. 44, pp. 193-198.

36. Alan Mullane, Gordon Light body & Yacamini, R 2005, 'Wind Turbine Fault Ride Through enhancement', IEEE Transactions on Power System, vol. 22, no. 4, pp. 2218-2214.

37. Alvaro, L, Araujo, L, David, S, Pedro, R, Edson, W & Santiago, A 2011, 'Simplified Modeling of a DFIG for Transient Studies in Wind Power Application', IEEE Transactions on Industrial Electronics, vol. 58, no. 1, pp. 1101-1113.

38. Andreas Petersson, Torbjorn Thiringer, Lennart Harnefors & Tomas Petru 2005, 'Modeling and Experimental Verification of Grid Interaction of a DFIG Wind Turbine', IEEE Transactions on Energy Conversion, vol. 20, no. 4, pp. 878-886.

39. Lan H, Wena S, Hong Y-Y, Yu DC, Zhang L. Optimal sizing of hybrid PV/diesel/ battery in ship power system. Appl Energy 2015;158:26-34.

40. Gan LK, Shek JKH, Mueller MA. "Hybrid windephotovoltaicedieselebattery system sizing tool development using empirical approach, life-cycle cost and performance analysis: a case study in Scotland. Energy Convers Manag 2015;106:479-94.

41. Merabet A, Ahmed K, Ibrahim H, Beguenane R, Ghias A. Energy management and control system for laboratory scale micro-grid based wind-PV-battery. IEEE Trans Sustain Energy 2017;8(1):145-54.
42. Ghenai C, Janajreh I. Design of solar-biomass hybrid micro-grid system in Sharjah. Energy Proc 2016;103:357-62.
43. Lambert T, Gilman P, Lilienthal P. "Micro-power system modeling with HOMER," Chap. 15. In: Farret FA, Simoes MG, editors. Integration of alternative sources of energy. John Wiley & Sons; 2006.
44. Yilmaz S, Ozcalikb HR, Aksua M, Karapınara C. Dynamic simulation of a PV-diesel-battery hybrid plant for off grid electricity supply. Energy Proc 2015;75:381-7.
45. Ghenai Chaouki, Salameh Tareq, Merabet Adel, Kadir Hamid Abdul. Modeling and optimization of hybrid solar-diesel-battery power system. In: 7th international conference on modeling, simulation, and applied optimization (ICMSAO). IEEE; 2017.
46. Hussain Mohammed Noorul, Janajreh Isam, Ghenai Chaouki. Multiple source sustainable hybrid micro-grid for urban communities: a case study in UAE. Energy Proc 2016;103:419-24.
47. Wies RW, Johnson RA, Agrawal AN, Chubb TJ. Simulink model for economic analysis and environmental impacts of a PV with diesel-battery system for remote villages. IEEE Trans Power Syst 2005;20(2):692-700.
48. Tu Tu, Rajarathnam Gobinath P, Vassallo Anthony M. Optimization of a stand-alone photovoltaic-wind-diesel-battery system with multi-layered demand scheduling. Renew Energy 2019;131:333-47.
49. Rodríguez-Gallegos Carlos D, Yang Dazhi, Gandhi Oktoviano, Bieri Monika, Reindl Thomas, Panda SK. A multi-objective and robust optimization approach for sizing and placement of PV and batteries in off-

grid systems fully operated by diesel generators: an Indonesian case study. Energy 2018;160:410-29.

50. Chettibi N, Mellit A. Intelligent control strategy for a grid connected PV/SOFC/ BESS energy generation system. Energy 2018;147:239-62.

51. Ceran Bartosz. The concept of use of PV/WT/FC hybrid power generation system for smoothing the energy profile of the consumer. Energy 2019;167: 853-65.

52. Khan Faizan A, Pal Nitai, Saeed SyedH. Review of solar photovoltaic and wind hybrid energy systems for sizing strategies optimization techniques and cost analysis methodologies. Renew Sustain Energy Rev 2018;92:937-47.

53. Qandil Mohammad D, Amano Ryoichi S, Abbas Ahmad I. A stand-alone hybrid photovoltaic, fuel cell and battery system. In: 12th international conference on energy sustainability. Lake Buena Vista, Florida, USA: ASME; 2018. June 24e28, 2018.

54. Abushnaf Jamal, Alexander Rassau. Impact of energy management system on the sizing of a grid-connected PV/Battery system. Electr J 2018;31(2):58-66.

55. Duque Grisales Eduardo Alexander, Gonzalez Ruiz Juan David, Ortíz, Grisales Paola Maritza, Lujan Tobon Anderson Felipe, Chica Lopez Sebasti an, Isaza Piedrahíta Andres Felipe. Design and construction of a stand-alone PV system for charging mobile devices in urban landscapes in medellin. Int J Renew Energy Resour 2018;8(1).

56. Samy MM, Barakat S, Ramadan HS. A flower pollination optimization algorithm for an off-grid PV-Fuel cell hybrid renewable system. Int J Hydrogen Energy 2018.

57. Han Ying, Zhang Guorui, Qi Li, ZhiyuYou, Chen Weirong, Liu Hong. Hierarchical energy management for PV/hydrogen/battery island DC micro-grid. Int J Hydrogen Energy 2018.

58. Sanni Shereef deen O, Oricha Joseph Y, Soremekun Rasaq K. Techno-economic analysis of hybrid solar PV/diesel power system: case study of sustainable agriculture. FUW Trend Sci Technol J 2018;3(2A):496-500.

59. Hazem Mohamed O, Amirat Y, Benbouzid M, Elbast A. Optimal design of PV/ fuel cell hybrid power system for the city of brest in France. Sfax, Tunisia: IEEE ICGE; 2014. p. 119-23.

60. Attala A, Taha ATM, Ryad A. PV, wind and fuel cell hybrid optimization generation for Al-arish site. Int J Recent Dev Eng Technol April 2014;2(Issue 4).

61. Ghenai C, Bettayeb M. Optimized design and control of an off grid solar PV/ hydrogen fuel cell power system for green buildings. In: NEFES 2017, IOP publishing IOP Conf. Series: Earth and environmental science, vol. 93; 2017.

62. Ghenai C, Merabet A, Salameh T, Pigem EC. Grid-tied and stand-alone hybrid solar power system for desalination plant. Desalin J 2018;435:172-80.

63. Ghenai C, Salameh T, Merabet A. Technico-economic analysis of off grid solar PV/fuel cell energy system for residential community in desert region. Int J Hydrogen Energy 2018.

64. Ezhiljenekkha, G.; MarsalineBeno, M. Review of Power Quality Issues in Solar and Wind Energy. Mater. Today Proc. 2020, 24, 2137–2143.

65. K.N. Nwaigwe, P. Mutabilwa, E. Dintwa, An overview of solar power (PV systems) integration into electricity grids, Materials Science for Energy Technologies, Volume 2, Issue 3, 2019, Pages 629-633.

66. Li, W.; Ren, H.; Chen, P.; Wang, Y.; Qi, H. Key Operational Issues on the Integration of Large-Scale Solar Power Generation—A Literature Review. Energies 2020, 13, 5951.

67. Seme, S.; Štumberger, B.; Hadžiselimovi´c, M.; Sredenšek, K. Solar Photovoltaic Tracking Systems for Electricity Generation: A Review. Energies 2020, 13, 4224.

68. Eltawil, M.A.; Zhao, Z. Grid-connected photovoltaic power systems: Technical and potential problems—A review. Renew. Sustain. Energy Rev. 2010, 14, 112–129.

69. Islam, M.; Nadarajah, M.; Hossain, M.J. A Grid-Support Strategy with PV Units to Boost Short-Term Voltage Stability Under Asymmetrical Faults. IEEE Trans. Power Syst. 2020, 35, 1120–1131.

70. Eltawil, M.A.; Zhao, Z. Grid-connected photovoltaic power systems: Technical and potential problems—A review. Renew. Sustain. Energy Rev. 2010, 14, 112–129.

71. Zhang, W.; Zhou, G.; Ni, H.; Sun, Y. A Modified Hybrid Maximum Power Point Tracking Method for Photovoltaic Arrays Under Partially Shading Condition. IEEE Access 2019, 7, 160091–160100.

72. Samara, S.; Natsheh, E. Intelligent Real-Time Photovoltaic Panel Monitoring System Using Artificial Neural Networks. IEEE Access 2019, 7, 50287–50299.

73. Ali, A.; Almutairi, K.; Malik, M.Z.; Irshad, K.; Tirth, V.; Algarni, S.; Zahir, M.; Islam, S.; Shafiullah, M.; Shukla, N.K. Review of online and soft computing maximum power point tracking techniques under non-uniform solar irradiation conditions. Energies 2020, 13, 3256.

74. Abdouramani Dadjé, Noël Djongyang, Janvier Domra Kana & Réné Tchinda 2016, ‘Maximum power point tracking methods for photovoltaic systems operating under partially shaded or rapidly variable

insolation conditions: a review paper', International Journal of Sustainable Engineering, vol. 9, no. 4, pp. 224-239.

75. Alice Hepzibah, A & Premkumar, K 2020, 'ANFIS current–voltage controlled MPPT algorithm for solar powered brushless DC motor based water pump', Electrical Engineering, vol.102, pp. 421-435.

76. Anup Anurag, Satarupa Bal, Suman Sourav & Mrutyunjaya Nanda 2016, 'A review of maximum power- point tracking techniques for photovoltaic systems', International Journal of Sustainable Energy, vol. 35. no. 5, pp. 478-501.

77. Bahrami, M, Gavagsaz-Ghoachani, R, Zandi, M, Phattanasak, M, Maranzanaa, G, Nahid-Mobarakeh, B, Pierfederici, S & Meibody-Tabar, F 2019, 'Hybrid maximum power point tracking algorithm with improved dynamic performance', Renewable energy, vol.130, pp. 982-991.

78. Bataineh, K 2018, 'Improved hybrid algorithms-based MPPT algorithm for PV system operating under severe weather conditions', IET Power Electronics, vol. 12, no. 4, pp.703-711.

79. Belhachat, F & Larbes, C 2017, 'Global maximum power point tracking based on ANFIS approach for PV array configurations under partial shading conditions', Renewable and Sustainable Energy Reviews, vol. 77, pp. 875-889.

80. Boumaaraf, H, Talha, A & Bouhali, O 2015, 'A three-phase NPC grid-connected inverter for photovoltaic applications using neural network MPPT', Renewable and Sustainable Energy Reviews, vol.49, pp. 1171-1179.

81. Da Luz, CMA, Vicente, EM & Tofoli, FL 2020, 'Experimental evaluation of global maximum power point techniques under partial shading conditions', Solar Energy, vol. 196, pp. 49-73.

82. Danandeh, MA 2018, ‘A new architecture of INC-fuzzy hybrid method for tracking maximum power point in PV cells’, Solar Energy, vol. 171, pp. 692-703.

83. Faiza Belhachat & Cherif Larbes 2017, ‘Global maximum power point tracking based on ANFIS approach for PV array configurations under partial shading conditions’, Renewable and Sustainable Energy Reviews, vol. 77, pp. 875-889.

84. Fernando Lessa Tofoli, Dênis de Castro Pereira & Wesley Josias de Paula 2015, ‘Comparative Study of Maximum Power Point Tracking Techniques for Photovoltaic Systems’, International Journal of Photoenergy, vol. 2015, Article ID 812582, pp. 1-10.

85. Gosumbonggot, Jirada & Goro Fujita 2019, ‘Partial shading detection and global maximum power point tracking algorithm for photovoltaic with the variation of irradiation and temperature’, Energies, vol.12, no. 202, pp. 1-22.

86. Houria Boumaaraf, Abdelaziz Talha & Omar Bouhali 2015, ‘A three-phase NPC grid-connected inverter for photovoltaic applications using neural network MPPT’, Renewable and Sustainable Energy Reviews, vol. 49, pp. 1171-1179.

87. Hsu, TW, Wu, HH, Tsai, DL & Wei, CL 2018, ‘Photovoltaic energy harvester with fractional open-circuit voltage based maximum power point tracking circuit’, IEEE Transactions on Circuits and Systems II: Express Briefs, vol. 66, no. 2, pp. 257-261.

88. Hu, K, Cao, S, Li, W & Zhu, F 2019, ‘An Improved Particle Swarm Optimization Algorithm Suitable for Photovoltaic Power Tracking under Partial Shading Conditions’, IEEE Access, vol.7, pp.143217-143232.

89. Jirada Gosumbonggot 2016, ‘Maximum Power Point Tracking Method using Perturb and Observe Algorithm for Small Scale DC Voltage Converter’, Procedia Computer Science, vol. 86, pp. 421-424.

90. Kante Visweswara 2014, ‘An Investigation of Incremental Conductance based Maximum Power Point Tracking for Photovoltaic System’, Energy Procedia, vol. 54, pp.11-20.

91. Khanaki, Razieh, Mohd Radzi, Mohd Amran & Marhaban, Mohammad Hamiruce 2014, ‘Artificial neural network based maximum power point tracking controller for photovoltaic standalone system’, International Journal of Green Energy, vol.13, no.3, pp. 1543-5075.

92. Kumar, R, Khandelwal, S, Upadhyay, P & Pulipaka, S 2019, ‘Global maximum power point tracking using variable sampling time and pv curve region shifting technique along with incremental conductance for partially shaded photovoltaic systems’, Solar Energy, vol.189, pp.151-178.

93. Li, G, Jin, Y, Akram, MW, Chen, X & Ji, J 2018, ‘Application of bio-inspired algorithms in maximum power point tracking for PV systems under partial shading conditions–A review’, Renewable and Sustainable Energy Reviews, vol. 81, pp.840-873.

94. Li, W, Zhang, G, Pan, T, Zhang, Z, Geng, Y & Wang, J 2019, A Lipschitz Optimization-Based MPPT Algorithm for Photovoltaic System Under Partial Shading Condition. IEEE Access, vol.7, pp.126323-126333.

95. Lyden, S & Haque, ME 2015, ‘Maximum Power Point Tracking techniques for photovoltaic systems: A comprehensive review and comparative analysis’, Renewable and Sustainable Energy Reviews, vol. 52, pp. 1504-1518.

96. Mehmet Sait Cengiz & Mehmet Salih Mamiş 2015, 'Price-Efficiency Relationship for Photovoltaic Systems on a Global Basis', International Journal of Photoenergy, vol.2015, Article ID 256101, pp. 1-12.

97. Mehreen Gul, Yash Kotak & Tariq Muneer 2016, 'Review on recent trend of solar photovoltaic technology', Energy Exploration & Exploitation, vol. 34, no. 4, pp. 485-526.

98. Mostafa, MR, Saad, NH & El-sattar, AA 2020, 'Tracking the maximum power point of PV array by sliding mode control method', Ain Shams Engineering Journal, vol. 11, no. 1, pp. 119-131.

99. Nabipour, M, Razaz, M, Seifossadat, SGH & Mortazavi, SS 2017, 'A new MPPT scheme based on a novel fuzzy approach', Renewable and Sustainable Energy Reviews, vol. 74, pp. 1147-1169.

100. Padmanaban, S, Priyadarshi, N, Bhaskar, MS, Holm-Nielsen, JB, Ramachandaramurthy, VK & Hossain, E 2019, 'A Hybrid ANFIS-ABC Based MPPT Controller for PV System With Anti-Islanding Grid Protection: Experimental Realization', IEEE Access, vol.7, pp.103377-103389.

101. Premkumar, K & Manikandan, BV 2018, 'Stability and Performance Analysis of ANFIS Tuned PID Based Speed Controller for Brushless DC Motor', Current Signal Transduction Therapy, vol.13, no.1,
pp. 19-30.

102. Premkumar, K & Manikandan, BV 2014, 'Adaptive Neuro Fuzzy Inference System based speed controller for brushless DC motor', Neurocomputing, vol.138, pp. 260-270.

103. Putri, RI, Pujiantara, M, Priyadi, A, Ise, T & Purnomo, MH 2017, 'Maximum power extraction improvement using sensorless controller

based on adaptive perturb and observe algorithm for PMSG wind turbine application', IET Electric Power Applications, vol.12, no.4, pp.455-462.

104. Rathi, KJ & Ali, MS 2016, 'NFC Design using ANFIS for Power Electronics Circuits', International Journal of Innovative Research In Electrical, Electronics, Instrumentation and Control Engineering, vol.4, no. 3, pp. 9-12.

105. RatnaIka Putri, Sapto Wibowo & Muhamad Rifa 2015, 'Maximum Power Point Tracking for Photovoltaic using Incremental Conductance Method', Energy Procedia, vol.68, pp.22-30.

106. Rezk, H, Aly, M, Al-Dhaifallah, M & Shoyama, M 2019, 'Design and Hardware Implementation of New Adaptive Fuzzy Logic-Based MPPT Control Method for Photovoltaic Applications', IEEE Access, vol.7, pp.106427-106438.

107. Rokeya Jahan Mukti & Ariful Islam 2015, 'Modeling and performance analysis of PV module with Maximum Power Point Tracking in Matlab/Simulink', Applied Solar Energy, vol.51, no.4, pp.245–252.

108. Rozana Alik & Awang Jusoh 2017, 'Modified Perturb and Observe (P&O) with checking algorithm under various solar irradiation', Solar Energy, vol.148, pp.128-139.

109. Saban Ozdemir, Necmi Altin & Ibrahim Sefa 2017, 'Fuzzy logic based MPPT controller for high conversion ratio quadratic boost converter', International Journal of Hydrogen Energy, vol.42, no.28, pp. 17748-17759.

110. Sabir Messalti, Abdelghani Harrag & Abdelhamid Loukriz 2017, 'A new variable step size neural networks MPPT controller: Review, simulation and hardware implementation', Renewable and Sustainable Energy Reviews, vol.68, no.1, pp. 221-233.

111. Sakh Mozaffari Niapour, S, Danyali, MBB, Sharifian, MR & Feyzi 2011, 'Brushless DC motor drives supplied by PV power system based on Z-source inverter and FL-IC MPPT controller', Energy Conversion and Management, vol.52, no.8–9, pp. 3043-3059.

112. Samani, L & Mirzaei, R 2019, 'Model predictive control method to achieve maximum power point tracking without additional sensors in stand-alone renewable energy systems', Optik, vol. 185, pp.1189-1204.

113. Solangi, KH, Islam, MR, Saidur, R, Rahim, NA & Fayaz, H 2011, 'A review on global solar energy policy, Renewable and Sustainable Energy Reviews', vol.15, no. 4, pp. 2149-2163.

114. Zainal, NA, Yusoff, AR & Apen, 2019, 'Integrated cooling systems and maximum power point tracking of fuzzy logic controller for improving photovoltaic performances', Measurement, vol.131, pp.100-108.

115. Zou, Y, Yan, F, Wang, X & Zhang, J 2019, 'An Efficient Fuzzy Logic Control Algorithm for Photovoltaic Maximum Power Point Tracking under Partial Shading Condition', Journal of the Franklin Institute, vol. 357, no. 6, pp. 3135-3149.

List of Publications

S.no	Journal indexing	Status of Paper	Type of paper	Title of the Paper	Journal Name
1.	Scopus	Published	Research	Maximum Power extraction in partial shaded grid-connected in PV system using hybrid fuzzy logic/Neural network based variable step size mppt	Smart grids and sustainable energy
2.	Scopus	Published	Research	De-rated concept-based adaptive neuro-fuzzy inference system (ANFIS) and fuzzy mppt technique for PV Power grid	Design Engineering
3.	Scopus	Submitted	Research	Artificial ecosystem optimization algorithm tuned PI controlled grid-connected PV-system	Smart grids and sustainable energy
4	Scopus	Published	Research	Horse herd optimization mppt for grid-connected pv system under partial shading conditions	IEEE Xplore
5	Scopus	Submitted	Research	Artificial Rabbit optimized Neural network control of Battery and PV-powered UPQC for Microgrid Application	Optik

Research Conference Details

S.no	Journal indexing	Type of paper (Research/Review)	Conference Name	Title of the Paper	ISSN Number
1.	Conferences	Research	2022 IEEE 10th PICON Conference	Horse herd optimization mppt for grid-connected pv system under partial shading conditions	ISSN 2642-5289
2	Conferences	Review	International Conference on Recent Innovation in Science, Engineering and Technology	Artificial-based maximum power point tracking for green building application.	ISBN: 978-94-5408-314-3
3	Conference	Research	International Conference on Recent Innovations in Science, Engineering & Technology-ICRISET-2021	De-rated concept based adaptive neuro-fuzzy inference system (ANFIS) and fuzzy mppt technique for PV Power grid	ISBN: 978-93-91131-30-2
4	Conference	Research	2014 IEEE Conference on POWER, ENERGY, AND INDUSTRIAL INNOVATIONS (PEII)	*Adaptive Neuro-Fuzzy Inference System for Optimizing Energy Flow in Grid-linked Solar and Battery Storage Systems*	accepted